ON THE ANALYSIS OF TWO LOW-MASS, ECLIPSING BINARY SYSTEMS IN THE YOUNG ORION NEBULA CLUSTER

By

Yilen Gómez Maqueo Chew

Dissertation

Submitted to the Faculty of the

Graduate School of Vanderbilt University

in partial fulfillment of the requirements

for the degree of

DOCTOR OF PHILOSOPHY

in

Physics

August, 2010

Nashville, Tennessee

Approved:

Prof. Keivan G. Stassun

Prof. David J. Ernst

Prof. Robert A. Knop

Prof. Robert C. O'Dell

Prof. Andrej Prša

Prof. David A. Weintraub

ACKNOWLEDGEMENTS

This research would not have been possible without the financial support of CONACYT and Keivan Stassun.

I am very grateful to the people from Villanova's Astronomy Department for sharing their knowledge on eclipsing binaries, for their hospitality, and for always proving excellent espresso. I would like to also thank those in the Physics and Astronomy Department at Vanderbilt that helped me through this journey, specially the other grad students, Leslie who always had words of encouragement, and Bob who believed in me.

Special thanks to Gilma and Martha for sharing with me all these years, with their ups and downs. I am also grateful for the good time spent at the Fortress, with the other members of the garrison: Talia and Yonah. Thank you Brittany, for being Thing 1 or Thing 2, as required, and also to Stacey for Hana Club. I would like to thank Jeff for good food, and words. And I would also like to thank Ponch for being a good friend.

Finally, I would like to thank my parents and sister, Yuyen, for being patient and never doubting that I could accomplish this, as well as the Agraz GM family for feeding me and keeping me well caffeinated when I visited.

TABLE OF CONTENTS

LIST OF TABLES

LIST OF FIGURES

CHAPTER I

INTRODUCTION

Empirical measurements of the masses, radii, temperatures, and luminosities of pre-main sequence (PMS) stars and brown dwarfs are valuable for the understanding of star formation. They delimit the Initial Mass Function, defining the outcome of star formation and providing the energy scale for the formation process. They represent an observational tie to the theoretical evolution models that describe the chronology of stellar evolution, and set the timescales for circumstellar disk evolution and planet formation. In order for these models to accurately describe the physics of PMS evolution, they must be tested against observed properties of young stars and brown dwarfs (e.g., Mathieu et al., 2007).

Mass is the physical property of stars that is most important in determining the course of their evolution. Most stellar masses, however, are derived from evolutionary tracks based on converting the measured spectral types and magnitudes to model-dependent calculations of temperatures and luminosities. Thus, the empirical determination of PMS masses represents the link between observations and theoretical evolutionary models. The calibration of these models can be done by measuring the dynamical masses, with precisions of at least a few percent, and jointly obtaining stellar properties like luminosities and effective temperatures or radii (Torres et al., 2010). Only three systems allow for dynamical mass measurements to be acquired:

young stars with a circumstellar disks, binary systems with both double-lined spectroscopic and astrometric orbits, and double-lined eclipsing binary (EB) systems.

In the case of the first type of system mentioned above, the dynamical mass of the parent star can be determined from the disk's rotation curve (e.g., Prato et al., 2002). The derived mass depends on the inclination of the disk with respect to the observer, which can be estimated from the morphology of the observed disk emission. In the second case, direct mass measurements for both binary components is possible. The spectroscopic orbit solution provides the mass ratio of the system, as well as the period and information about the size and eccentricity of the orbit. The inclination of the system can be determined from the astrometric orbit solution, which sets the scale of the system and thus the absolute masses of the components (e.g., Boden et al., 2005). Lastly, eclipsing binaries provide both masses, and radii for each component, and the ratio of the effective temperatures (see Chapter IV.2). Eclipsing binaries are rare, because their orbits have to be oriented such that we see the components eclipse one another.

There are only a handful of eclipsing binary systems where both components are found to be in their PMS phase, and which constitute most of the direct measurements, independent of theoretical models and distance determination, against which the earliest stages of theoretical evolutionary models can be compared and tested. There are a few tens of systems for which the dynamical masses of their PMS components have been measured (Mathieu et al., 2007); eclipsing binaries however are the only ones that allow for the measurement of the radii of the components. For

PMS, low-mass, eclipsing binaries, where both components have masses below 1.5 $M_{\odot}$, there are only six systems reported in the literature: ASAS J052821+0338.5 (Stempels et al., 2008); RXJ 0529.4+0041 (Covino et al., 2000, 2004); V1174 Ori (Stassun et al., 2004); Parenago 1802 (Cargile et al., 2008; Stassun et al., 2008); JW 380 (Irwin et al., 2007), and 2MASS J05352184-0546085 (Stassun et al., 2006, 2007). Table 1 presents the physical properties of these low-mass, PMS, eclipsing binary systems. This thesis is focused on the multi-band, multi-epoch analysis of two of the youngest and least massive EB systems on this list, Parenago 1802, and 2MASS J05352184-0546085. The components of the latter are below the hydrogen-burning limit, i.e., they are brown dwarfs.

The study of young binaries, such as Par 1802 and 2M0535−05, not only allows us to determine the properties of the individual components, but it also allows us to probe into the formation mechanisms of close binaries and into the evolution of their orbits. Multiple systems are thought to form simultaneously from the same protostellar core, such that their components are assumed to be coeval and to have the same metallicity. Binary and multiple systems are likely the result of collapse with rotation in order to distribute angular momentum into the orbital motions of the stars (e.g., Larson, 2003). Equal-mass components of binary systems, also known as *twins*, are therefore expected to evolve following essentially the same evolutionary track. While wide binaries may be due to fragmentation of rotating cloud cores, close binaries require the involvement of stochastic processes, to account for the large range of separations, and of dissipative processes, to reduce the initial angular momentum

Table 1: Physical Properties of the Low-Mass, PMS Eclipsing Binaries

	Primary Secondary	Mass ($M_\odot$)	Radius ($R_\odot$)	$T_{\rm eff}$ (K)	$T_{\rm eff,2}/T_{\rm eff,1}$
1	ASAS J052821+0338.5	1.375 ± 0.011	1.83 ± 0.01	5103 ± 100	0.931 ± 0.005
		1.329 ± 0.008	1.73 ± 0.01	4751 ± 100	
2	RXJ 0529.4+0041	1.27 ± 0.01	1.44 ± 0.05	5200 ± 150	...
		0.93 ± 0.01	1.35 ± 0.05	4220 ± 150	
3	V1174 Ori	1.009 ± 0.015	1.339 ± 0.015	4470 ± 120	0.809 ± 0.002
		0.731 ± 0.008	1.065 ± 0.011	3615 ± 100	
4	Par 1802†	0.391 ± 0.032	1.73 ± 0.11	3675 ± 150	0.915 ± 0.002
		0.385 ± 0.032	1.62 ± 0.08	3360 ± 150	
5	JW 380	$0.262\ ^{+0.025}_{-0.024}$	$1.189\ ^{+0.039}_{-0.175}$	3200 ± 300	$0.8700\ ^{+0.0168}_{-0.0041}$
		0.151 ± 0.013	$0.897\ ^{+0.170}_{-0.034}$	3000 ± 400	
6	2M0535−05†	0.0572 ± 0.0033	0.690 ± 0.011	2715 ± 200	1.050 ± 0.004
		0.0366 ± 0.0022	0.540 ± 0.009	2850 ± 200	

References: (1) Stempels et al. (2008); (2) Covino et al. (2000, 2004); (3) Stassun et al. (2004); (4) Cargile et al. (2008); Stassun et al. (2008); Gómez Maqueo Chew et al. (2010); (5) Irwin et al. (2007); (6) Stassun et al. (2006, 2007); Gómez Maqueo Chew et al. (2009)

† The analysis of these systems is presented in this thesis.

and average energy (Bate et al., 2002).

The multiplicity properties of newly born stars and brown dwarfs, such as the multiplicity fraction, the orbital geometry, and the mass ratio are likely to be mass dependent (e.g., Lafrenière et al., 2008; Bonnell et al., 2007). Furthermore, these properties may be modified by dynamical interactions over a few million years that may depend on the density of the environment (e.g., Kroupa, 1998). Observational studies of field stars in the solar neighborhood have found that while low-mass stars and brown dwarfs have a binary frequency between 10 and 30 percent (e.g., Burgasser et al., 2003; Close et al., 2003; Fischer and Marcy, 1992) more than half of

solar mass stars have companions (Duquennoy and Mayor, 1991). In the high-mass regime, nearly all of stars are in binary or multiple systems (Mason et al., 1998). The multiplicity of PMS stars and brown dwarfs is found generally to agree with the field distribution for dense clusters (Köhler et al., 2006) or to be higher up to two times for less dense environments (e.g., Lafrenière et al., 2008).

If the orbit of a binary system is eccentric, the tidal forces between the components will be time dependent and will produce strong disturbances at each periastron passage (Hut, 1981). As a result of tidal interactions between the components of a close binary, the stellar components synchronize their rotation to the orbital motion, and, at a much longer timescale, the orbit is circularized. An important part of this orbital evolution occurs during the components' PMS phase and continues during the main sequence (Melo et al., 2001). The timescales for both synchronization of the components and circularization of the orbit in the context of Par 1802 will be presented in Section V.4.1.

We present in Chapter II the photometric and spectroscopic observations used for the analysis of the two eclipsing binary systems, Parenago 1802 and 2MASS J05352184-0546085. We also detail the reduction of the different data, in particular that of the near-infrared photometric observations in Section II.1. In Chapter III, the creation of radial velocity and light curves from the observations is described. The methodology of the analyses implemented for the study of both eclipsing systems are explained in Chapter IV. The periodicity analysis of the light curves used to determine the orbital period of the binaries and the rotation periods of the components of each

system is described in Section IV.1. The simultaneous modeling of the light and radial velocity curves, including a detailed assessment of the parameter uncertainties, is found in Section IV.2. Chapter V describes the analysis and results of Parenago 1802, and Chapter VI that of the eclipsing brown dwarfs. Lastly, a summary of our findings, including a comparison of the properties of Par 1802, 2M0535−05 and the other known PMS EBs presented in Table 1, and a description of work in progress is found in Chapter VII.

CHAPTER II

OBSERVATIONS AND DATA REDUCTION

The physical properties of an eclipsing binary system and its components can be determined when different types of observational data are analyzed jointly. Typically, the data set consists of spectroscopic and photometric data. Depending on the nature of the eclipsing system one can obtain different observable curves.

The photometric data of an eclipsing binary compose the light curve, which describes the flux observed from the system as a function of time. Eclipsing binary light curves are characterized by periodic increases in magnitude, i.e., the system appears dimmer to the observer for an extended period of time. This occurs when one of the components blocks the light of the other as it passes in front of it, eclipsing it. The simultaneous modeling of multi-band light curves allows us to probe the radiative properties of the system in order to determine the components' radii. The photometric data obtained for Par 1802 and 2M0535−05 are described in Sections II.1 and II.2.

The spectroscopic observations of eclipsing binaries are essential for describing the dynamic properties of the system, primarily through radial velocity (RV) measurements. The spectroscopic data for Par 1802 are described in Section II.3.1 and for 2M0535−05 in Section II.3.2. Precise and accurate RVs are necessary in the analysis of eclipsing binaries in order to calculate fundamental stellar properties. The

uncertainties in the RV measurements presented for these stars are of the order of a few km s^{-1}. Radial velocities can be extracted by cross-correlation of observed spectra against a reference spectrum and by using a broadening function method. The techniques used for the creation of the RV curves of Par 1802 and 2M0535−05 are described in Chapter III.

From spectroscopic observations, we can obtain the RV curves of the system, and we may also determine the spectral types of one or both of the components and may give a measure of their effective temperatures, surface gravities, metallicities and rotational velocities. Moreover, they can provide additional information about the luminosity ratio, which constraints the individual radii of the eclipsing components.

II.1 The JHK_S Photometric Observations

The near-infrared (NIR), corresponding to wavelengths between ~ 1 and 5 μm, is a very useful wavelength range in which to observe low-mass objects in star formation regions. NIR radiation is able to travel through interstellar gas and dust experiencing less absorption than visible light; thus, it is an excellent probe into dusty environments which are often opaque at optical wavelengths. Moreover, emission from stars in the low-mass stellar population in dusty star formation regions generally peaks at NIR wavelengths. However, observing in the infrared presents particular challenges. NIR observations are affected by ambient thermal emission, including the telescope's optics and support structure, and by the brightness of the atmosphere at these wavelengths. The night sky's background radiation at $\lambda < 2$ μm is domi-

nated by scattered moonlight and starlight and by high-altitude airglow emission; at $\lambda > 2\ \mu$m, it is dominated by the blackbody thermal radiation of the atmosphere and of the telescope (Glass, 1999). Furthermore, radiation at many wavelengths in the infrared is effectively absorbed by atmospheric water vapor; this effect varies with observing site, season and time, making it necessary to be accounted for when reducing the observations. The NIR atmospheric transmission at the site of our observations, shown in Fig. 1, was adopted from Section III.1.b1 of the *Explanatory Supplement to the 2MASS All Sky Data Release*[1], and is compared to the JHK_S passbands.

We observed Par 1802 and 2M0535−05 in the NIR passbands, JHK_S, using the ANDICAM instrument on the 1.3-m SMARTS[2] telescope at Cerro Tololo Inter-American Observatory[3] (CTIO) in Chile. Optical images in B, V, or $I_C$were acquired simultaneously to the NIR images, as described in Section II.2. The characteristics of the ANDICAM's NIR and optical detectors are presented in Table 2.

Table 2: ANDICAM Detector Characteristics

	NIR	Optical
Format (unbinned)	1024×1024	2048×2048
Pixel Size (μm)	18	15
Image Pixel Scale (arcsec/pixel)	0.137	0.185
Field of View (arcmin^2)	∼2.4×2.4	∼6×6

[1]http://www.ipac.caltech.edu/2mass/releases/allsky/doc/explsup.html
[2]http://www.astro.yale.edu/smarts/
[3]http://www.ctio.noao.edu/

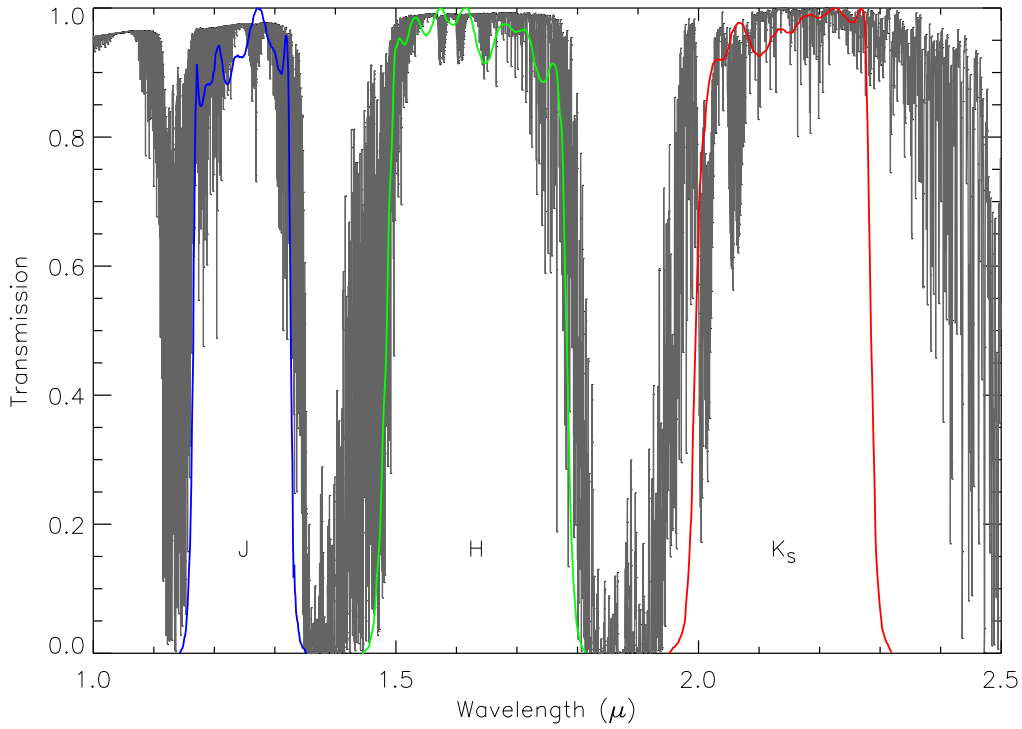

Figure 1: NIR Atmospheric and Passband Transmission. The transmission of the atmosphere above CTIO, shown in grey, was adopted from the *Explanatory Supplement to the 2MASS All Sky Data Release*. This model accounts for atomic and molecular absorption, and Rayleigh and site-specific mean aerosol scattering. The J transmission curve is shown in blue in the figure, the H curve in green, and the K_S curve in red. Both the atmospheric and the passband transmission curves have been normalized to have a maximum transmission of 1.0.

The JHK_S filters have central wavelengths of 1.2 μm, 1.6 μm and 2.2 μm, respectively. The K_S passband is narrower than the K band used by Johnson (1964). This variation reduces the contribution of terrestrial thermal background radiation (e.g., Wainscoat and Cowie, 1992).

ANDICAM's dichroic mirror splits the beam at 1.0 μm and allows for simultaneous optical and NIR observations (DePoy et al., 2003). Figure 2 shows the optical layout of

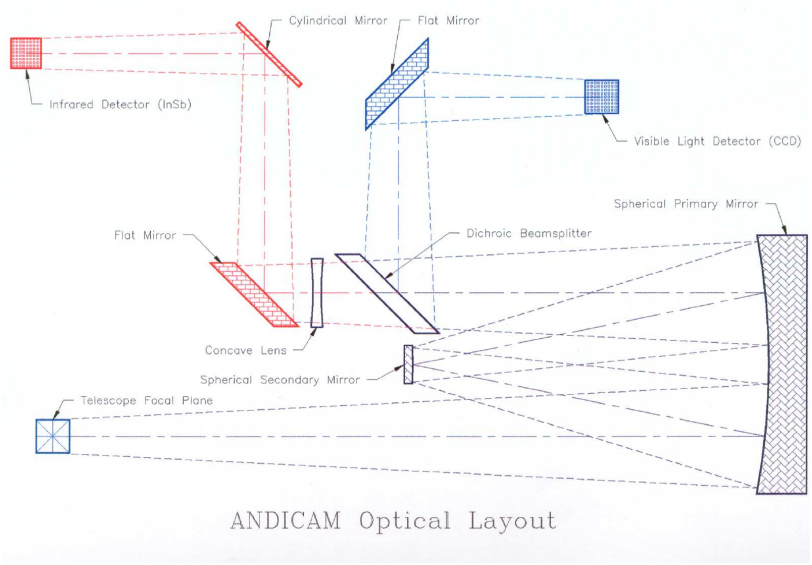

Figure 2: ANDICAM's Optical Layout (DePoy et al., 2003). By splitting the beam, ANDICAM allows for the simultaneous imaging in the optical (blue path) and the NIR (red path).

ANDICAM; the red beam describes the path of the NIR light and the blue beam that of the optical light. Each NIR observation is composed of multiple, short exposure images with slightly different fields of view, obtained by moving an internal mirror in the NIR channel while maintaining the telescope's pointing. This allows the optical image to have a longer exposure than that of the individual frames that compose a single NIR observation. This observing technique is called dithering and is important for correcting for bad pixels and removing cosmic rays hits. The NIR channel's field of view, $\sim 2.4' \times 2.4'$, is not exactly located at the center of the larger ($\sim 6' \times 6'$) optical field of view and it's exact location depends on the dithering position.

The observations were taken in queue mode one to three times a night during

the Fall and Spring of each year from 2003 through 2008. The queue observing is done exclusively by a CTIO staff astronomer, allowing for cost-effective and telescope-time effective time series photometry over a long timespan, which is very useful for monitoring the behavior of eclipsing binaries. The photometric observing campaigns for Par 1802 and 2M0535−05 are described in detail in §V.1.2 and §VI.1, respectively.

II.1.1 NIR Data Reduction

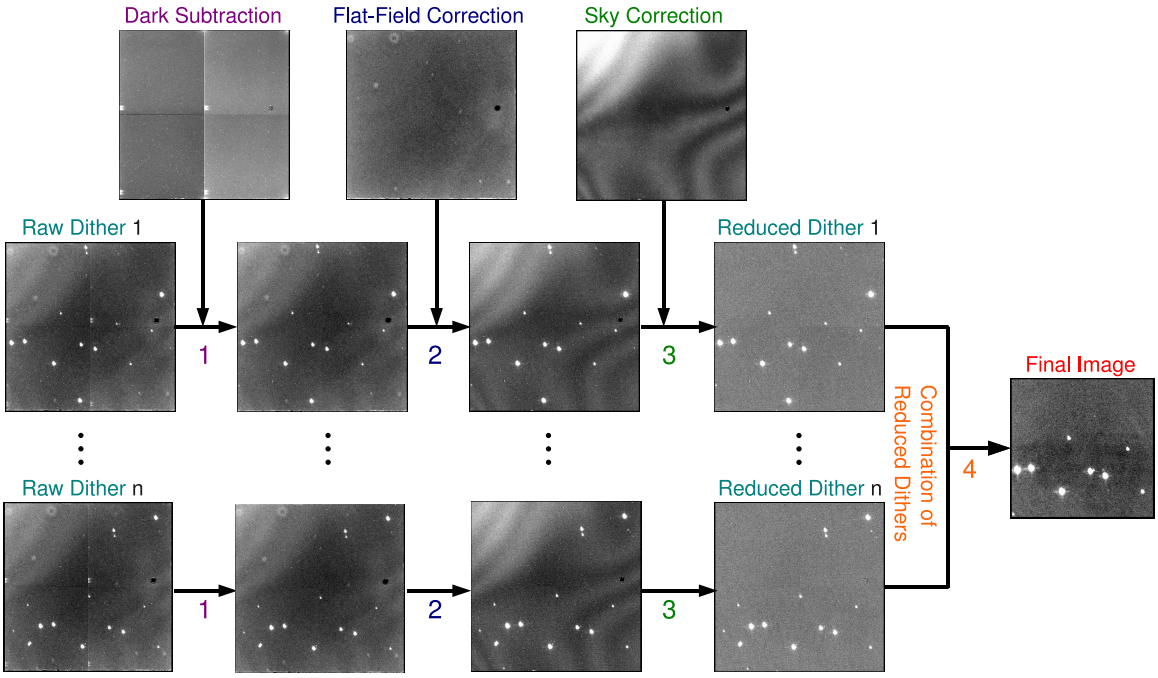

Figure 3: JHK_S Data Reduction Flowchart. Steps 1 through 3 are repeated for each of the dither pointings using the corresponding calibration frames. The reduced frames were then combined to form the final image in Step 4. Observations of 2M0535−05 are used in this example.

This section describes the reduction of the photometric JHK_S data. The reduction process followed is the same for the observations of both systems. Slight modifications were made for the different exposure times used; Par 1802 has a K_S magnitude of 9.9, whereas 2M0535−05's is 13.5 (Cutri et al., 2003).

All the NIR data were pre-processed at CTIO before being distributed; a bad-pixel mask was applied to the raw images and each frame was binned 2×2. Calibration images, described below, were also obtained regularly at the beginning of each observing night and were distributed with the science images. ANDICAM has a linear response up to $\sim$ 5 000 counts per pixel for the unbinned images. Thus for each binned frame, one should be cautious for counts per pixel that exceed 15 000.

The reduction process described below refers to each of the dithered frames that compose a single NIR observation as an individual image until they were combined in the final step. Figure 3 presents a flowchart of the reduction process; the steps of the reduction process are described below:

1. Dark Subtraction – Although called "dark" images in the pipeline processing, these short exposures are dominated by the detector's readout noise. To account for the bias information, the dark current, and the readout noise present in the images, we subtracted a dark image from every science frame using the `IRAF`[4] task `IMARITH`. Typically, ten dark frames were available for every night the science targets were observed. We median combined these to create one dark

[4] `IRAF` is distributed by the National Optical Astronomy Observatory, which is operated by the Association of Universities for Research in Astronomy (AURA) under cooperative agreement with the National Science Foundation.

image. If the dark frames were not furnished for a given night, we subtracted the dark image closest to the date of the observations.

2. Flat-Field Correction – A flat-field correction is needed to account for the variation in sensitivity of each pixel throughout the image and for instrumental vignetting. We divided each of the science images by the corresponding normalized, wavelength-dependent flat-field which was obtained by pointing the telescope at an evenly illuminated screen within the dome. This type of flat-field image is also known as a dome-flat. Typically, a set of dome-flats in one NIR passband were acquired each night, so that a full suite of JHK_S dome-flats were obtained every three nights. The sets were composed of seven distinct dome-flats, one for each dither position. Each dome-flat was composed of the average of $\sim$ 10 frames taken with the flat-field lamp on, from which a combination of $\sim$ 10 frames with the lamp off was subtracted. The result is the characterization of the illuminated flat-field, with the bias level, the dark current, the readout noise, the thermal background, and the scattered light that are typical in NIR observations removed. The dome-flat was normalized such that its median is equal to unity, and then the science images were divided by the corresponding normalized dome-flat using the task `IMARITH`. In season `I`, dome-flats were not obtained in JHK_S; thus, the reduction process of the `I` data is slightly different, and is described in §II.1.2.

3. Sky Correction – Even after applying the flat-field correction, the images present

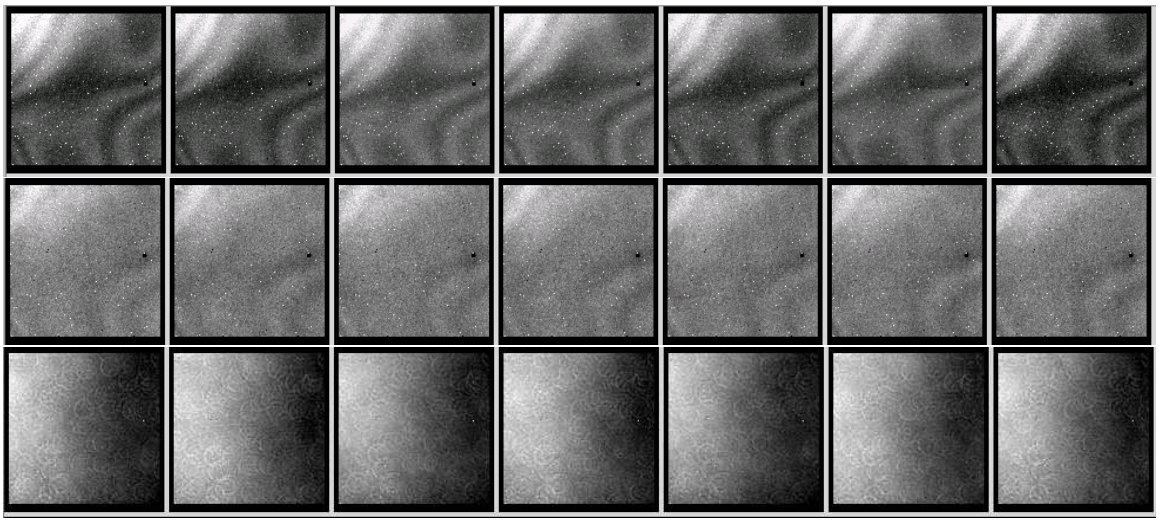

Figure 4: JHK_S Master Sky Frames. Individual sky frames were created for each of the seven dither positions in J (top), H (middle), and K_S (bottom) each observing season. These sky frames were created for the observing season `VII`.

variations that surface as one uses plane-parallel light to illuminate the detector. This remaining structure found in the images may be due to a difference in optical path, scattered light and/or thermal emission, important contributors in the NIR. The sky calibration frames, which we will refer to as master sky frames, were used to correct for this effect and were particular to each filter and to each dither position. Examples of these are shown in Figure 4. The sky contribution was removed from the flattened science images by subtracting a normalized master sky frame. One master sky was created for each of the seven dither positions in each of the NIR filters to account for the difference in optical paths. Furthermore, we made master skies specific for every observing season in case any change in the instrument or configuration occurred during

the off-season. We used between 10 and 15 science images from different nights throughout the observing season to create the master skies. Each frame was chosen to have a slightly different field of view, so that the stars in the field of view are removed when the images are combined. Because observations were taken only one to three times a night, the images that compose each master sky are scaled so their medians are the same before being combined. The combination of the images into a master sky for a given filter and dither position was done by using the `IRAF` task `IMCOMBINE`. This median combination of the sky images ensured that the stars and other high count contributions are effectively removed and that only the sky contribution remained.

The appropriate master sky was scaled making its median equal to the median of the science frame, and then subtracted from the image being reduced. Note that in the case of the `I` data, we did not create specific master skies for the dithered positions.

4. Combination of Dithered Frames into a Single Observation – The reduced frames were aligned, cropped, and co-added to create a single NIR observation. We first calculated the pixel offset between the different dither frames with respect to the first frame. Using `IMEXAMINE`, we obtain the pixel coordinates of the same star in all the dithers of the observation. Then, we created a list of the shifts with respect to the first image of each subsequent frame. Using the `IRAF` task IMALIGN and the calculated offsets, the frames were aligned and cropped,

such that the star in each of the cropped frames was moved to the same pixel coordinates. We combined each of the dithers using `IMCOMBINE` by averaging the counts in each frame without any scaling to obtain a single co-added science observation.

II.1.2 `I` Season: Undithered Calibrations

At the beginning of our dataset, dome-flats for the individual dither positions were not available which affected the reduction of the Season `I` data. The calibration images used to create Season `I`'s flat-field images comprise instead ten brightly illuminated and ten faintly illuminated "blank" sky frames, all with an exposure time of 4 seconds. Unlike the dome-flats described in the previous section, these images were obtained by pointing the telescope at an apparently blank portion of the sky at the beginning of the night and at a fixed mirror position. The reduction process for the `I` data was adapted to accommodate for the difference in the calibration images, and consists of the following steps:

1. Night Sky Subtraction – A night sky image was subtracted from each of the science frames. This night sky image was composed from the seven dither frames that compose the NIR observation. The individual frames were scaled to the median of the first one. Then they were combined by their median using the task `IMCOMBINE`; a rejection of the maximum value for each pixel was implemented to ensure that the high-count contributions, such as stars, were removed from the night sky image before being subtracted.

2. Flat-Field Correction – The brightly illuminated blank sky frames for a single night were median-combined using `IMCOMBINE` with no rejection or scaling; the faintly illuminated blank sky frames were combined in the same manner. The combined faint image was then subtracted from the combined bright image creating the flat-field. This image was then normalized to have a median of unity, creating our flat-field image.

3. Combination of Dithered Frames into a Single Observation – The dithers were aligned, cropped, and co-added, as described in the previous section.

II.1.3 The NIR Bad Quadrant

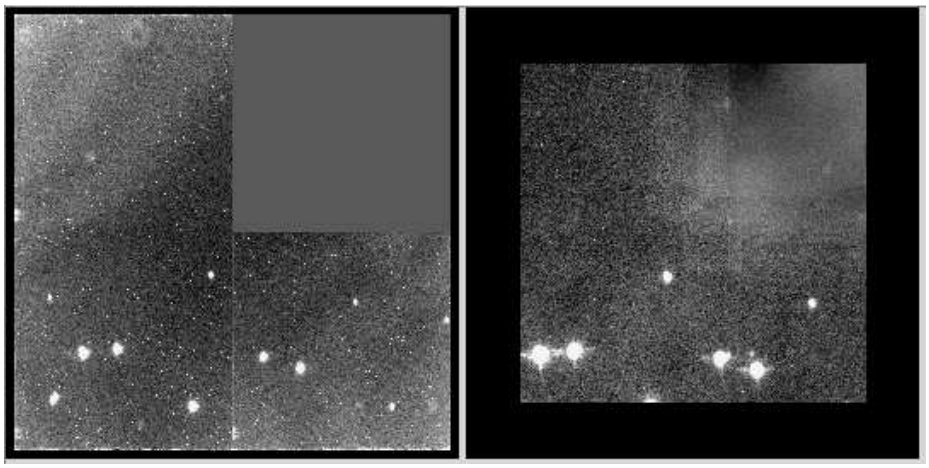

Figure 5: *J*-band Bad Quadrant Dither and Co-Added Image. The left side of the image shows the first dither of the image after the pixels in the bad quadrant have been replaced by the median of the rest of the image. The co-added image, on the right, includes seven dither frames.

For images obtained between 2004 January 22 and 2004 November 30, the top-right quadrant of the NIR detector of ANDICAM did not work, affecting the end of the `I` and all of the `II` ANDICAM observing campaigns. The reduced field of view limited the number of useful comparison stars in the field of view used to obtain the differential magnitude of the target star. Furthermore, we had to ensure that neither the target nor the comparison star fell within the bad quadrant in any of the dithers. The bad quadrant has a constant count level similar to the that of the darks, lowering the median of the entire image. Thus before undertaking the reduction of these images, we replaced all the pixels in the bad quadrant to have a count level equal to the median of the other three quadrants.

II.2 The BVI_C Photometric Observations

This section describes the BVI_C photometric data used to create the BVI_C light curves.

Both of the eclipsing systems were discovered during the photometric variability survey of an area of $40' \times 80'$ centered on the Orion Nebula (Stassun et al., 1999). Par 1802 and 2M0535−05 were observed during this $I_C$band survey from 1994 December 11 through 1994 December 27 using the Kitt Peak National Observatory 0.9-m and Wise Observatory 1.0-m telescopes. Follow-up observations in the BVI_Cbands were acquired and include data from the WIYN[5] 0.9-m and the SMARTS 0.9-m, 1.0-m and 1.3-m telescopes. The observations were obtained in queue observing mode in

[5]http://www.noao.edu/wiyn/

the case of ANDICAM data, and during intensive observing campaigns lasting from a few days to a few of weeks for the other telescopes. The BVI_C data from the different telescopes are reduced following the standard process for optical images, bias subtraction and flat-fielding.

The observing campaigns in all bands are described in detail in Sections V.1.1 and VI.1, for Par 1802 and 2M0535−05 respectively.

II.2.1 ANDICAM BVI_C Data Processing

As mentioned in Section II.1, ANDICAM simultaneously takes images in the optical channel along with the NIR frames. These parallel observations were done for the most part in the I_C filter, centered at 786.5 nm. In the case of Par 1802, observations were also acquired in the BV filters, with central wavelengths of 445 nm and 551 nm, respectively. The $I_C$band is at the reddest-end of the optical wavelength range. Because the detector collects the I_C light in the optical channel and its data reduction process is the same as for VB filters, we will consider the BVI_C data to be *optical*.

Unlike the JHK_S data, ANDICAM optical data is not pre-processed at CTIO. A data reduction pipeline has been implemented by the SMARTS team at Yale, utilizing the NOAO `IRAF` package and the task `CCDPROC`. The pipeline subtracts the bias based on the overscan columns and a zero frame. This zero frame is composed of 10 zero-second exposures with the shutter closed that record the two-dimensional bias due to the detector's readout process. The final step in the reduction pipeline is the division of the image by a normalized dome-flat. The calibrated images are then distributed

to the observers.

II.3 The Spectroscopic Observations

This section describes the spectroscopic observations that were used in the analysis of both eclipsing binary systems. The data are described here to provide context for the analysis for which they are being utilized.

The reduction of spectroscopic data is done to obtain a one-dimensional spectrum of the target from the image with which radial velocities may be measured. The standard process starts with bias subtraction and flat-field correction using calibration frames typically obtained at the beginning of the observing night. The next step consists of tracing the target spectrum on the image and extracting the pixels that contain it. The sky contribution is then subtracted from the spectrum. The wavelength solution of the image is then calculated based on arc lamp spectra typically obtained immediately before and after the science images.

II.3.1 Spectra of Par 1802

The radial velocities for the components of Par 1802 are obtained from two sets of spectroscopic observations: one with the Hydra Multi-Object Spectrograph (MOS; Barden and Armandroff, 1995) at the 3.5-m WIYN telescope, and the second with the High Resolution Spectrograph (HRS; Tull, 1998) at the 9.2-m Hobby-Eberly Telescope[6] (HET). Additional details of these spectroscopic observations and reduction

[6]http://www.as.utexas.edu/mcdonald/het/het.html

analysis can be found in Cargile et al. (2008).

Par 1802 was observed on 8 nights between 1997 January and 2004 December with the Hydra MOS, a fiber-fed spectrograph that allows up to 93 objects to be observed over a $60'$ field. The spectra of Par 1802 were centered at 6400 Å, which corresponds approximately to the R_C band; the spectra span the range from 6250 to 6550 Å, and have a resolution of R $\approx$ 12,000. The signal-to-noise ratio is about 20 per resolution element. The reduction of the data was done using the `IRAF` task `DOHYDRA`. The wavelength calibration was done based on the spectra of a Th-Ar arc lamp, taken with the same fiber configuration as for the target observations. Several fibers were pointed at blank parts of the nebula, and for each target observation, they were combined by their median to create a signature of the sky, including both the nebular and sky emission. This composite "sky" contribution was subtracted from the corresponding target spectra. The results of the sky subtraction were not optimal because the nebula emission varies on a small-scale, and thus, the "sky" does not represent exactly the nebular and sky contribution in the spectra of Par 1802. The non-optimal sky subtraction causes the radial velocity measurements to be less precise. The radial velocity standard used for the cross-correlation analysis, described in Section III.2.1, is the M2-type star, GJ 411, observed by Rhode et al. (2001) with same instrumental set up.

The ten spectroscopic observations of Par 1802 were obtained with the HRS in queue observing mode from 2003 January to 2004 January. The HRS is a fiber-fed, cross-dispersed, echelle spectrograph that allows for the observation of a single object

with dispersed sky spectra in between the target's orders taken through separate sky fibers. Each observation of Par 1802 was divided into two exposures of 1650 s with an average signal-to-noise ratio of $\sim$ 50. They are centered at 6948 Å and span the range from 5263 to 8915 Å and have a spectral resolution of R $\approx$ 30 000. Each spectrum is imaged onto two chips, with 30 spectral orders on the blue chip and 17 on the red chip. The red chip exhibits fringes rendering those orders unusable for radial velocity measurements. Along with every observation of Par 1802, calibration spectra of a Th-Ar arc lamp and of the radial-velocity standard HD 26162 (Famaey et al., 2005) were obtained. The reduction of the spectra was done with the `IRAF` tasks `CCDPROC` and `ECHELLE`, and consisted of the following steps: subtracting the bias, flat-fielding, applying a mask for bad columns, tracing the sky and target orders and subtracting the sky. The wavelength calibration was done by identifying $\sim$ 525 features in the Th-Ar spectrum and fitting a fourth-order polynomial in both the dispersion and cross-dispersion directions. Cosmic ray removal was done by rejecting deviant pixels when the two separate exposures were co-added. The templates used for the cross-correlation method were of spectral types K2, K3, K5 and K7. Additional observations of stars, with spectral types M1 and M2, were obtained and utilized for a two-dimensional cross-correlation of the spectra of Par 1802 to obtain the flux ratio of the system.

A single spectrum of Par 1802 was observed with HIRES (Vogt et al., 1994) at the Keck-I[7] 10.0-m telescope on the night of UT 2007 Oct 23. HIRES is a grating

[7]Time allocation through NOAO via the NSF's Telescope System Instrumentation Program

cross-dispersed, echelle spectrograph; it was used in its HIRESr configuration. This "red" configuration has a cross disperser designed to be most efficient at wavelengths longer than 5 000 Å as compared to its "blue" cross disperser. The OG530 filter was used to block the blue orders. One 900 s exposure of Par 1802 was obtained in between Th-Ar arc lamp calibration images. We used 21 spectral orders ranging from 5782 to 8757 Å. The resulting resolution power was of $R \approx 34\,000$ with a S/N of $\sim$ 70 per resolution element. Additionally, two late-type spectral standards, M1.5 and M3 (Kirkpatrick et al., 1991), were observed. The reduction was done using standard `IRAF` tasks and the reduction package MAKEE designed specifically for HIRES data by T. Barlow. The first step of the reduction is the flat-fielding followed by the determination of the trace of each of the echelle orders. The spectrum extraction is performed by determining the background levels for each order optimally, followed by the wavelength calibration. This data is used for the measurement of the veiling in the spectrum of Par 1802, and is described in Section V.1.3.

II.3.2 Spectra of 2M0535−05

The spectroscopic observations for 2M0535−05, from which radial velocities were measured, were acquired using the Phoenix instrument on the Gemini South[8] 8-m telescope. Phoenix is a long slit, high resolution, infrared spectrograph. Its spectra are single-order and cover a very narrow wavelength range. Observations were centered at 1.555 μm (Hband) and ranged from 1.5515 to 1.5585 μm, with a resolving power of R

(TSIP).

[8] http://www.gemini.edu/

$\approx 30\,000$. The exposure times ranged between 1 to 3.3 hours. Calibration spectra of a Th-Ne-Ar arc lamp were obtained in between science exposures. The radial velocity standard HD 50778, a K4III star (Setiawan et al., 2003), was observed to ensure the instrument's stability and to determine absolute heliocentric radial velocities. Additionally, observations of late-type standards with spectral types between M0 and M9 (Kirkpatrick et al., 1991) were acquired with the same instrument setup.

The standard reduction of these spectral images was done using Interactive Data Language (`IDL`) procedures. A sky subtraction was done from the background contribution surrounding the target spectrum. The wavelength solution was determined from the calibration spectra of the Th-Ne-Ar arc lamp. The attained signal-to-noise ratio per resolution element is ~ 15 for 2M0535−05 and ~ 50 for standard stars.

The details of these observations and their processing can be found in the paper by Stassun et al. (2007).

CHAPTER III

LIGHT AND RADIAL VELOCITY CURVES

This chapter describes the generation of data curves from the reduced observations described in the previous chapter. Light curves are produced from the BVI_CJHK_S photometric data; the radial velocity curves are obtained from the spectroscopic observations.

III.1 Generating the Light Curves

This section describes the creation of the light curves after the photometric data are reduced. Typically, light curves are given in units of magnitude as a function of Heliocentric Julian Dates (HJD), which denote the time of the event as would be measured from the center of the Sun. This correction accounts for the light travel time between the Earth and the Sun.

Photometry refers to the measuring of the amount of flux received from an astronomical object; its light curve describes the measured flux over a period of time. The light curves of eclipsing binary systems are characterized by showing periodic decreases in brightness as one component of the binary passes in front of the other blocking its light.

Fundamentally, there are two types of photometry: differential and absolute photometry. Both compare the observed fluxes of the target to those of reference stars;

the variation in the target's magnitude due to external factors, like the weather and observing conditions, is accounted for and only the intrinsic variability of the target star remains in the light curve.

Differential photometry of point sources enables us to measure the apparent magnitude of the target star with respect to one or more reference stars in the same field of view. Since the target and the comparison stars are close to each other, it is reasonable to assume that any atmospheric extinction variation between the target and the comparisons is negligible. Absolute or all-sky photometry is done by comparing the target star to a set of stars whose flux has been carefully measured, known as standard stars. Because the target and the standard stars are not generally located within the same field of view, careful atmospheric extinction corrections need to be implemented. In general, differential photometry provides more accurate light curves than absolute photometry when measuring small variations, because of its relative simplicity as compared to absolute photometry.

Aperture photometry is one of the methods used to obtain the differential brightnesses of sources in an image. The signal from the source is estimated by defining an aperture around the star, adding the counts in each pixel, and subtracting the background level. No assumption is made about the shape of the light source. It works best for uncrowded fields with little or no overlapping of sources, like the NIR fields of Par 1802 and 2M0535−05 which contain about 10 stars.

A second method that may be used to measure the brightness of stars in an image is based on fitting their point-spread function, or PSF, to an analytical function or an

empirical PSF. The PSF depends on the telescope's diffraction pattern, focus, guiding, seeing, observing conditions, and aberrations; it may change with every image. PSF fitting requires fields with enough of stars to be able to closely characterize the true PSF of the stars in the image. One of its greatest advantages over aperture photometry is that it allows for independent brightness measurement of sources that may be overlapping.

We used different techniques to create the JHK_S and the BVI_C light curves. Aperture photometry was applied to the JHK_Simages because they contain only about 10 point sources. The PSF fitting technique was used for the BVI_C images. They have a larger field of view and thus more point sources that can be used to characterize the PSF of each image.

III.1.1 JHK_S Light Curves

We applied aperture differential photometry for the creation of the JHK_S light curves of Par 1802 and 2M0535−05.

The full width at half-maximum (FWHM) of the point sources is typically 1.1–1.5″, corresponding to $\sim$ 3–4 pixels in the reduced images. The FWHM changes with observing conditions and is consistently different in each NIR filter even for consecutive observations, decreasing with increasing wavelength.

For the aperture photometry of our target and comparison stars, we use the `IRAF` package APPHOT. We selected the aperture to be circular with a radius of 6 pixels, about two times the typical FWHM. The contribution of the sky is calculated by

fitting for the intensity-weighted mean within an annulus around the point source extending from 14–20 pixels. Pixels within this annulus with counts outside the bounds of the detector's linear response range and those that are more than three sigma above or below the sky-mean are rejected before any fitting. The centroid of the distribution is fitted iteratively by rejecting the pixels that deviate from the sky value. The final sky value is then subtracted from each of the pixels within the target's aperture.

The differential photometry requires at least one comparison star for each of the objects. To create the differential light curves after the raw aperture photometry is done, the target's measured flux is subtracted from the comparison's and that difference is converted into differential magnitudes. The time of this measurement is corrected for the total integration time. In the case of Par 1802, each of the five dithered images that compose one J observation had an exposure time of 30 s adding to an integration time of 150 s. The HK_S observations had a total exposure time of 175 s and were composed of 7 dithers of 25 s each. In the case of 2M0535−05, each JHK_S frame was 70 s adding to 490 s per observation. The time of observation was set to the midpoint of the total exposure time, and was converted into Heliocentric Julian Dates using the `IRAF` task `SETJD`.

The comparison stars of Par 1802 and 2M0535−05 were chosen because they were always present in the field of view and because their I_C-band light curves did not present significant variability. The comparison stars of Par 1802 and 2M0535−05 are also not found to be variable in the NIR by Carpenter et al. (2001), in time

scales of a few days, months and up to two years. By using a single reference star to obtain differential photometry, we are more susceptible to the intrinsic variability of the comparison star. However, since the BVI_C light curves, as described in the next section, use a reference star formed from the average of the stars in the field, they allow us to assess the variability of the stars used in the JHK_S light curves as comparison stars independently. Moreover, the I_C light curves of the comparison stars were searched for periodicities, following the procedure described in Section IV.1, and none were found.

In fact, both comparison stars have been shown to be non-members of the Orion Nebula Cluster (ONC) to which both eclipsing binary systems belong. Since they are not part of the pre-main sequence stellar population, they are less likely to be intrinsically variable. Par 1802's comparison, Parenago 1810, was found to have a proper motion distinct from the other stars in the ONC by Hillenbrand (1997). The comparison star for 2M0535−05, 2MASS J05352007-0545526, was shown to not have Hα emission and to have a heliocentric radial velocity inconsistent with the ONC population (Fűrész et al., 2008). Moreover, it was was found to be a non-member based on its position on the HR diagram (Frasca et al., 2009).

The uncertainty in the JHK_S light curves is estimated from the scatter in the out-of-eclipse (OFE) phases. Figure 6 shows the OFE phases of the light curve delimited by the vertical lines. The OFE phases are between ~ 0.05 and ~ 0.45, and between ~ 0.55 and ~ 0.95. The standard deviation of the rectified light curves in the OFE phases, i.e., after all periodic signals found in the data have been removed

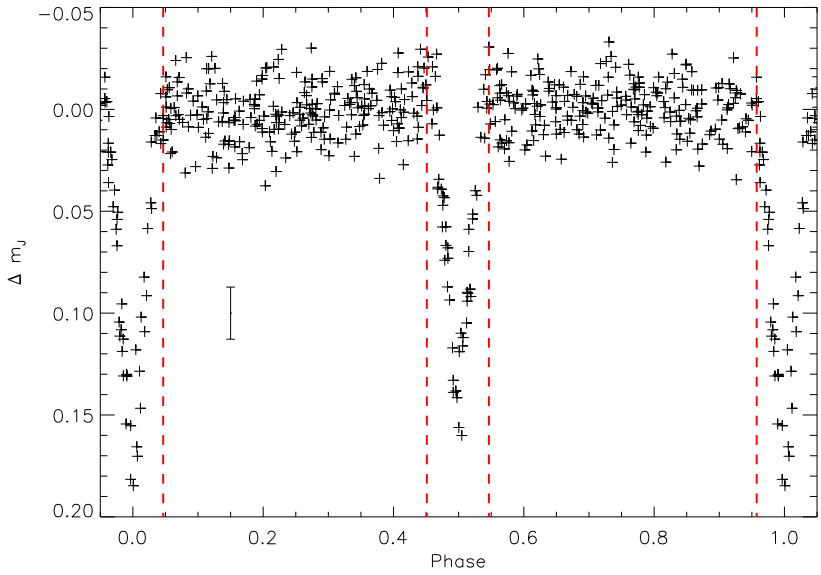

Figure 6: Rectified, Out-of-Eclipse J Light Curve. Using the Jband of Par 1802 as an example, the Out-Of-Eclipse (OFE) light curve is found between the phases of $\sim$ 0.05 and $\sim$ 0.45, and between $\sim$ 0.55 and $\sim$ 0.95. The OFE phases are separated in the figure from the eclipses by the vertical, dashed (red) lines. The uncertainty in the JHK_S light curves is given by the scatter of the rectified data in the OFE phases, and is shown by the error bar at a phase of 0.15.

(see Section IV.1), is used to measure the photometric uncertainty. The uncertainty in the light curves is dominated by systematic uncertainties, not by the error in the aperture photometry which includes the error in the determination of the flux, the sky, and the aperture of both the target and the comparison stars. Figure 7 compares the errors from the aperture photometry in the JHK_S-bands (left-side panels) to the residuals of the light curve modeling (right-side panels; see Section IV.2 for modeling). This figure shows that the scatter in the OFE light curves (vertical dotted lines) is an adequate estimate of the photometric uncertainty, more so than the errors from

the aperture photometry (vertical dashed lines).

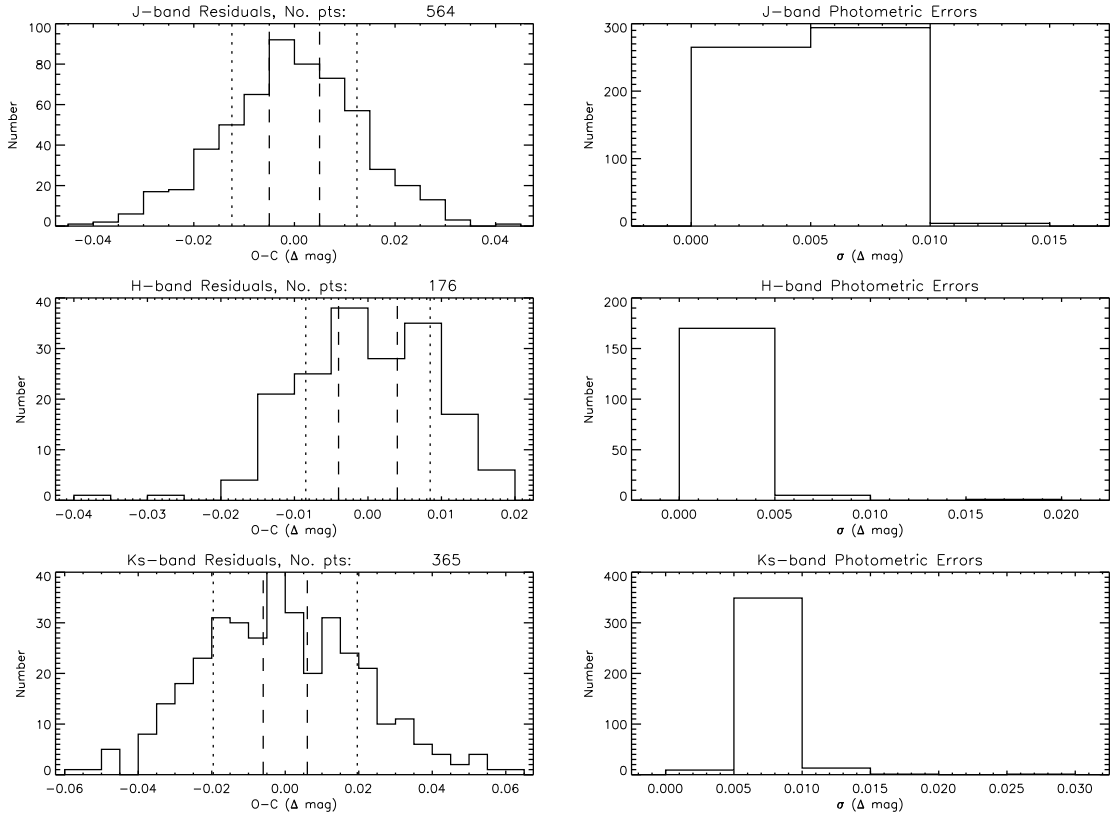

Figure 7: Histograms of the JHK_S Light Curves' Residuals and Photometric Errors. The left-side panels show the histograms of the residuals of the eclipsing binary model to the JHK_S light curves, from top to bottom. The vertical dashed lines represent the median photometric error. The vertical dotted lines represent the standard deviation in the OFE data for a given light curve. The right-side panels show the histograms of the photometric errors. All histograms have a bin size of 0.005 magnitudes. This figure is shows the data of Par 1802.

III.1.2 BVI_C Light Curves

The optical light curves are created using a differential PSF fitting photometry technique as described by Honeycutt (1992) for inhomogeneous ensembles. This technique does not require a particular set of comparison stars nor it requires the stars to be present in every frame.

Raw BVI_C light curves for stars on the reduced images were obtained by fitting the stars' PSF to an empirical PSF using the `IRAF` task DAOPHOT. The optical fields of view for both our targets contain a few tens of stars. After obtaining these raw light curves, the magnitudes are compared to an assigned reference magnitude based on observations taken with the best seeing and atmospheric transparency. This allows for the calculation of an ensemble average created from the magnitudes of the stars on each frame. Stars that deviate greatly from the ensemble's average are removed from the calculation in an iterative process. Differential light curves of the target star are then determined with respect to the mean magnitude of the stars in the field. The uncertainty of each magnitude measurement is given by the scatter of the measurement for sources of similar brightness.

III.2 Radial Velocity Curves

The velocity of any astronomical object can be separated into two perpendicular components: one parallel to the line-of-sight, known as radial velocity (RV), and the other parallel to the plane of the sky. A positive RV signifies that the object is moving away from the observer; while a negative RV means that it is approaching the observer.

Fundamentally, radial velocities of stars can be measured by comparing the Doppler-shifted wavelength of the observed spectral lines to their rest-frame wavelengths.

As the components of a binary system revolve around their common center of mass, the spectral lines may show a continuous and periodic shift in wavelength. The spectrum of a single-lined spectroscopic binary exhibits the spectral lines of only one star with this periodic change, and provide its RV measurements. In the case of a double-lined spectroscopic binary, there are two identifiable sets of spectral lines, one for each component, that are shifting as they orbit. In this case, radial velocities can be measured for both components, allowing for the ratio of the masses to be ascertained. Both Par 1802 and 2M0535−05 are double-lined, eclipsing binary systems; their mass ratios are directly determined from the ratio of their RVs at any given orbital phase. The determination of the physical parameters of a double-lined eclipsing binary system by modeling its radial velocity and one or more light curve is described in detail in Chapter IV.2.

There are several techniques for determining the radial velocities of binary components from a one-dimensional spectrum. They are based on the comparison of the observed spectrum of the binary to template spectra.

One of the techniques used to measure RVs estimates the cross-correlation function (CCF) between the observed spectrum and a template spectrum, and is described in detail by Tonry and Davis (1979). The peak of the CCF corresponds to the relative shift in radial velocities of the observed spectrum with respect to the template. In the case of double-lined spectroscopic binaries, the CCF has two peaks and typically

the more significant peak corresponds to the RV of the primary component. Cross-correlation is a one dimensional technique, introducing systematic errors into the RVs of both components in a double-lined spectrum when the lines are blended, i.e., when the components are near conjunction. By applying this method, the RVs of Par 1802 were measured on the WIYN/MOS and the HET/HRS spectroscopic data as described below in Section III.2.1.

Another method based on the CCF is the algorithm TODCOR (Zucker and Mazeh, 1994), specifically designed for the extraction of radial velocities from double-lined spectra. It calculates a two-dimensional CCF of the observed spectrum against combinations of two templates. The templates can be of different spectral types; however, this introduces a strong dependence on the luminosity ratio between the two templates. TODCOR is able to minimize for the intensity ratio, assuming that the spectral templates used correspond closely to those of the binary components. The highest peak of the two-dimensional CCF determines the RVs of the primary. Those of the secondary component are given by the lower peak. This technique may be applied iteratively with tomographic reconstruction of the spectra to refine the flux ratio of the system, like in the case of Par 1802 as described in SMC08.

A third technique to measure RVs estimates the broadening function (BF) using least-squares fitting, and is described by Rucinski (1999). The BF is the function by which a standard template spectrum with sharp lines is transformed into the observed spectrum of the binary. The BF method requires a template that is closely matched to the target spectrum. This method relates directly the absolute RV of the target

star to that of the standard. The RVs are measured by simultaneously fitting a Gaussian to as many spectral features as are identified in the BF. This method is used to measure the RVs of 2M0535−05 (see Section III.2.2) and is less sensitive than the CCF technique to systematic errors in the RV determination when the velocity separation of the components is of the order of the spectral resolution.

III.2.1 Radial Velocities of Par 1802

The radial velocities of Par 1802 were measured via the CCF method, applying the `IRAF` task FXCOR to the data from WIYN/MOS and HET/HRS (See Section II.3.1). The measurements presented here are described in detail by Cargile et al. (2008).

The WIYN/MOS data was cross-correlated with the M2-type RV template using the `IRAF` task FXCOR and producing a single CCF which was fitted to a Gaussian. The radial velocities for a given observation are given by the centroids of the Gaussian fit. The formal uncertainties are determined by the r statistic, which depends on the characteristics of the CCF. The typical uncertainties of the measured RVs are ~ 3 km s^{-1} for this data set.

The HET/HRS data was cross correlated with different templates of late type stars. The spectral orders were cross-correlated independently, and the resulting CCFs were added, excluding the CCFs that did not show two clear peaks. The strongest CCF peaks were obtained for the K7 spectral type. The radial velocities were obtained by fitting both CCF peaks to Gaussians. The uncertainties in the RVs

were determined by the statistical error in the Gaussian's centroid. The orders that contained broad spectral features, like the nebular Hα emission were not included in the cross-correlation.

III.2.2 Radial Velocities of 2M0535−05

As mentioned above, the RVs of the components of 2M0535−05 were obtained via the BF method Stassun et al. (2006, 2007). The absolute heliocentric RVs of the observed late-type standard stars are obtained relative to the RV standard HD 50778 (K4). To avoid systematic uncertainties in the absolute RV determination introduced by a difference in spectral type between HD 50778 and the M-type standards, the velocity corrections found by cross-correlation were applied sequentially. The BF technique was then applied for the observed spectra of 2M0535−05 with respect to the observed M-type standards. The highest peaks for both components in the BF were found using the M6.5 template. Using the M6 and M7 templates caused the peaks to weaken by $\sim$ 20%; later and earlier spectral types caused weaker peaks. This suggests that the components of 2M0535−05 have similar spectral types, which is confirmed with the effective temperature ratio of almost unity found from the eclipsing binary modeling. The flux ratio between the binary components is estimated from the ratio of the area under the BF peaks when the primary and secondary are at maximum separation (see Fig. 8). This is a valid estimate in the H-band at which the observations were taken because both components have similar spectral types.

The radial velocities for each component are measured by fitting a two-Gaussian

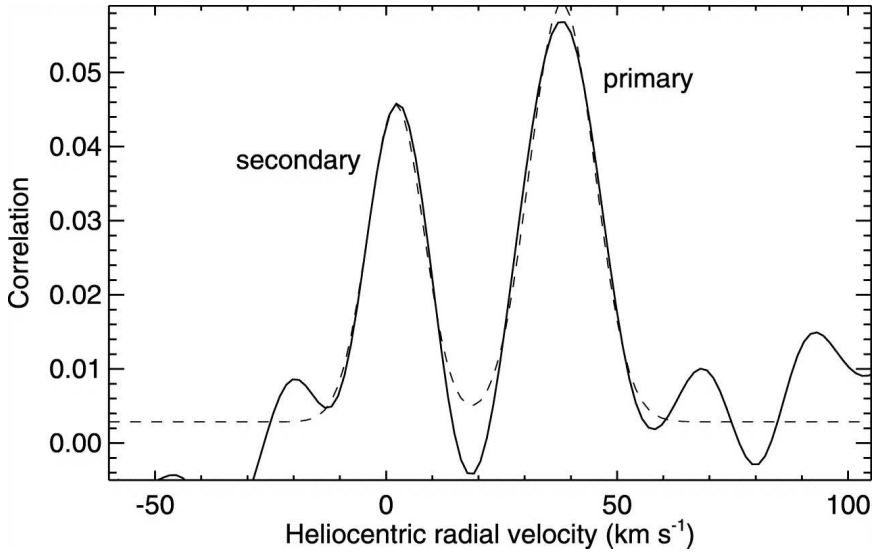

Figure 8: RV Determination via the Broadening Function. The BF for the spectrum of 2M0535−05 and a M6.5 template is shown by the solid line; the orbital phase of the system is when the components are near their maximum velocity separation. The dashed line is the two-Gaussian fit to the BF, from which the radial velocities are measured. This plot is Figure 1. from Stassun et al. (2007).

function to the BF of 2M0535−05 for 7 of the 9 observations. One observation was taken at the time of primary eclipse, so the BF was fit to a single Gaussian and the RV was assigned to the secondary component. The other observation was taken closely after the secondary eclipse, so the resulting BF was single-peaked. The RVs were measured by fitting two Gaussian functions of fixed widths, based on the widths of the two-peaked BFs at other orbital phases.

CHAPTER IV

METHODOLOGY OF THE ANALYSIS

IV.1 Periodicity

This section describes the characterization of periodicities in the light curves.

One of the characteristics of Pre-Main Sequence stars is that they are variable. Their variability may be intrinsic, i.e., due to physical changes in the star like pulsations, or extrinsic, due to their rotation or orbital motion. The variability can be periodic, as in the case of eclipsing binaries, or eruptive, like in flares in T Tauri stars. Identifying and determining the properties of the variability of PMS stars provides insight into the physical properties of the system. Once the periodicity has been identified, it is common to fold the light curves to display the variability as function of phase, where one phase is the length of time over which the periodic signal occurs once.

IV.1.1 Orbital Period Determination

Eclipsing binaries show periodicity in their light curves as the observed light from the system decreases when one component eclipses the other and in their radial velocity curves due to the orbital motion of the components around their common center of mass. Both of these periodicities depend directly on, and therefore contain information about, the orbital period. The photometric variability to the orbital motion is

not sinusoidal in nature for detached eclipsing binaries. The variability in the radial velocity curves due to the orbital motion is sinusoidal if the orbit is circular; as the eccentricity increases, it becomes less sinusoidal.

To determine the orbital periods of Par 1802 and 2M0535−05, we use the I_C-band light curves. In both cases, it is the light curve that has the longest time span and the greatest number of data points. We did not search the radial velocities for periodicities to determine the orbital period because the light curve provides about two orders of magnitudes more data points.

We used a Phase-Dispersion Minimization (PDM) technique described by Stellingwerf (1978) to determine the orbital periods of the binaries. This period searching method does not make any assumptions about the shape of the periodicity, and thus is well suited for detecting non-sinusoidal periodicities. This period searching method compares the overall variance of the data with the variance of the data folded over different trial periods. If the data do not contain a periodic signal at the trial period, then the data will be randomly distributed and the variance would be comparable to the overall variance of the data. When the data are tried against a true period, the dispersion will be reduced and the ratio of the overall variance with the variance of the data will be small. In a plot of trial frequency or period versus the ratio of the variances, real periods and their aliases will be shown by dips. The depth of a dip gives a measure of the significance of the associated period in the data.

Aliases are the result of the temporal sampling of the data. The gaps in the data acquisition create a certain degree of regularity in the observations. For example,

data that are observed in consecutive nights will show strong aliases at frequencies of $\pm$ 1 d^{-1}. Aliasing represents one of the main complications in detecting unknown periodicities, since an alias instead of the true period may be identified. In fact, when the PDM technique is applied to eclipsing binary systems it is common to find that the deepest valley in the PDM is at half of the true orbital period. The uncertainty in the period is determined via a *post-mortem* analysis (Schwarzenberg-Czerny, 1991), similar to that described below (see Fig. 12).

PDM is not the only technique that can be used to search for periodicity in data. There are also string-length methods and those based on periodograms, as employed in Section IV.1.2, to analyze the low-amplitude variability in the light curves. A useful tool to assess the determination of the orbital period is the O – C diagram, which compares the observed data against an expected value by presenting the residuals. Its name, O – C, means literally Observed minus Calculated. The shape of the O – C diagram of the times of the primary and secondary minima can reveal whether the orbital period is correct and whether it is constant over time. The calculated time of eclipse t_C is given by $t_C = E + n\ P_{orb}$, where E is the epoch, n is the cycle number and P_{orb} is the orbital period. For example, if the orbital period is correct, then the O – C diagram will present the residuals to be scattered about zero. If the orbital period is correct but epoch is not, then the scatter will not be about zero, and the mean of the residuals will give the correction to E. If P_{orb} is incorrect but constant, then the residuals will be on a straight line with a slope containing the correction of the period. If the O – C plot presents a sinusoid, it may be due to apsidal motion

or light-time effect because of a gravitationally bound third body in the system. We utilize this tool to refine the orbital period of Par 1802, as described in Section V.2.1.

IV.1.2 Low-Amplitude Photometric Variability

Apart from the orbital periodicity discussed in the previous section, we find that the light curves present a periodic low-amplitude variability.

The photometric low-amplitude variability found in the light curves is sinusoidal, which is characteristic of rotational modulation of the light curves by surface spots (e.g., Stassun et al., 1999). Through the periodicity analysis, we are able to measure the photometric rotational period of the eclipsing components. The details of the periodicity analysis of Par 1802 and 2M0535−05 are described in Section V.2.1 and VI.2.1, respectively.

We apply the periodicity analysis only to the out-of-eclipse (OFE) phases of the light curves, i.e., all orbital phases except for the eclipse phases, to exclude the periodicity that the eclipses introduce and to focus on characterizing the low-amplitude variability. Another approach is to search the residuals of the light curve modeling for periodicities, such that any periodic signal due to the binary nature of the system would not be included. As a consistency check, after obtaining a good fit to the light curve modeling, we search the residuals for periodicity to verify that the periods found in the OFE light curves are real and are not skewed by the exclusion of the eclipse phases. However, the bulk of this analysis is done before the best radial and light curve model is reached, allowing the inclusion of the components' rotation periods in

the light curve modeling.

We implement the Lomb-Scargle periodogram technique developed by Scargle (1982) that is well suited for unevenly sampled data. It constructs the power spectra as a function of frequency by fitting sinusoids to the data by the method of linear least squares. The periodograms present the power spectra in frequency (d^{-1}) and show multiple strong peaks. Figure 9 presents the Lomb-Scargle periodogram for the V light curve of Par 1802, as an example. The power of the periodogram is shown by

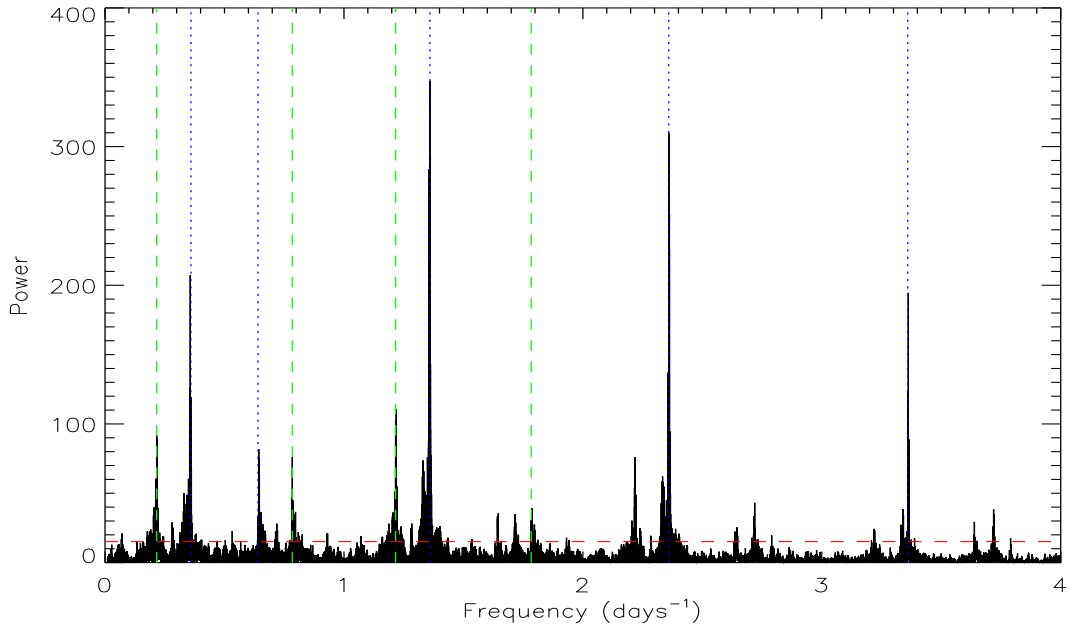

Figure 9: V-band Lomb-Scargle Periodogram of Par 1802. The peaks in the periodogram represent the two independent periodicities and their aliases (dotted and dashed lines). The 1% false-alarm probability (FAP) is shown with the horizontal broken line; periods above of this line have less than a 1% probability of being spurious.

Scargle (1982) to be equivalent to fitting sinusoids to the data by least-squares and is normalized by the variance of the data (Horne and Baliunas, 1986). This allows for the significance of the peaks in the periodogram to be given by the False-Alarm Probability (FAP). This period searching technique assumes that the signal is sinusoidal. However, it is still a valid technique to detect unknown periodicity for highly non-sinusoidal signals, because in principle all periodic signals can be decomposed into a liner combination of sines and cosines.

The FAP describes the probability that for M independent frequencies sampled, a given periodogram power z could be attained in the case that the data are only noise; it is given by P $(> \ z) \equiv 1 - (1 - e^{-z})^M$ (Press et al., 2007). A priori the number of independent frequencies M sampled is unknown, since it depends on the number of frequencies sampled, the number of data points and their temporal sampling. We are able to calculate the FAP for the periodogram of each light curve by using a Monte Carlo method. For each light curve, we create 1000 synthetic signals keeping fixed the number of data points and their time-stamps to keep the window function and the statistical properties of the data the same. This allows us to not make any assumptions about the level of noise in the data. The magnitudes then are randomly distributed to create the new light curves, for each of which, we calculate the Lomb-Scargle periodogram with the same frequency intervals as for the real data. We find the highest peak in each of the resulting 1000 periodograms, and obtain the probability distribution for different peak heights. We fit the distribution to find M and then calculate the 1% FAP level for each light curve. Figure 10 shows the

distributions of maximum periodogram power resulting from the Monte Carlo process in the solid line and the fitted distribution to determine in the dashed line. The data utilized in this figure are the light curves of Par 1802, and are shown here to exemplify the process. The 1% FAP level is shown in Fig. 9 as the horizontal dashed line.

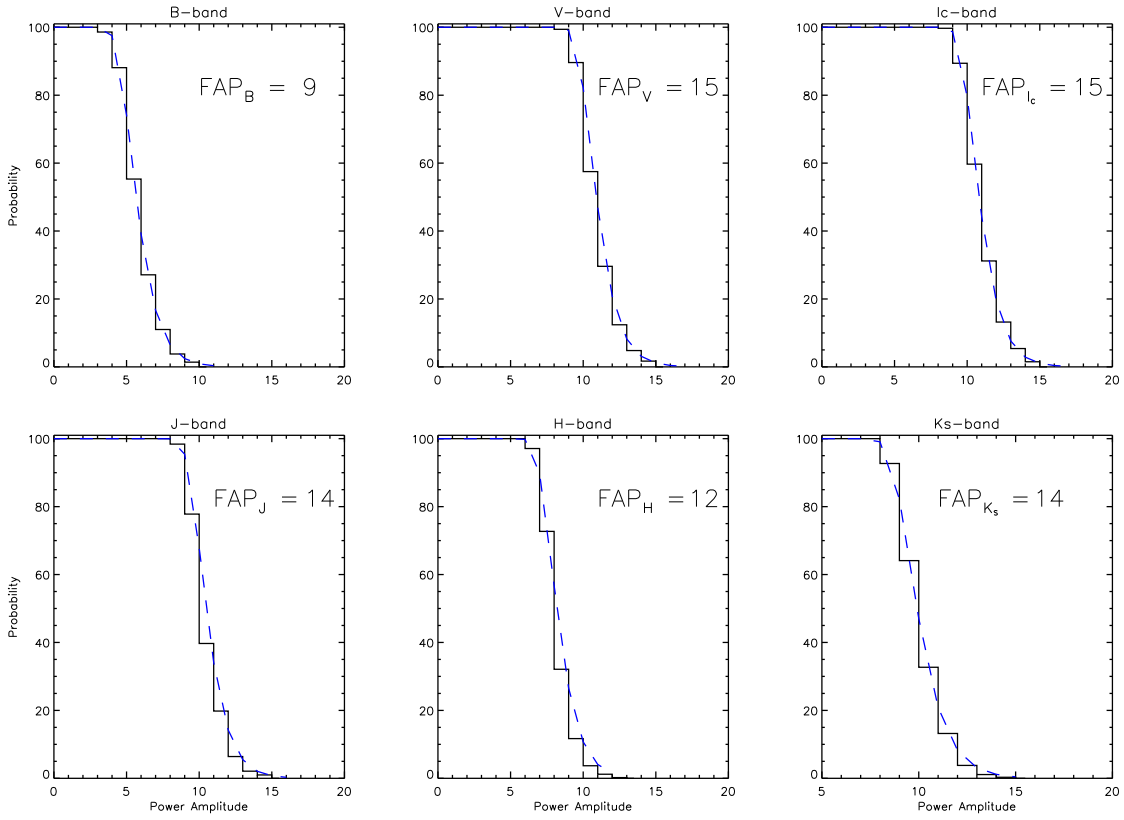

Figure 10: Maximum Periodogram Peak Distribution from Monte Carlo Method. By fitting the resulting distribution of maximum peak heights, shown in the solid line, to an exponential function of the form 1 – (1 - e^{-z})^M, we are able to determine the number of independent frequencies M that best fits each distribution. This best fit is given by the blue, broken line. Consequently, we can obtain the 1% FAP for each light curve.

As mentioned in the previous section, aliases are common in periodicity searches of astronomical observations and may complicate the detection of the true physical period. In order to distinguish the real frequencies from their aliases, additional assessment of the periodograms is necessary. Thus, we fit the OFE data to a sinusoid with a period corresponding to the highest peak in the periodogram via a least-squares method and consequently subtract the sinusoidal fit from the data. We apply the same periodicity analysis to the residuals of this fit, allowing us to identify the set of peaks that depend on the period, including its aliases. If the period that is removed is real, then the peak corresponding to that period is removed from the periodogram along with the peaks of its aliases; see middle panel in Fig. 11. Furthermore, the overall noise in the periodogram decreases. If the period removed is an alias, the noise in the periodogram increases and the removal of the peaks from the periodogram is not as effective; see bottom panel in Fig. 11. This filtering technique also permits us to identify independent periods in the data. When a true period has been successfully removed by the fitted sinusoid and if another independent periodicity exists, then the periodogram will still contain the peaks corresponding to this second period and its aliases. In fact, the peaks may be higher in this periodogram because the removal of the other periodic signal makes the remaining periodicities more significant, as shown in the second panel of Fig. 11. To ensure that both periodic signals are truly independent and that the second identified period is not a result of the filtering process, we exchange the order in which the signals are filtered. We are able to distinguish both periods regardless of the order in which the periodic signals are removed from the

data. The top panel of Fig. 11 shows the Lomb-Scargle periodogram of the J light

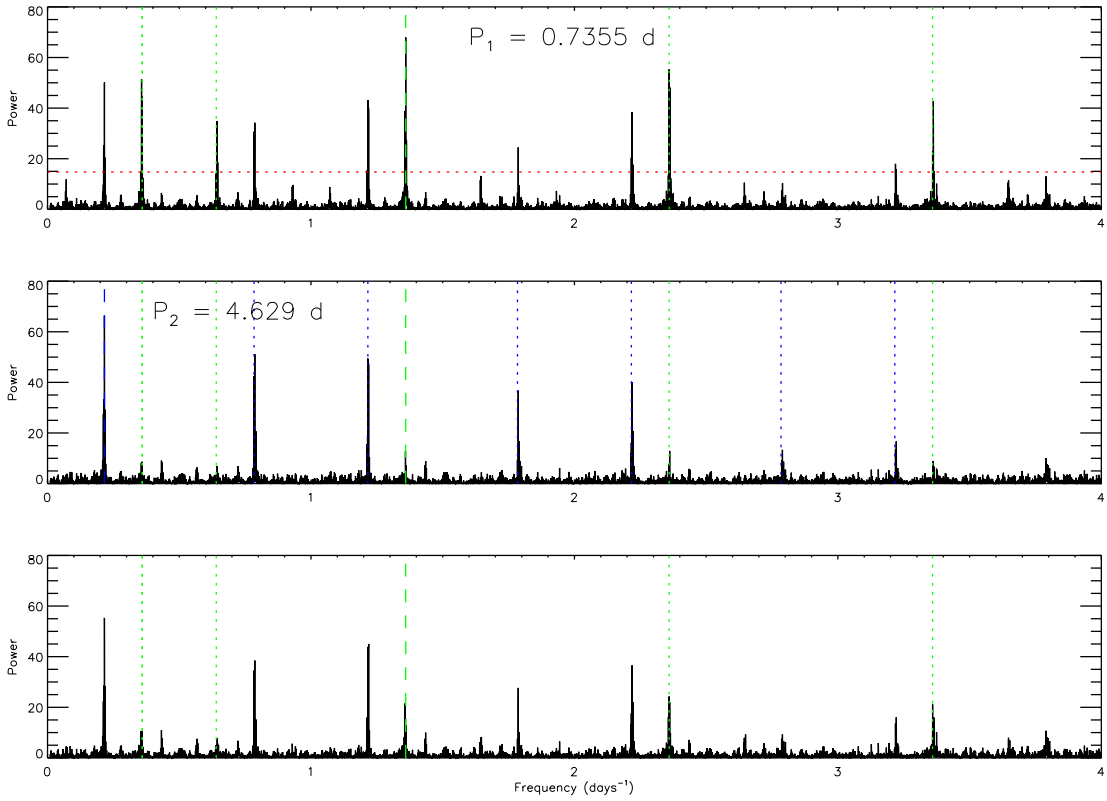

Figure 11: Identifying Independent Periodicities from their Aliases. See text for details.

curve of Par 1802; the 1% FAP is marked by the (red) horizontal, dotted line. The true period, $P_1 = 0.7355$ d, is highlighted with the (green) vertical, dashed line; its aliases are marked by the (green) vertical, dotted lines. The green lines are shown in every panel as a reference. The middle panel shows the periodogram of the residuals when a sinusoidal signal with a period equal to the true periodicity has been removed;

thus, the peaks that correspond to P_1 are well removed from this periodogram. A second independent periodicity is made evident with the subtraction of the first periodic signal; the most significant peak in this periodogram corresponds to a period of P_2 = 4.629 d, and is marked by the (blue) vertical, dashed line with the (blue) vertical, dotted lines as its aliases. The bottom panel shows the periodogram resulting from removing a sinusoidal signal with a period corresponding to the left-most alias of P_1 at frequency of $\sim$ 0.36 d^{-1} from the OFE light curve. Filtering the alias is not as effective in removing the set of periodogram peaks, as is filtering the real periodicity. Additionally, because the available data sets are composed of multi-band light curves,

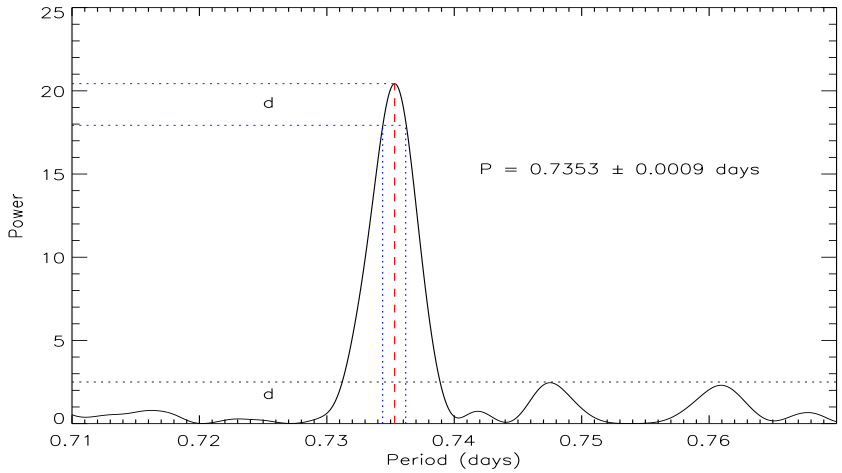

Figure 12: Period Uncertainty via Post-Mortem Analysis. The periodogram of Par 1802's H-band light curve around the most significant period, denoted by the red vertical dashed line, is shown as a function of period. The horizontal dotted line of height d, toward the bottom of the plot, measures the noise in the periodogram around the peak. The uncertainty in the period, marked by the vertical dotted lines. It is given via the *post-mortem* technique by the width of the periodogram peak at a level of d (bottom horizontal, blue, dotted line) from its maximum amplitude (top horizontal, blue, dotted line).

we can compare the periodograms separately to determine which peaks correspond to the real period. This is possible because the window functions of the light curves are not exactly the same. We also analyze each of the observing seasons independently, effectively changing the window function and the resulting aliases. We find generally that the periodic signals change in phase for a given season, but the periods remain consistent with each other. In searching each season independently for periodicities, we have fewer measurements, and we loose frequency resolution because of the shorter timespan of the data. Moreover, we fold the light curves to the significant periods to visually assess their periodicity.

For the different light curves, we find slightly different periods. The uncertainty in the determination of the period from the periodograms is obtained via the *post-mortem* analysis described by Schwarzenberg-Czerny (1991). We calculate the periodogram as a function of period, instead of frequency, only around the period of interest, that was determined from the previous periodograms. First, we estimate the noise level d from the periodogram (see in Fig. 12). The width of the peak at a level d from the maximum height of the peak determines the uncertainty in the period.

The rotation periods of the components are determined by the mean of the periods obtained from each light curve and its uncertainty is given by the uncertainty in the mean. Furthermore, we confirm that these rotation periods are consistent with the measured values of $v \sin i$.

IV.2 Eclipsing Binary Modeling

This section describes the modeling of the eclipsing binary (EB) data with the goal of determining the system's physical parameters, including the characteristics of the orbit and of the stellar components.

IV.2.1 Overview of the Model

The inverse problem for eclipsing binaries is to determine n physical parameters from one or more observed radial velocity (RV) and light curves (LC) and can be formulated as a nonlinear least-squares problem. Because the system is nonlinear and the calculated parameters are correlated, the solution to a given set of observed curves is not unique. A unique solution would correspond to a point in the n-dimensional parameter hyperspace. Instead, the global minimum of the system is a region in the n-dimensional parameter hyperspace; its form and significance depend on the uncertainty in the data and the parameter correlations. The implication of this *solution degeneracy* is that a change in the value of a parameter may be compensated by a change in one or more parameters, rendering solutions that are indistinguishable from each other. Thus, every solution must be examined to ensure that it lays within the system's global minimum and is physically consistent with external observational constraints. The methodology described throughout this chapter aims to reduce the effects of the present degeneracies in our solutions by capitalizing on the diverse available data sets for both Par 1802 and 2M0535−05.

The modeling of the EB systems Par 1802 and 2M0535−05 is done with the

software PHOEBE (Prša and Zwitter, 2005), which is based on the Wilson-Devinney (WD) code (Wilson and Devinney, 1971). WD was developed specifically for the analysis of eclipsing binaries and has been continuously refined since its creation to include more complex treatment of implemented processes, additional constraints and more efficient computations (Wilson, 1979, 1990; Van Hamme and Wilson, 2007). PHOEBE is able to compute radial velocity and light curves from system parameters, which are fitted to the observed curves by minimization algorithms. The minimization algorithms converge by reducing the χ^2 to the fit, and may therefore fall into a local minimum in the parameter hyperspace instead of the solution's deepest χ^2 minimum, or global minimum. The minimization implemented by WD is based on differential corrections (DC), which replace partial derivatives with finite differences resulting in the parameter corrections that reduce the χ^2 of the fit. If the solution does not converge, the method of multiple subsets described by Wilson and Biermann (1976) can be applied. This method divides the parameters in subsets and minimizes for them separately. Furthermore, PHOEBE implements the minimization algorithm Nelder-Mead Simplex, based on function evaluation instead of derivatives. This method is slower computationally, but it is more robust and does not diverge. Moreover, PHOEBE's back-end scripter capabilities facilitate the implementation of heuristic scans of the solutions to explore the parameter degeneracies and avoid local minima.

A model of the observable curves is based on the understanding of the physics and geometry of the orbits and the components, the computation of the local radiative intensity and the computation of the integrated flux in the direction of the observer.

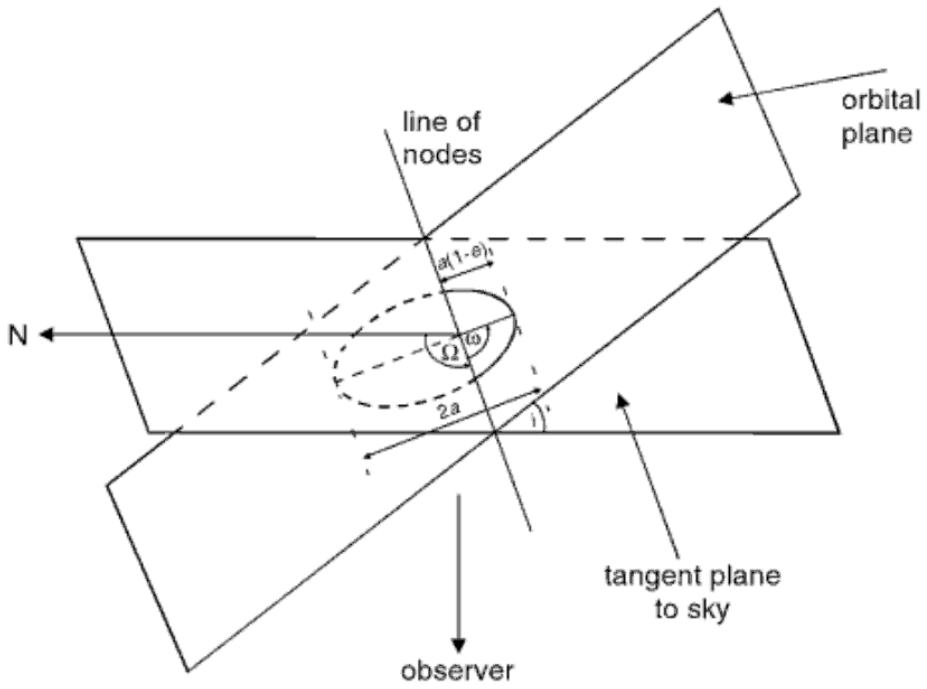

Figure 13: Orbital Geometry and Orientation. Ω is the longitude of the ascending node, ω is the argument of periastron, e is the orbital eccentricity and a is the semi-major axis. See text for details. This figure was adopted from Kallrath and Milone (2009).

The system's orbital geometry can be described in terms of a relative orbit, where the movement of one component is in terms of the other component, as shown in Fig. 13. The orbit's semi-major axis a is equal to the sum of the distances between each component and the center of mass of the system; the orbital eccentricity e lays between 0.0 and 1.0. In the case of $e = 0.0$, the orbit is circular and the components are separated at all times by a. The orbital elements define the orientation of the orbit with respect to a reference, typically the observer. The argument of periastron ω is the angular distance, measured in the sense of the motion of the component, between

the ascending node, i.e., the point in the orbit where the secondary component is moving most rapidly away from the observer, and periastron, the point of closest approach of the components. The ascending node is on the line nodes in which the orbital plane intersects the plane of the sky. The inclination angle i describes the angle between the orbital plane and the plane of the sky; when $i = 90°$, the system is edge-on. The longitude of the ascending node Ω, measured in the plane of the sky, gives the position of the ascending node and is by convention set to zero, because the radial velocities and eclipses are independent to the orientation in this direction.

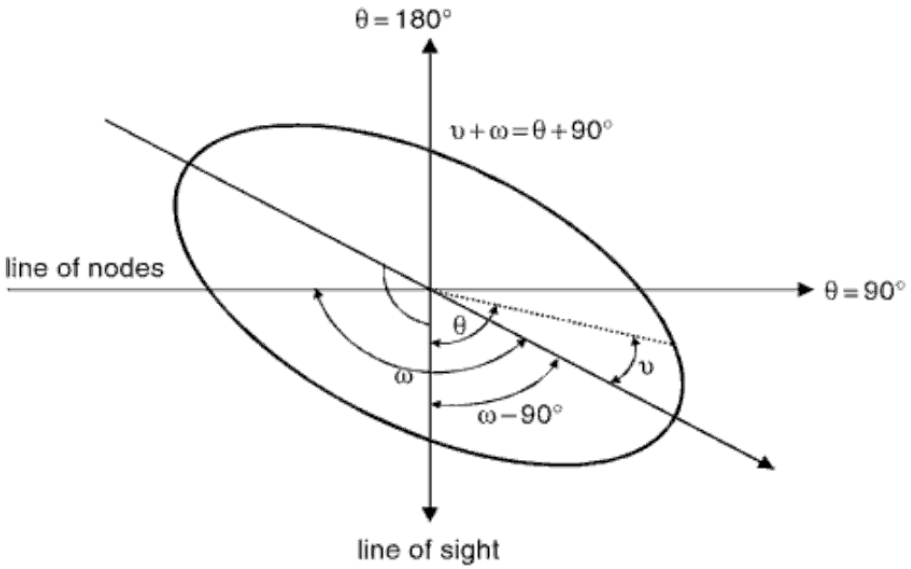

Figure 14: Orbital Phase and Quantities. This figure shows the relationship between the orbital geometric phase θ, the orientation of the orbit (ω) and the position of the star in the orbit measured from periastron, by the true anomaly υ. This figure was adopted from Kallrath and Milone (2009).

The time dependence of the motion of the components of the binary system in

their orbit is given by the orbital photometric phase Φ, i.e., the phase that is observed in the light curves, depends on the orientation of the orbit (ω) and on the position of the star in the orbit, as measured from periastron by the true anomaly υ. For a circular orbit, the relationship between the geometric phase θ and the photometric phase Φ is simply given as $\theta = 360^\circ\ \Phi$. For eccentric orbits, the photometric phase is $\theta = \upsilon + \omega$ - 90°. The relationship between a and the orbital period $P_{\rm orb}$ for an inclined orbit is given by Kepler's third law:

$$\frac{a^3 \sin^3 i}{P_{\rm orb}^2} = \frac{GM \sin^3 i}{4\pi^2} \quad ; \qquad M = M_1 + M_2, \tag{1}$$

where M_1 and M_2 are the masses of the components, M is the total mass of the system and G is the gravitational constant. The ephemeris of the system is determined by a zero-point in time, HJD_0, at which the origin of the ephemeris is set, the orbital period $P_{\rm orb}$, the rate of period change dP/dt, and the phase shift $\Delta\Phi$, which is a constant displacement to the ephemeris (Prša, 2006). By convention, we set HJD_0 to be the time of a primary eclipse. For our systems, the orbital period is constant during the observed timespan, and as such, $dP/dt = 0$.

The points at the surfaces of the stellar components are described by the Roche model, which is based on equipotential surfaces. For a given set of system parameters, the surfaces of the components depend on only the potential energy of those surfaces, and thus the effective surface potentials determine the shape and size of the components. The Roche model assumes that the binary components are point masses surrounded by a massless surface, such that each potential can be described by the gravitational interaction between the components and a centrifugal potential

(Kallrath and Milone, 2009). It also assumes that equilibrium is regained in short timescales when compared to the orbital period. The stars are therefore considered to rotate as equipotential surfaces, without differential rotation. Wilson (1979) showed that an effective potential Ω can be defined and utilized to describe the binary system assuming that the volumes of the components remain constant, even when their shapes depend on where they are in their orbits. We denote the surface potentials as Ω to be consistent with the notation typical in eclipsing binary modeling. Thus, Ω hereafter refers to the surface potentials of the components and is different from the longitude of the ascending node Ω described in the geometry of the system. The surface potential for eccentric orbits and asynchronously rotating components is given in terms of a component's radius R normalized by the semi-major axis ($r = R/a$) by:

$$\Omega = \frac{1}{r} + q\left[\frac{1}{\sqrt{\delta^2 + r^2 - 2\lambda\delta r}} - \frac{\lambda r}{\delta^2}\right] + \frac{1}{2}F^2(q+1)r^2(1-\nu^2), \tag{2}$$

where q is the mass ratio, given by:

$$q \equiv M_2/M_1; \tag{3}$$

and d is the instantaneous separation between the centers of the components ($\delta = d/a = (1-e^2)/(1+e\cos\upsilon)$), F is the synchronicity parameter:

$$F \;=\; \omega_{\rm rot}/\omega_{\rm orb} \;=\; P_{\rm orb}/P_{\rm rot}, \tag{4}$$

and (λ, ν) are the coordinates for points on the stellar surface. The potential with respect to the secondary stellar component is obtain by the change of coordinate system with the origin at the center of the primary component to the center of the

secondary component: $\Omega' = \Omega/q + \frac{1}{2}(q-1)/q$ and $q' = 1/q$.

The radiative properties of the system determine how many photons are emitted and how they are emitted by the components. Stars do not radiate uniformly because of diverse physical effects described below, including distortions due to tidal forces and the rotation of the components. The emergent intensity from each of the components can be described by a simple black body radiation, or it can be based on model atmospheres, like those by Kurucz (1996).

Limb darkening must also be taken into account. The emergent intensity from the center of the stellar disk comes from a deeper layer of the stellar atmosphere, which is at a hotter temperature, than the layer of the atmosphere that is observed toward the edge or limb. Thus the limb of the stellar disk appears to be dimmer than its center. `PHOEBE` allows limb darkening to be modeled by a linear, a logarithmic or a square-root law by interpolating the van Hamme (1993) tables for a given set of system parameters. van Hamme (1993) compared the different limb darkening laws at different wavelengths and for different stellar sources and found that in the ultraviolet range the logarithmic law worked best. The square-root law was best at modeling limb darkening at NIR wavelengths. In the optical range, van Hamme (1993) found that for effective temperatures of $\lesssim$ 9000 K, the logarithmic law was more appropriate; and for effective temperatures of $\gtrsim$ 9000 K, limb darkening was best modeled by the square-root law.

Gravity darkening happens because rotation deforms a star causing the effective gravity and the local temperature at the poles to be higher and thus to make the

polar regions appear brighter than the equatorial regions, as stated by the von Zeipel theorem (1924). Another effect to be considered is the so-called reflection effect in binaries. Contrary to what it has been historically named, it refers to the heating of the surface of the irradiated stars. When the radii of the binary components are $\gtrsim$ 15 to 20% of the orbital semi-major axis (Wilson, 1990), reflection effects become important as the radiation of one component by the other causes the heating of the stellar surface and thus, an increase of surface temperature in the side facing the other component. Furthermore, when the components are greatly distorted, like in the case of contact binaries, the distortion causes a variation in the size of the surface area visible to the observer, which affects the light curve.

Another phenomenon that affects the radiative properties of the binary components is the existence of surface spots. The spots on the components' surfaces can be cold, like those typically attributed to magnetically induced spots, or hot, like those that arise from accretion. A spot is fully described in `PHOEBE` by its position on the stellar surface in colatitude and longitude, its angular radius and its temperature factor, which is the ratio of the spot temperature to the local surface temperature. Spots change the local emerging intensity by multiplying the local temperature by the temperature factor on the surface elements covered by the spot (Prša, 2006). The treatment of spots by `PHOEBE` allows the user to reproduce a large range of light curve effects because of its simplicity, but must be used with reservations. For example, a spot of a given size and temperature factor on the primary may produce similar variations on the model light curves as a group of spots or a single spot on

the secondary component. In fact, a large surface spot spot has a similar effect on the overall emerging intensity than a smaller spot at a cooler temperature. These different scenarios render fits to the observed light curves that are indistinguishable. Without additional observational constraints, like Doppler tomography, it is not possible to determine the true configuration of the spots on the stellar surfaces. From the observed photometric, small-amplitude variations like the ones described above in Section IV.1.2, we are able only to narrow down the spots that reproduce the observed amplitudes to a family of configurations; the details are further explained in Sections IV.2.6 and its implementation in the modeling of 2M0535−05 is in Section VI.3.

An additional source of flux in the light curves that may be extrinsic to the eclipsing components can be modeled as a third light ℓ_3 that is constant in time. The luminosities from the eclipsing components (L_1, L_2) are distinct from ℓ_3. The zero-magnitude m_0 of the system is used in `PHOEBE` to normalize the flux of the light curves. The third light can be modeled in units of flux or as a fraction of the total light of the system. If it is modeled in units of flux, then ℓ_3 is added directly to the flux from the eclipsing components, such that: $(L_1 + L_2)/(4\pi) + \ell_3 = F_s$, where F_s is the flux of the system at, for example, quarter phase. From this relationship combined with the ratio of fluxes: $\ell_3/[(L_1 + L_2)/(4\pi)] = x/(1-x)$, we can obtain the value of ℓ_3 in percentage of the total light of the system. Effectively, additional light in the system makes the eclipses shallower keeping all other parameters constant. The light curve modeling of Par 1802 required the addition of ℓ_3 in order to simultaneously fit

all bands and is described in Section V.2.3.

IV.2.2 Setting Up

This section describes the data and external information and the practical steps that are done to begin the modeling of an EB system with `PHOEBE`, for which the radial velocity (RV) curves of both components and multi-band light curves are available. The RV solution provides the scale of the binary's orbit, and the light curve (LC) solution provides relative quantities, like the components' radii as a function of the semi-major axis of the orbit. The simultaneous solution of both RV and LC provides a consistent solution with a single set of physical characteristics to describe the binary system. This is only a guideline describing in general terms the modeling process of Par 1802 and 2M0535−05; every eclipsing system is unique and its modeling may require the adaptation of the procedure here described. A sample input file is shown in Appendix A, and a script with the commands utilized for the EB modeling using `PHOEBE`'s back-end scripter is shown in Appendix B.

The first step is to create a configuration file with the known parameters of the system. If the system has been analyzed before and a solution is readily available, one may use those values as a starting point for the modeling. Among the initial parameters to be included is the ephemeris of the system: the orbital period $P_{\rm orb}$ obtained from the periodicity analysis of the light curves, as described in Section IV.1.1, and the zero-point of the ephemeris HJD_0. Because the periods of both systems are not found to vary with time, dP/dt is set to zero.

Initial estimates of the eccentricity e and the periastron ω can be obtained from the duration of the eclipses and from their separation in time or orbital phase. For eccentric orbits, the duration of the eclipse that occurs close to apastron (Θ_a), i.e., when the separation between the components is greater, is longer than the duration of the one that occurs close to periastron (Θ_p), i.e., when the components' separation is smaller. The relationship between the duration of the eclipses and the orbital elements e and ω is approximated as (Kallrath and Milone, 2009):

$$e \sin \omega \approx \frac{\Theta_a - \Theta_p}{\Theta_a + \Theta_p} \; ; \qquad \Theta_a > \Theta_p.$$

In general for eccentricities larger than zero, successive primary and secondary minima are not separated by equal lengths of time. The eclipses are symmetrically arranged for circular orbits, or when the semi-major axis of an eccentric orbit coincides with the observer's line-of-sight. The displacement of the minima depends on the eccentricity and the orientation of the orbit as follows:

$$e \cos \omega \; \approx \; \frac{\pi}{2P} \left(t_{\rm II} - t_{\rm I} - \frac{P}{2} \right),$$

where $t_{\rm I}$ is the time of primary minimum and $t_{\rm II}$ is time of the secondary minimum. This relationship is valid for inclination angles close or equal to 90°.

The components are assumed by default to be rotating synchronously with the orbital motion, i.e., their synchronicity parameters F_j are 1.0 (see Equation 4). This is not the case for either Par 1802 or 2M0535−05. Therefore, F_1 and F_2 are calculated from the measured rotation periods $P_{\rm rot,i}$ and $P_{\rm orb}$. If the components are rotating sub-synchronously, the limits of the synchronicity parameter have to be adjusted in

order to fit for F_j; the default upper limit is 1.0, allowing for the slowest rotation to be of a synchronized component.

Generally, an appropriate step size, or increment, when minimizing for the system parameters is about 1% of the parameter value. However, for certain parameters the generalized rule does not apply; such is the case of the inclination angle, for which the step size depends on the particular properties of the binary.

IV.2.3 Radial Velocity Solution

The fitting of the radial velocity (RV) curves was done first in order to obtain from the observed radial velocities the system's mass ratio q:

$$q = \frac{M_2}{M_1} = \frac{K_1}{K_2},$$

where K_j are the semi-amplitudes of the orbit (see Equation 5), and the semi-major axis as a function of the inclination angle of the system (Torres et al., 2010), $a \sin i$:

$$a \sin i = \frac{P_{\rm orb}}{2\pi} \, (1 - e^2) \, (K_1 + K_2).$$

These two quantities, q and $a \sin i$, will remain constant for the rest of the analysis once an adequate RV solution is reached.

The two RV data files are loaded into `PHOEBE`, one for the primary's RVs and one for the secondary's. In fact, `PHOEBE` allows for more than one RV file to be uploaded for each component and one must specify the component for which the measurements apply. Each RV data file is composed of three columns: the Heliocentric Julian Dates (HJD) of the observation, the measured RV and the standard deviation of the

measurement σ_i. The individual weights of the measurements are calculated from this uncertainty, $w_i = 1/\sigma_i^2$. We set the passband sigma σ_p for both curves to 1.0, so that they are weighted equally and each data point is weighted only by its individual weight w_i. The typical definition of σ_p is to set each to the standard deviation of that curve's fit to the data. This is true for σ_p of both RV and LC data.

The passband in which each RV curve was observed is specified, and the appropriate limb darkening law is chosen. Because we are not able to determine the inclination of the orbit i from the RV solution, i is set to 90° and it is not adjusted throughout the RV fitting. Initial estimates of a and q are left at their default values, 10.0 $R_\odot$ and 1.0, respectively. The systemic velocity v_γ is solely determined by the RV solutioni. It is not necessary to estimate a value of v_γ, since its convergence is very efficient. Starting at $v_\gamma = 0.0$ km s^{-1}, the solution converges after just a few iterations.

We mark the parameters to be fitted to the RV curves, $\Delta\Phi$, $a \sin i$, q, v_γ, e and ω, and minimize them using DC as implemented by `PHOEBE` with the default step sizes for each parameter. After each iteration, the corrections to the parameters are verified to make sure they represent a physical solution, and if the solution appears to be converging, we adopt them. Convergence is evaluated quantitatively by a decrease in the fit's cost function χ^2 as reported by the minimization routine; it can also be assessed by calculating with each iteration the rṁs̀óf the model curve to the data (σ_{curve}). The parameter step sizes should be compared to the parameter corrections after a few iterations and modified if needed to aid convergence. Computational accuracy can be increased by refining the numerical grid into which the components'

surfaces are divided and which are used for calculating their physical properties. Once the corrections to the parameters are of the same order of magnitude as the parameter uncertainties, we include the treatment of the proximity effects, i.e., when the stars are close to eclipsing, by modeling the Rossiter effect. The Rossiter effect is due to the rotation of the components which causes the radial velocities to vary because part of the velocity contributions of one of the components are being eclipsed. The solution is minimized again a few more times, evaluating the corrections at each step. When the change in the proposed corrections is not significant, iė; when they are similar to the parameter uncertainties, and when $\sigma_{\text{curve}} \approx \bar{\sigma}_i$, the solution has converged and the data are well fitted; σ_{curve} should not be less than $\bar{\sigma}_i$. It is also important to plot the modeled curve superimposed with the data and to carefully inspect the residuals in case there is an obvious systematic trend.

The attained values for q, v_γ and $a \sin i$ for the RV solution will remain constant throughout our analysis. In particular, the value of a as parameter in `PHOEBE` must be adjusted as the value of i is fitted. This adjustment is done manually with every iteration after which the inclination angle is minimized; thus, $a \sin i$ will be conserved.

IV.2.4 LC Solution

We now fit only the available light curves, excluding the RV data from the minimization, in order to constrain i, the radii R_i and the temperature ratio T_1/T_2, and improve the estimates of e, ω and $\Delta\Phi$.

Like the RV data files, the LC files typically consist of two columns, one for the

HJD of the observation and the second for the measured differential magnitudes; a third optional column, with the measurements' individual uncertainties σ_i, may also be present and if so, it must be specified to `PHOEBE`. In the case of our data sets, the BVI_C LC data did include uncertainties σ_i for each individual measurement; however, the uncertainties in the JHK_S light curves are estimated from the rectified light curves, as described in III.1.1. As mentioned in the previous section, this becomes important when weighting the diverse data curves for the simultaneous fitting. Therefore, we set the passband sigma σ_p of the BVI_C LCs to 1.0, and for the JHK_S LCs to the typical measurement uncertainty, $\sim$ 0.02–0.04, because the σ_i's for the JHK_S data are effectively 1.0.

Because both Par 1802 and 2M0535−05 have well separated eclipses as characteristic of detached binaries, we constrain the system's morphology as such. Since our light curves are differential and not absolute, we set the zero magnitude of the system to 0.0. The temperature of the primary component $T_{\rm eff,1}$ is typically determined from the spectral type or from the fitting of the spectral energy distribution to measured broadband photometry, and then included as a fixed parameter in the configuration file. As a first estimate, the secondary's effective temperature $T_{\rm eff,2}$ can be set equal to $T_{\rm eff,1}$ if $q \approx 1$ and the eclipses are of similar depth. We utilize the values of the parameters resulting from the RV fit, and provide initial estimates for the potentials Ω_i. The inclination angle is set at 89.0° and a is adjusted accordingly.

We then fit for i, $T_{\rm eff,2}$, Ω_1 and Ω_2. As mentioned in the previous section, after each correction in the value of i, a is updated to maintain $a \sin i$ constant. `PHOEBE`

allows for the direct computation of the passband luminosities, instead of minimizing them with DC like the other parameters, which enables a faster convergence of the fitted parameters (Prša and Zwitter, 2005). Therefore, we do not fit for the passband luminosities, but instead we compute them directly after the corrections from the DC minimization are adopted. The same convergence criteria as for the RV solution are applied, including the assessment of the parameter step sizes and the comparison of the model light curves to the photometric data. The passband sigmas σ_p for the LCs should be updated as the solution is improving, by calculating the standard deviation of the fit of the model to the data, $\sigma_{\rm curve}$. Because of the weighting of the curves described above, this is done only to the JHK_S LCs; σ_p for the BVI_Cbands remain at 1.0. Once these parameters have converged, we minimize for the e and ω while keeping the rest of the parameters fixed. Specially at the beginning of the analysis, each iteration has to be assessed carefully to make sure the parameters are not diverging and it is closing into a good fit to the data.

IV.2.5 LC+RV Solution

As mentioned at the beginning of this chapter, the system parameters are correlated and depend on the observables in different ways. So far, we have analyzed the RV and the LC data independently by fitting subsets of the parameters separately to minimize the effects of the solution degeneracy. However, doing the simultaneous fit to all the available RV and LC (RV+LC) data is extremely valuable. Firstly, it ensures that the solution provides a single and consistent set of parameters. This

is particularly important, because there is only one physical system. Moreover, it reduces the number of free parameters in the fitting. Fitting each curve individually could provide different values for the non-wavelength dependent parameters, e.g., i, q, Ω_i, that should be equal within their uncertainties. However, some parameters, in particular e, ω and $\Delta\Phi$, depend on both the RV and LC data, and should be fitted to both types of curves.

We fit e, ω and $\Delta\Phi$ to the RV and LC data, following the convergence criteria mentioned above, and compare at each iteration the modeled RV and light curves to the data. When a good fit is reached, we minimize for i, $T_{\rm eff,2}$, Ω_1 and Ω_2 to only the LC data because they are not determined by the RV curves. We minimize for the system parameters to the LC and the RV+LC fits in alternating order until a consistent set of parameters is attained. The formal parameter uncertainties are obtained from the correlation matrix that encompasses all of the parameters in a single minimization. The corrections to the parameters' values supplied by this final iteration should not be adopted. In the likely case that any of the solutions (RV, LC or RV+LC) contained parameter correlations that caused some of the parameters to diverge and that we have painstakingly tried to circumvent throughout this modeling procedure, the corrections would depart from the converged solution. However, only by including all of the parameters are we able to obtain the appropriate formal errors from the covariance matrix. The determination of more complete and robust parameter uncertainties is described in Section IV.2.8.

It is possible that an adequate fit is not achieved. This could be due to the solution

converging to a local minimum instead of to the system's global minimum; or another possibility could be that the model is not appropriate for the system. In the case of the solution falling outside the global minimum, one could change the subsets of the parameters that are being fitted in order to break the strongest degeneracies between them. In the case of Par 1802, we found that after trying multiple variations of the fitting to find a good solution there was no combination of i, $T_{\rm eff,2}$ and Ω_i that was able to reproduce the observed eclipses. Thus, we include a third source of light in the model light curves to be able to fit all passbands simultaneously. This is not done lightly because of the large degeneracy that is introduced with the inclusion of third light into the EB solution. More details about this analysis are found in Chapter V.

IV.2.6 Including Surface Spots

This section describes the practical aspects of implementing the treatment of surface spots in the light curve modeling. As mentioned above, spot modeling is not well constrained without Doppler imaging of the spots on the star's surface. Furthermore, the system's physical parameters have been shown not to change significantly when analyzing the rectified light curves as compared to the light curves including spots (e.g., Milone et al., 1987). The inclusion of spots in the light curve modeling may be done as an exercise to explain, as in the case of 2M0535−05, an apparent reversal of the temperature ratio of the system as explained in Section VI.3.

`PHOEBE` allows for the modeling of one or more spots in either or both eclipsing components. A surface spot is described by its position on the stellar surface, its size

and its temperature. The position on the surface is determined by the coordinates of spot's center, given in: colatitude θ_{sp}, 0.0 at the pole, $\pi/2$ at the equator and π at the opposite pole, and longitude ϕ_{sp}, 0.0 at the line between the centers of the components increasing counterclockwise. The size of a spot is defined by its angular radius in radians, where a spot with a radius of π would cover the entire surface of the star. The temperature of the spot is characterized in `PHOEBE` by the temperature factor $t_f \equiv T_{spot}/T_{star}$, such that a $t_f > 1.0$ represents a hot spot and $t_f < 1.0$ a cool spot.

We can constrain the spot parameters with the small-amplitude periodic variation of the light curves. The amplitude of this variation along with its wavelength dependency provides information about the properties of the spot and the underlying effective temperature. Since rotational modulation of the light curves due to surface spots can be approximated as sinusoidal, a way to estimate the amplitude of this photometric variation is by fitting a sinusoid with the rotation period of the spotted component to the data. In fact, if we find that both components are rotating with different periods, we can fit two sinusoids simultaneously to obtain the amplitudes due to both rotations. The measured peak-to-peak amplitude in each band must be scaled by the components' relative luminosities, because the observed amplitude is diluted by the light from the other component. For example, spots that cause photometric variability of 10% in the light curve of a single star, in a system in which two components are contributing equal amounts to the system's luminosity, the same spots would cause a 5% variability in the system's light curve.

Once we have estimated the intrinsic variability of the component $\Delta m_o(\lambda)$, then we model the spotted star following an analytical inversion technique, like that by Bouvier et al. (1993). This model is based on blackbody radiation from two sources, and assumes that all the spots are at the same temperature. It does not assume anything about the number or shape of the spots, and instead models the areal coverage of the spots as a fraction of the star's surface, $\alpha = A_{spot}/A_{star}$. The wavelength-dependent variation in the light curves due to surface spots is thus described as:

$$\Delta m(\lambda) = -2.5\ \log[1 - (1 - Q(\lambda))\ \alpha/(1 - \mu(\lambda)/3)],$$

where $\mu(\lambda)$ are the corresponding limb-darkening coefficients for the observed bands (e.g., Claret, 2000); and $Q(\lambda)$ is the flux ratio of the spots and the star:

$$Q(\lambda) = \frac{B_\lambda(T_{spot})}{B_\lambda(T_{star})} = \frac{e^{\frac{hc}{\lambda k_B T_{star})}} - 1}{e^{\frac{hc}{\lambda k_B T_{spot}}} - 1},$$

where h is the Planck constant, c is the speed of light and k_B is the Boltzmann constant. The flux ratio $Q(\lambda)$ is integrated over each of the observed passbands using their transmission functions in order to best represent the variability in each band.

We fit the modeled $\Delta m(\lambda)$ to the observed variability in each of the observed bands by doing a Monte Carlo sampling of the spots' parameters α and t_f, about 1 000 times. In fact, we are able to determine a family of α and t_f for which the variability is equally well fitted to the observed $\Delta m_o(\lambda)$. This lack of uniqueness in the solution is because a spot will cause a similar variability than a larger but warmer spot, or several warmer spots, or a smaller and cooler spot. Once this family of spot parameters is determined, one must chose a given α and t_f that reproduces

the observed variability to use as input parameters for the spot modeling in PHOEBE.

Because of the degeneracy that spot modeling introduces into the eclipsing binary model, the determination of the spot parameters through this analytical inversion technique is a proxy for minimizing for the spot parameters in the solution. After obtaining values for α and t_f, the position of the spot on the surface can be determined by minimizing for θ_{sp} and ϕ_{sp} in PHOEBE, while keeping all other parameters constant. Afterwards, because the analytical inversion technique is an approximation, the radius of the spot which is derived from α can be also minimized after the position of the spot is defined and while keeping the other spot parameters and the system parameters fixed.

This analysis was implemented in the light curve modeling of 2M0535−05, as described in Section VI.3, to describe the small amplitude variability of the light curves in the different observed passbands.

IV.2.7 Joint Confidence Intervals

The global minimum of the solution is not a single point in the parameter space, but is instead a region. In fact, the data's noise and parameter degeneracy may make the global minimum more difficult to identify. The heuristic scans allow us to obtain statistically correct errors in the parameters, which are generally larger than the formal errors. In order to explore the parameter correlations and solution degeneracies more carefully, and to thus determine more robust parameter uncertainties, a thorough Monte Carlo sampling of parameter hyperspaces is performed using PHOEBE's

scripting capability. An example of script written to scan the parameter cross section between the ratio of temperatures and the ratio of radii or surface potentials is found in Appendix C.

The correlations between the parameters are particular to the system's characteristics and data set. The goal of exploring different parameter cross sections is to determine heuristic errors for parameters given the system parameters and evaluate the goodness of the fit to the observed curves. The latter can be evaluated by the reduced chi-square of the fit, which is given by:

$$\chi^2_{red} \;=\; \frac{\chi^2}{N-M-1} \;=\; \frac{1}{N-M-1}\sum_{j=0}^{N-1}\frac{(O_j-C_j)^2}{\sigma_j^2},$$

where N is the number of data points, M is the number of fitted parameters, $(O_i - C_i)$ are the residuals of the fit and σ_j is the uncertainty of the data points; an adequate fit is when $\chi^2 \approx N - M - 1$ (Press et al., 2007). The best solution will correspond to that for which the χ^2 of the fit is χ^2_{min}.

The exploration of the parameter cross sections is done via a Monte Carlo sampling that allows one to randomly select values of the parameters of interest. This part of the analysis is computationally very expensive and is done largely with the use of computer clusters. One parameter cross section typically requires several hundreds of hours of computer usage on one processor. The system parameters that are strongly correlated with the parameters of interest, like $\Delta\Phi$ when sampling e and ω or the passband luminosities when changing the effective temperatures, are then minimized or computed; while all other parameters are kept constant. We begin the sampling over a large range of parameter values. After a few hundred random iterations, we

Table 3: $\Delta\chi^2$ as a Function of Confidence Level and Number of Parameters of Interest ν

	ν					
	1	2	3	4	5	6
68.27%	1.00	2.30	3.53	4.72	5.89	7.04
90%	2.71	4.61	6.25	7.78	9.24	10.6
95.45%	4.00	6.18	8.02	9.72	11.3	12.8
99%	6.63	9.21	11.3	13.3	15.1	16.8
99.73%	9.00	11.8	14.2	16.3	18.2	20.1
99.99%	15.1	18.4	21.1	23.5	25.7	27.9

This table has been adopted from Press et al. (2007).

assess the shape and depth of the χ^2 around the global minimum and narrow the sampled parameter range to obtain more detailed contours around the minimum while limiting the computing usage. With every change in the system parameters, the χ^2 of the fit will also vary and one can calculate this variation with respect to the best solution as $\Delta\chi^2 = \chi^2 - \chi^2_{min}$. Thus $\Delta\chi^2$ in the joint parameter hyperspace of the sampled parameters will have a χ^2 distribution with ν degrees of freedom, where ν are the number of parameters of interest for which the confidence intervals are to be determined jointly (Press et al., 2007). The confidence levels of ν parameters for a given $\Delta\chi^2$ are found in Table 3; where a confidence level of 68.27% typically represents an uncertainty of 1 σ, a 95.45% level corresponds to 2 σ, 99.73% to 3 σ, and so on. The heuristic uncertainty of a sampled parameter is determined by the constant χ^2 contours in the parameter cross section; see for example Figure 28. The 1-σ uncertainty for one of the explored parameters is given by the projection of the

constant χ^2 1-σ contour onto that parameter's axis.

The detailed exploration of different parameter cross sections thus allows us to determine the heuristic errors of parameters that are strongly correlated, and also to ensure that the LC+RV solution has reached its global minimum.

IV.2.8 Determination of the Parameter Uncertainties

The formal errors of the fitted parameters are determined by the diagonal elements of the covariance matrix resulting from the minimization procedure. The off-diagonal elements represent the correlations between the parameters, and are useful to distinguish parameters that are not sensitive to a particular data set from those parameters that are highly correlated. For example, the mass ratio q is fully defined by the radial velocity curves and trying to extract it from a fit to only light curves is not possible. The minimization might converge, but because the light curves are not sensitive to q the resulting corrections are not physically significant. The modeling tools offer great flexibility, and in practice, we are allowed to minimize for any adjustable parameter given one or more observed curve. However, the user must undertake the analysis cautiously in order to avoid generating unphysical results.

When implementing the method of multiple subsets to reach the best solution, the covariance matrices resulting from the minimization of the distinct parameter subsets expressly do not include all the parameter correlations in order to aid convergence. Therefore, they are not suitable to derive formal uncertainties for the adjusted parameters (Wilson and Biermann, 1976). To correctly compute the covariance matrix

for the determination of their formal errors, all of the parameters should be minimized after the best solution has been attained. The result from this minimization will include the appropriate formal errors from the covariance matrix; however, the corrections to the parameters should not be adopted.

Once the global solution of the system has been attained, from the careful minimization of the system parameters and the heuristic scanning, we are ready to assess the uncertainties of the parameters of the RV+LC solution. There are certain parameters that have uncertainties that are not derived from the eclipsing binary modeling, i.e. $P_{\rm orb}$ and $P_{\rm rot,j}$, their determination has been explained in Section IV.1. These errors are propagated into those of the other system parameters by the sum of their errors in quadrature. The synchronicity parameters σ_{F_j} depend exclusively on $P_{\rm orb}$ and $P_{\rm rot,j}$ (see Equation 4) thus their uncertainties are given by:

$$\sigma_{F_j} = F_j \left[\left(\frac{\sigma_{P_{\rm orb}}}{P_{\rm orb}} \right)^2 + \left(\frac{\sigma_{P_{\rm rot,j}}}{P_{\rm rot,j}} \right)^2 \right]^{1/2} .$$

We continue with the determination of the parameter uncertainties that depend solely on the RV solution, namely q, $a \sin i$, v_γ and $M \sin^3 i$. For the RV solution, the inclination is set to 90° and the value of a is adjusted to maintain $a \sin i$ constant. We minimize for q, $a \sin i$ and v_γ, but also for e, ω and $\Delta\Phi$, in order to obtain the appropriate correlation matrix from the minimization, because the RV solution depends on all of these parameters. However, because e, ω and $\Delta\Phi$ also depend on the LC, it would not be correct to obtain their formal errors from this correlation matrix. The formal errors from the covariance matrix of the fit to only the RV curves are adopted for q, v_γ and $a \sin i$. The uncertainty in $M \sin^3 i$ (see Equation 1) is

obtained from the propagation of those errors according to:

$$\sigma_{M \sin^3 i} = M \sin^3 i \left[\left(\frac{3\ \sigma_{a \sin i}}{a \sin i} \right)^2 + \left(\frac{2\ \sigma_{P_{\rm orb}}}{P_{\rm orb}} \right)^2 \right]^{1/2} .$$

After setting i and a back to their best values, we then obtain the formal errors for i, Ω_1, Ω_2, e, ω and $\Delta\Phi$ from the covariance matrix of the RV+LC solution. This matrix is obtained from the minimization of all of the parameters that have been determined via the eclipsing binary modeling except for q, v_γ and $a \sin i$, which were determined in the previous step. The parameters that are assumed or obtained externally are not minimized.

In the cases where the uncertainty of a parameter has been determined from the parameter cross section scans described in the previous section, the heuristic errors are adopted instead of the formal uncertainties.

The uncertainty in a is then obtained from $a \sin i$, i and their errors, as follows:

$$\sigma_a = a \left[\left(\frac{\sigma_{a \sin i}}{a \sin i} \right)^2 + \left(\frac{\sigma_i}{\tan i} \right)^2 \right]^{1/2} .$$

The individual masses are obtained from Kepler's third law (Equation 1) and the mass ratio q (Equation 3), and their uncertainties are:

$$\sigma_{M_1} = M_1 \left[\left(\frac{3\ \sigma_a}{a} \right)^2 + \left(\frac{2\ \sigma_{P_{\rm orb}}}{P_{\rm orb}} \right)^2 + \left(\frac{\sigma_q}{q+1} \right)^2 \right]^{1/2} ,$$

$$\sigma_{M_2} = M_2 \left[\left(\frac{3\ \sigma_a}{a} \right)^2 + \left(\frac{2\ \sigma_{P_{\rm orb}}}{P_{\rm orb}} \right)^2 + \left(\frac{\sigma_a}{q\ (q+1)} \right)^2 \right]^{1/2} .$$

The components' radii depend on Ω_j, q, a, e and F_j, by the inverse of Equation 2. Since the components are not perfectly spherical, the radius of a component varies at

different points on its surface. We obtain the uncertainty for the radius that points toward the center of the other component, known as point radius, for which $\lambda = 1$, $\nu = 0$. The uncertainty in the fractional radius σ_{r_j}, where $r_j = R_j/a$, will be largest when the components are closest to each other, i.e. at periastron, thus $d = 1 - e$. The error in the fractional point radius is given by:

$$\sigma_{r_j} = \left[\left(\frac{\sigma_{\Omega_j}}{A_1} \right)^2 + \left(\frac{A_2 \ \sigma_q}{A_1} \right)^2 + \left(\frac{A_3 \ \sigma_e}{A_1} \right)^2 + \left(\frac{A_4 \ \sigma_{F_j}}{A_1} \right)^2 \right]^{1/2},$$

where:

$$A_1 = -\frac{1}{r_j^2} - \frac{q \ (r_j + e - 1)}{[r_j^2 + (1-e)^2 - 2 \ r_j \ (1-e)]^{3/2}} - \frac{q}{(1-e)^2} + F_j^2 \ r_j \ (1+q),$$

$$A_2 = \frac{1}{[r_j^2 + (1-e)^2 - 2 \ r_j \ (1-e)]^{1/2}} - \frac{r_j}{(1-e)^2} + \frac{1}{2} \ F_j^2 r_j^2,$$

$$A_3 = -\frac{q \ (r_j + e - 1)}{[r_j^2 + (1-e)^2 - 2 \ r_j \ (1-e)]^{3/2}} - \frac{2 \ q \ r_j}{(1-e)^3},$$

$$A_4 = F_j \ (1+q) \ r_j^2.$$

The uncertainty in the radii are then given by:

$$\sigma_{R_j} = R_j \ \left[\left(\frac{\sigma_a}{a} \right)^2 + \left(\frac{\sigma_{r_j}}{r_j} \right)^2 \right]^{1/2}.$$

We can also obtain the semi-amplitudes K_1 and K_2 and their uncertainties:

$$K_1 = \frac{2 \ \pi \ q \ a \sin i}{P_{\rm orb} \ (1+q)(1+e^2)^{1/2}}, \quad K_2 = \frac{K_1}{q}; \tag{5}$$

$$\sigma_{K_1} = K_1 \ \left[\left(\frac{\sigma_{a \sin i}}{a \sin i} \right)^2 + \left(\frac{\sigma_{P_{\rm orb}}}{P_{\rm orb}} \right)^2 + \left(\frac{\sigma_q}{q \ (1+q)} \right)^2 + \left(\frac{e \ \sigma_e}{1-e^2} \right)^2 \right]^{1/2},$$

$$\sigma_{K_2} = K_2 \ \left[\left(\frac{\sigma_{K_1}}{K_1} \right)^2 + \left(\frac{\sigma_q}{q} \right)^2 \right]^{1/2}.$$

Additionally, we calculate the surface gravities, $g_j = G\ M_j/R_j^2$, assuming that the stars are spherical. Surface gravities are typically reported in terms of their logarithm, $\log g_j$. The errors in $\log g_j$ therefore depend on the mass and radius of each component, according to the following:

$$\sigma_{\log g_j} = \frac{1}{\ln(10)} \left[\left(\frac{\sigma_{M_j}}{M_j} \right)^2 + \left(\frac{2\ \sigma_{R_j}}{R_j} \right)^2 \right]^{1/2}.$$

An example of a `PHOEBE` script that was used for the calculation of the parameter uncertainties of Par 1802's system parameters can be found in Appendix D.

CHAPTER V

PARENAGO 1802

This chapter exemplifies the use of the analyses and techniques described in the previous chapters to model the eclipsing binary system, Parenago 1802, and consists of the manuscript, Gómez Maqueo Chew et al. (2010), that is to be submitted for publication.

The discovery of Parenago 1802 was presented, along with its radial velocity, study which found the system to be an eclipsing binary with a period of ~ 4.67 days where both components have near equal masses, $M_1 = 0.40 \pm 0.03$ and $M_2 = 0.39 \pm 0.03$ $M_\odot$ (Cargile et al., 2008, hereafter CSM07). Par 1802, as a member of the Orion Nebula Cluster (ONC; Hillenbrand, 1997), is considered to have an age of ~ 1 Myr (CSM07). A follow-up analysis which included the radial velocity curves and the I_C-band light curve found the components' masses to be equal to within $\sim 2\%$, but their radii and effective temperatures to differ by ~ 5–10% (Stassun et al., 2008, hereafter SMC08). These disparate radii and temperatures are suggested to be the result of a difference in age of a few hundred thousand years. The common assumption that binary components have the same age is tested by this equal-mass system by giving a measure of how strictly coevality should be considered, to within $\sim 300\,000$ years. At very young ages, like that of Parenago 1802, the true difference in the formation epoch of the stars has a more significant imprint on the system and its components

(Kraus and Hillenbrand, 2009); it is after $\sim$ 10 Myrs that this signature becomes insignificant (Stempels et al., 2008).

We present the VI_CJHK_S light curves for Par 1802 (§V.1.1); as well as, newly acquired, high-resolution, spectroscopic data (§V.1.3). The multi-band nature of our analysis allows us to probe the radiative properties of the system. An in-depth periodicity analysis of the light curves enables us to refine the orbital period for the binary and to identify the rotation period of its components (§V.2.1). We are able to measure a veiling contribution in the spectra (§V.2.2), which allows for the characterization of the third light of the system (§V.2.3) required for the multi-epoch, multi-band, light curve modeling presented in §V.3. As a result, we obtain the physical properties of the binary and its components along with formal and heuristic uncertainties. We also find evidence of a rapidly rotating stellar component in the light curves, which in conjunction with the observed blue excess in the light curves and the veiling found in the spectra, lead us to propose that Par 1802 has a third stellar component (§V.4.2).

V.1 Observations and Data Reduction

V.1.1 Photometric Observations

We present the light curves of Par 1802 in V (with a total of 2286 data points), I_C (3488), J (564), H (176) and K_S (365). The detailed observing campaign is described in Table 4, while Appendix E contains Tables 11–15 that provide a sample of the individual measurements in the observed VI_CJHK_S passbands. The full data

set will be found in the online version of the paper by Gómez Maqueo Chew et al. (2010). The I_C data cover the largest time span, from December 1994 to January 2009; it includes the previously published light curve (SMC08) and 1279 new data points obtained between March 2007 and January 2009. The V light curve includes data obtained between January 2001 and January 2009 with the 0.9-m telescope at KPNO and with the SMARTS 0.9-m, 1.0-m and 1.3-m telescopes at CTIO. Using the ANDICAM instrument, which allows for simultaneous optical and near-infrared imaging, Par 1802 was observed photometrically with the SMARTS 1.3-m telescope at CTIO between February 2005 and February 2008, constituting the entirety of the JHK_S light curves. Figure 15 shows the VI_CJHK_S light curves, including those published in SMC08; the data have been folded over the orbital period and each band has been shifted in magnitude for easier visualization. Each point is an individual observation and the solid line represents the model of our best solution as described in §V.3. We also observed Par 1802 in the B-band; however, the resulting light curve was not well-sampled and it is very noisy due to the photometric variability of the third component, as discussed in later sections. Thus, we do not include the B light curve in the rest of our analysis, except as a consistency check of our final solution.

V.1.2 Near-Infrared Data Reduction

The mean near-infrared magnitudes of Par 1802 are $J = 11.124 \pm 0.024$, $H = 10.267 \pm 0.032$ and $K = 9.938 \pm 0.018$ (Skrutskie et al., 2006). The observations in the near-infrared were made in sets of five dither positions in J, and seven dither

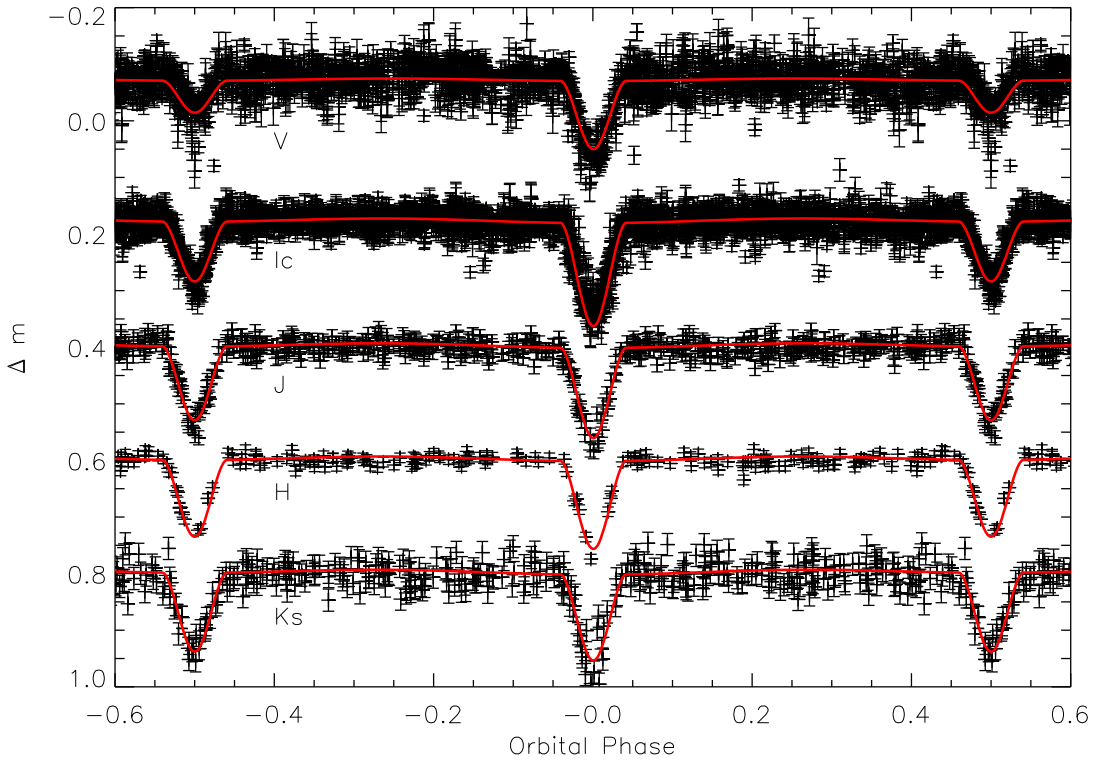

Figure 15: Observed and Modeled VI_CJHK_S Light Curves of Par 1802. We show the observed photometric light curves with their corresponding uncertainties as described in §V.1.2. The data has been shifted in magnitude for easier visualization and folded over the binary's orbital period. The solid line represents the best RV+LC solution for Par 1802 (see §V.3 for a detailed description of the modeling procedure, and see Table 7 for the physical parameters of the system).

Table 4: Photometric Time Series Observations of Par 1802

Telescope	HJD Range[a]	Filter	N_{obs}[b]
KPNO 0.9-m	49698.35–49714.50	I_C	110
KPNO 0.9-m	50820.62–50829.78	I_C	21
CTIO 0.9-m	51929.59–51936.78	I_C	164
		V	153
KPNO 0.9-m	52227.75–52238.00	I_C	131
KPNO 0.9-m	52595.75–52624.95	I_C	279
		V	146
CTIO 0.9-m	52622.57–52631.51	I_C	80
		V	83
SMARTS 0.9-m	53011.57–53024.77	I_C	200
		V	104
SMARTS 1.3-m	53403.53–53463.53	I_C	246
		V	176
		J	90
		K_S	88
SMARTS 1.3-m	53646.86–53728.69	I_C	188
		V	113
		J	57
		K_S	52
SMARTS 1.0-m	53719.56–53727.83	I_C	117
		V	101
SMARTS 1.3-m	53745.63–53846.51	I_C	276
		V	182
		J	80
		K_S	73
SMARTS 1.3-m	53980.89–54100.65	I_C	254
		V	190
		J	99
		K_S	98
SMARTS 1.0-m	54103.58–54112.773	I_C	105
		V	103
SMARTS 1.3-m	54103.73–54191.53	I_C	183
		V	61
		J	63
		K_S	54

Continued on Next Page . . .

Table 4 – Continued

Telescope	HJD Range[a]	Filter	N_{obs}[b]
SMARTS 1.3-m	54375.81–54465.82	I_C	371
		V	250
		J	128
		H	129
SMARTS 1.3-m	54467.62–54497.69	I_C	142
		V	96
		J	47
		H	47
SMARTS 1.0-m	54482.58–54494.74	I_C	218
		V	169
		B	183
SMARTS 1.0-m	54835.56–54853.78	I_C	403
		V	359

[a] Range of Heliocentric Julian Dates (2 400 000+).
[b] Number of observations.

positions in HK_S, with total integration times of 150 and 175 s, respectively.

The near-infrared data are reduced by taking into account the position of the ANDICAM's mirror which is essential in removing the interference pattern of sky emission lines characteristic to each of the mirror positions, as well as of other infrared contributions. Dome flats are provided individually for each of the possible seven dither positions. Each of these dome flats is created by subtracting from the median combination of ~ 10 images taken with the lights off a median combination of ~ 10 images taken with the dome lights on in order to reduce the infrared contribution in the final images of sources such as the telescope, the optical components and the sky. The individual dome flats for each of the mirror's dithers allow for the creation of separate flats for each mirror position. Sky flats are created from the median

combination of ~ 10 images with slightly different star fields for each distinct dither position, so that the stars present in the field average out and provide a flat image. This is possible since the observed field is not a very crowded one. For each observing season, new sky flats are created in order to correct for any changes in the dithering and for any physical changes in the instrument. The procedure to then reduce the data consists of the following steps: the dark is first subtracted from the raw image, followed by the subtraction of the corresponding normalized sky image, which depends on the mirror position at which the images were taken. The image is then divided by the corresponding normalized dome flat. Once this is done, the dithered images are shifted and cropped in order to be combined by doing a pixel-by-pixel average in order to obtain the final image.

Differential aperture photometry is done using the `IRAF` package `APPHOT`. The comparison star, Parenago 1810, was chosen for its frequency in the final reduced images of Par 1802 and because it shows very little variability in the I_C and V bands; furthermore, it is not found to be variable in the near-infrared variability study of the ONC by Carpenter et al. (2001). The uncertainty in the produced JHK_S light curves is dominated by the systematic uncertainties of the aperture photometry. The JH bands have a similar scatter in magnitude, $\sigma_J = \sigma_H = 0.01$; however, the interference pattern of the sky emission lines in the K_S light curve is more significant, making the scatter in this band larger, $\sigma_{K_S} = 0.02$. These uncertainties are estimated by calculating the standard deviation of the rectified light curves, excluding the data during the eclipses. The periodic low-amplitude variability, identified in the light

curves and described in detail in §V.2.1, is removed from each of the light curves in order to determine the photometric precision.

V.1.3 Spectroscopic Observations

We observed Par 1802 on the night of UT 2007 Oct 23 with the High Resolution Echelle Spectrometer (HIRES) on Keck-I[1]. We observed in the spectrograph's "red" (HIRESr) configuration with an echelle angle of -0.403 and a cross-disperser angle of 1.703. We used the OG530 order-blocking filter and $1\farcs15\times7\farcs0$ slit, and binned the chip during readout by 2 pixels in the dispersion direction. The resulting resolving power is $R \approx 34\,000$ per 3.7-pixel (~ 8.8 km s^{-1}) FWHM resolution element. For the analyses discussed below, we used the 21 spectral orders from the "blue" and "green" CCD chips, covering the wavelength range $\lambda\lambda$5782–8757.

We obtained one integration of Par 1802 of 900 s. Th-Ar arc lamp calibration exposures were obtained before and after the Par 1802 exposure, and sequences of bias and flat-field exposures were obtained at the end of the night. The Par 1802 exposure was processed along with these calibrations using standard `IRAF` tasks and the MAKEE reduction package written for HIRES by T. Barlow. The latter includes optimal extraction of the orders as well as subtraction of the adjacent sky background. The signal-to-noise (S/N) of the final spectrum is ≈ 70 per resolution element.

In addition, we also observed the late-type spectral standards (see Kirkpatrick et al., 1991), Gl 205 (M1.5) and Gl 251 (M3), at high signal-to-noise. These were

[1]Time allocation through NOAO via the NSF's Telescope System Instrumentation Program (TSIP).

observed immediately before the Par 1802 exposure and used exactly the same instrumental configuration. We use these spectral standards in our spectral decomposition analysis of the Par 1802 spectrum (see V.2.2).

V.2 Analysis

V.2.1 Periodicity

We measure the timings of the eclipses in the I_C light curve, which covers the longest time span, and are able to refine the orbital period for Par 1802 by fitting a linear ephemeris to the observed eclipse times. We find that an orbital period of $P_{\rm orb} = 4.673903 \pm 0.000060$ days fits our radial velocity and light curves. The eclipse timings are measured by fitting a Gaussian using a least squares approach to those eclipses for which there are at least five data points and that include the minimum of each eclipse. Table 5 summarizes the measurements of the timings of the eclipses and their uncertainties.

The VI_CJHK_S light curves corresponding to the out-of-eclipse (OFE) phases, i.e., all phases excluding those during the eclipses, are searched for periods between 0.1 and 20 d using the Lomb-Scargle periodogram technique (Scargle, 1982), well suited for unevenly sampled data. The resulting periodograms (Fig. 16) show the power spectra in frequency units of days^{-1} and present multiple strong peaks. These peaks represent a combination of one or more true independent frequencies and their aliases.

The amplitudes of the periodograms are normalized according to the formula-

Table 5: Timings of Eclipse Minima in the I_C Light Curve

HJD[a]	O-C (Phase)	Eclipse Type
49701.567326 ± 0.000006	-0.014307	Secondary
49703.956710 ± 0.000005	-0.003621	Primary
49713.296386 ± 0.000001	-0.005335	Primary
51935.7554 ± 0.0001	0.0052	Secondary
52227.86081 ± 0.00004	0.00256	Primary
52234.84326 ± 0.00001	-0.00296	Secondary
52601.77110 ± 0.00008	0.00317	Primary
52622.76956 ± 0.00002	-0.00353	Secondary
52629.82635 ± 0.00002	0.00577	Primary
53017.71700 ± 0.00005	-0.00242	Primary
53024.74611 ± 0.00001	0.00204	Secondary
53459.48344 ± 0.00006	0.01700	Secondary
54106.74615 ± 0.00001	0.00265	Primary
54487.65947 ± 0.00007	0.00215	Secondary
54494.6722 ± 0.0005	0.0020	Primary
54847.563143 ± 0.000004	0.005949	Secondary

[a] Heliocentric Julian Date (2 400 000+)

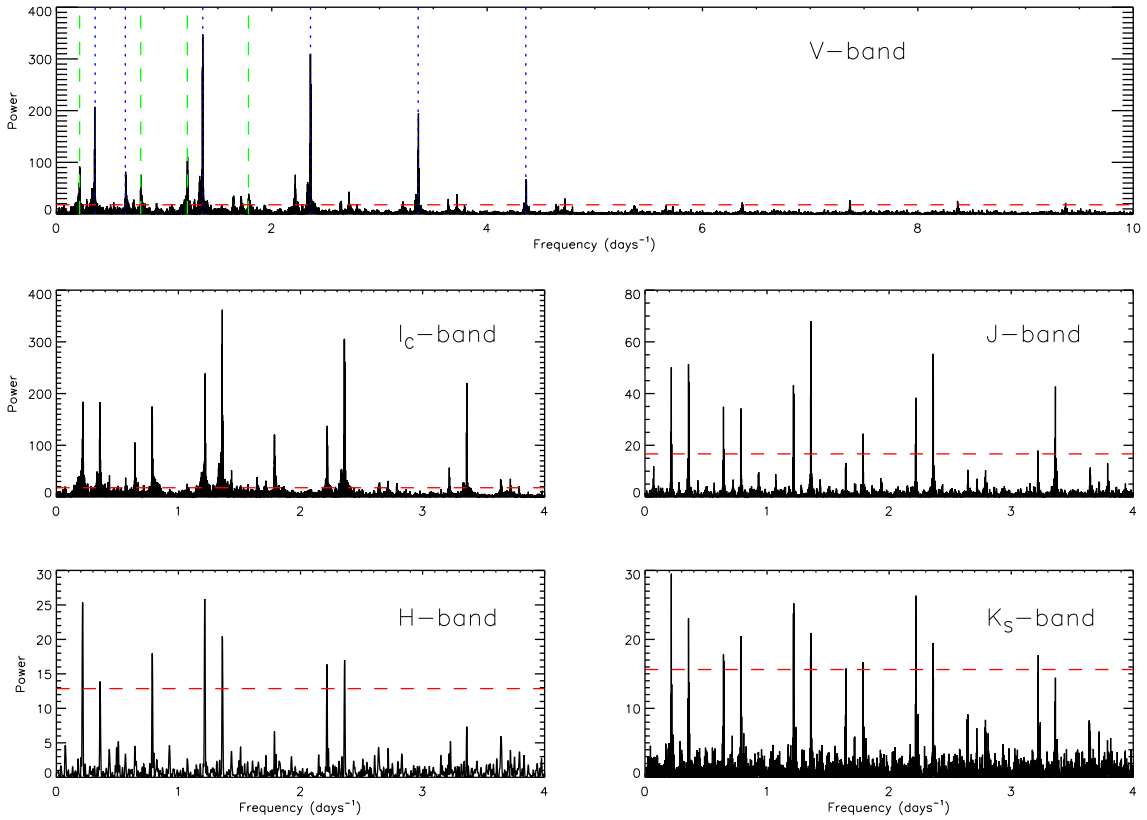

Figure 16: OFE VI_CJHK_S Lomb-Scargle Periodograms. The out-of-eclipse (OFE) light curves were searched for periodicities, as described in §V.2.1, identifying two independent periodic signals with frequencies of ~ 0.216 and ~ 1.36 days^{-1}, corresponding to periods of $P_1 = 4.629 \pm 0.006$ and $P_2 = 0.7355 \pm 0.0002$ d, respectively. Table 6 lists the identified periods in each observed passband with their corresponding uncertainties. The vertical, dashed lines on the top panel mark the frequency corresponding to P_1 and its aliases and beats; while the vertical, dotted lines correspond to the frequency of P_2 and its aliases and beats. The significance of the peaks is given by the horizontal, dashed line which denotes the 1% False-Alarm Probability (FAP); since most of the significant peaks are found between 0 and 4 days^{-1}, only the V-band periodogram is shown in its entirety. The out-of-eclipse VI_CJHK_S light curves folded over the two identified periods are presented in Fig. 17.

Table 6: Periodicity in the Light Curves of Par 1802

	OFE[a]		O-C[b]	
	P_1	P_2	P_1	P_2
V	4.626 ± 0.001	0.73557 ± 0.00002	4.6257 ± 0.0009	0.73558 ± 0.00001
I_C	4.6257 ± 0.0005	0.73560 ± 0.00001	4.6259 ± 0.0004	0.735606 ± 0.000009
J	4.628 ± 0.003	0.73551 ± 0.00007	4.627 ± 0.002	0.73551 ± 0.00005
H	4.64 ± 0.03	0.7353 ± 0.0008	4.64 ± 0.03	0.7353 ± 0.0007
K_S	4.629 ± 0.003	0.7355 ± 0.0001	4.627 ± 0.004	0.7355 ± 0.0001

[a] Only the phases of the light curves that are out-of-eclipse, i.e. excluding the eclipses, were searched for periodicities.

[b] We did the periodicity analysis on the residuals of the modeling of the light curves; any periodicity due to the eclipsing binary nature of the system would be removed from the O-C Periodograms.

tion of Horne and Baliunas (1986) by the total variance of the data, yielding the appropriate statistical behavior which allows for the calculation of the false-alarm probability (FAP). The FAP indicates the statistical significance of the periodogram by describing the probability that a peak of such height would occur from pure noise. To calculate the FAP for each of the OFE light curves, a Monte Carlo bootstrapping method (e.g., Stassun et al., 1999) is applied; it does 1000 random combinations of the differential magnitudes, keeping the Julian Dates fixed in order to preserve the statistical characteristics of the data. The resulting 1% FAP level is indicated in the periodograms by the horizontal dashed line in Fig. 16. All periodogram peaks higher than the 1% FAP are considered to be due to real periodicity in our data; this includes the aliases and beats of any periodic signals.

To distinguish the periodogram peaks of the independent periods from their

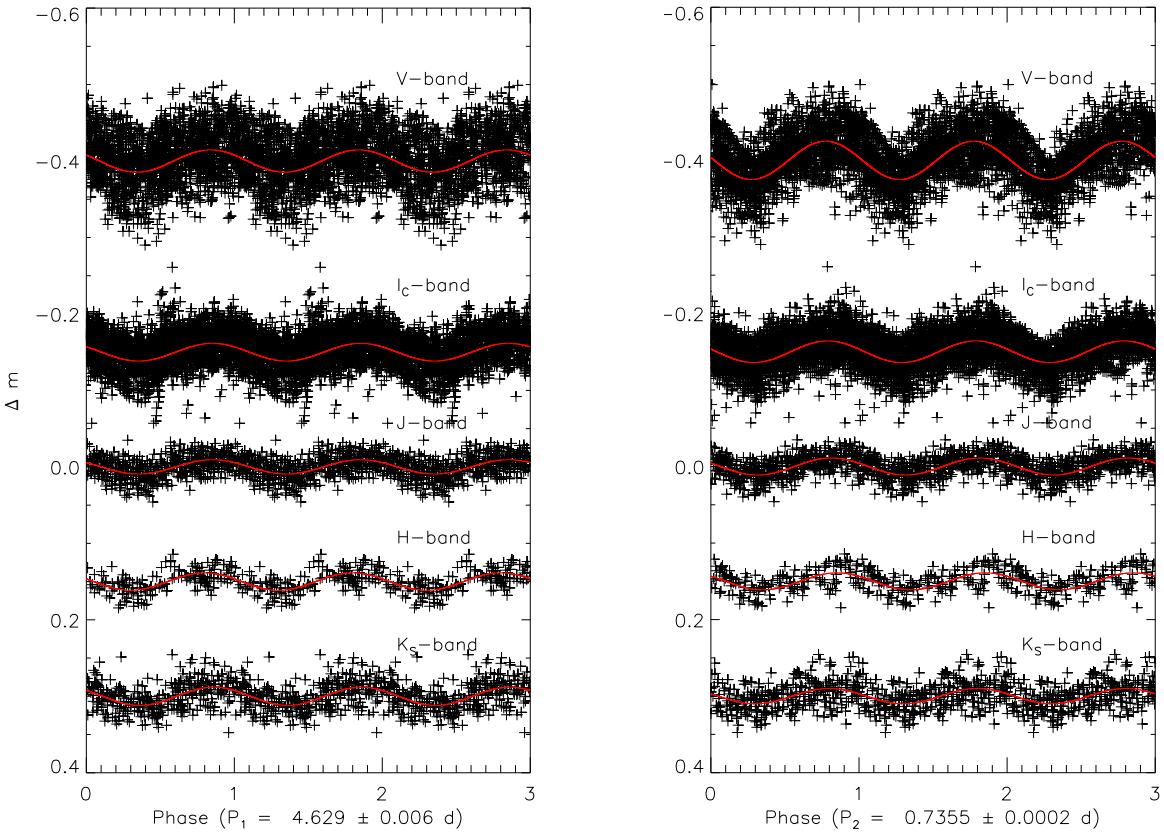

Figure 17: Low-Amplitude, Photometric Variability. The sinusoidal shape shown by the OFE light curves, folded over either of the two independent periods found in all observed passbands from the periodicity analysis (see Fig. 16 and Table 6), is characteristic of spot-induced, rotational modulation. The left-hand panel shows the VI_CJHK_S light curves folded over P_1 and displaced from zero for easier visualization. Superimposed is a sinusoid of period P_1 fitted to the data. In a similar way, the right-hand panel shows the same photometric OFE data folded over the shorter period, P_2, and its corresponding sinusoidal fit. The actual data points are repeated over each of the three phases shown. P_1 is attributed to the rotation period of the eclipsing components, and is consistent with the measured $v \sin i$ and radii of Par 1802; whereas P_2 is attributed to the stellar source of third light (see §V.4.2 for discussion on the third body).

aliases, a sinusoid is fitted to each light curve and subtracted from the data in order to remove the periodicity corresponding to the strongest peaks in the periodograms. This filtering procedure allows us to identify in the OFE periodograms of all observed passbands two independent periods, $P_1 = 4.629 \pm 0.006$ days and $P_2 = 0.7355 \pm 0.0002$ days. These two periods are given by the mean of the individual period measurements in each band and their uncertainties are given by the standard deviation of the mean (see Table 6). When the OFE light curves are phased to either P_1 or P_2, they are characterized by having a sinusoidal low-amplitude variability which is indicative of stellar rotational modulation (e.g., Stassun et al., 1999). Figure 17 shows on the left-hand side the OFE VI_CJHK_S light curves phased to P_1, and on the right-hand, the same data is phased to P_2. The periodograms of the OFE light curves after removing both sinusoidal signals are found to have peaks which are mostly below the 1% FAP line, ensuring that the periodic signals are well fitted by sinusoids and that any deviation from true sinusoids is hidden within the scatter of the data.

When we assess in detail the significant peaks in the periodograms of the OFE light curves, we find multiple-peaked structures due to the finite sampling of the data. In Fig. 16, the vertical dashed lines indicate P_1 and its aliases, and the aliases of P_2 are marked by the dotted lines. The peaks due to P_1 and its aliases attributed to the one-day sampling of the light curves and the peaks due to P_2 and its aliases correspond to the following frequencies (in days^{-1}):

$$
\begin{aligned}
1/P_1 &= 0.216 & \text{-1} + 1/P_2 &= 0.359 \\
1 - 1/P_1 &= 0.784 & \text{2 - } 1/P_2 &= 0.641 \\
1 + 1/P_1 &= 1.216 & 1/P_2 &= 1.359 \\
2 - 1/P_1 &= 1.784 & 1 + 1/P_2 &= 2.359, \\
2 + 1/P_1 &= 2.216 & \text{and so on.} & \\
3 - 1/P_1 &= 2.784 & & \\
3 + 1/P_1 &= 3.216 & &
\end{aligned}
$$

We also find at each significant period that there is a three-peaked structure, which is confirmed to arise from the sampling of the data. The separation between the higher central peak and the other two corresponds to the beat frequency of a $\sim$ 360 day period, which can be expected given the yearly recurrence of the data acquisition. To ensure that the peak that corresponds to P_1 is significantly different than that of the orbital period given the available dataset, we create two synthetic sinusoidal signals that are sampled using the timestamps of the OFE I_C light curve: one with a period equal to P_1 and another to $P_{\rm orb}$. After running the synthetic signals through the periodicity analysis described in §V.2.1, we compare their periodograms to that of the OFE I_C light curve. Figure 18 shows that the periodogram of the OFE I_C light curve (solid line) around the frequency of $1/P_1 \simeq 0.216$ days^{-1} is almost equal to the normalized periodogram of the synthetic signal with the same period (see dashed-dotted line in Fig. 18), as is expected. Moreover, the periodogram of the synthetic signal with a period equal to the orbital period (see dashed line in Fig. 18) is clearly distinct from the other two periodograms. For example in Fig. 18, the periodogram of the data (solid line) has its most significant peak at a frequency of $\sim$ 0.216 days^{-1}. The three-peaked structure is composed of this peak and the

peaks at ~ 0.2135, and ~ 0.2189 days^{-1}. By directly assessing the *window function* of the data through the periodograms of the synthetic periodic signals, we are able to discard the possibility that the three-peaked structure found in the periodograms centered around the most prominent peaks is an artifact of our periodicity analysis. The periodograms of the synthetic signals, as shown in Fig. 18, also present the three-peaked structure confirming that it arises from the sampling of the data and that we have enough frequency resolution to discern P_1 from $P_{\rm orb}$.

P_1 is close to the orbital period of the binary ($P_{\rm orb} = 4.673903 \pm 0.000060$ d), but is significantly different at a 7-σ level. In order to better understand P_1, we search for periodicities in the residuals (O-C) of the eclipsing binary modeling such that any period due to the eclipsing binary nature of the system would be removed from the periodograms. We are able to again identify both P_1 and P_2 in the O-C periodograms of all observed passbands. Table 6 describes in detail both identified periods in each observed light curve with their uncertainty, determined via a post-mortem analysis (Schwarzenberg-Czerny, 1991), for all of the OFE and O-C periodograms. We are able to verify that we have sufficient frequency resolution to distinguish P_1 from $P_{\rm orb}$ (see Fig. 18). Thus, we conclude that P_1 is not due to orbital effects, and in particular, P_1 significantly differs from $P_{\rm orb}$. If the photometric, low-amplitude variability is caused by surface spots rotating in and out of view on one or both of the binary components, the difference between P_1 and $P_{\rm orb}$ suggests that the rotation of the stars is not synchronized to the orbital motion.

The 4.629 d period (P_1) is consistent with the measured $v \sin i$ and radii of the

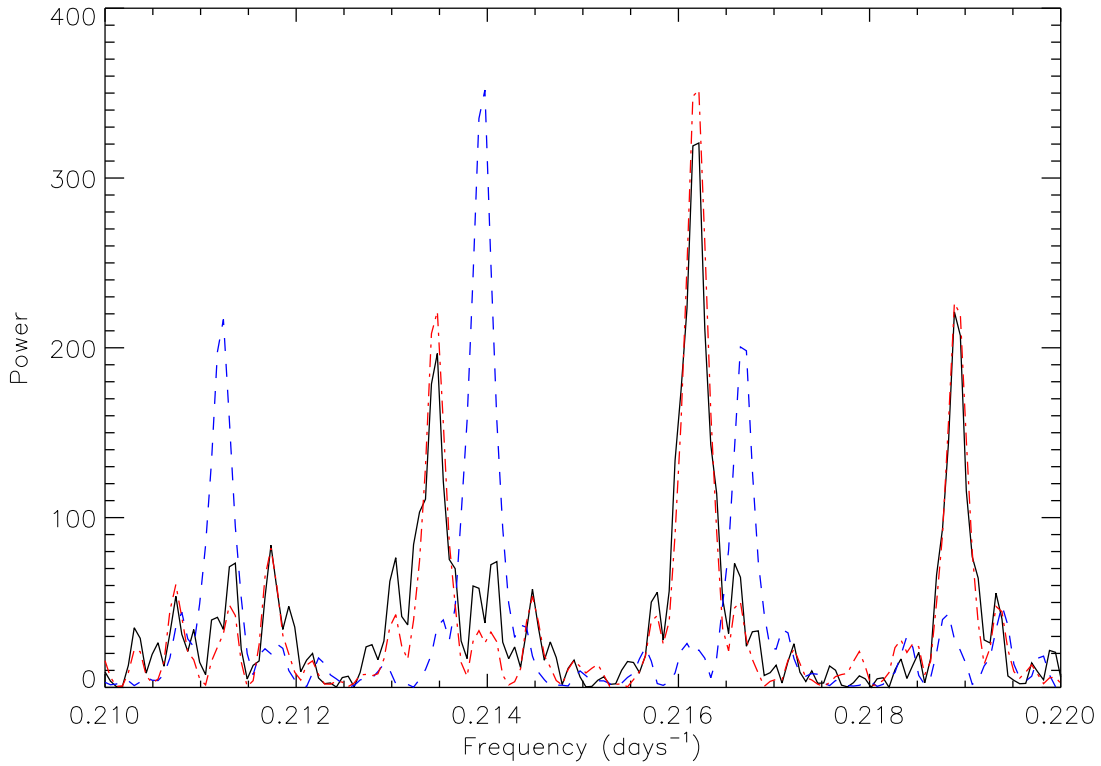

Figure 18: OFE I_C and Synthetic Periodograms. We compare the periodogram of the OFE I_C light curve (solid line) around the frequency of $1/P_1 \simeq 0.216$ days^{-1} with two synthetic sinusoidal signals, one with a period equal to P_1 (dashed-dotted line) and another with a period of $P_{\rm orb}$ (dashed line). Both synthetic signals have been sampled to the timestamps of the I_C data to preserve its statistical characteristics; and their periodograms have been scaled to the amplitude of the OFE I_C periodogram. The three-peaked structure around the most significant peak is due to the yearly sampling of the light curve; the side-peaks are separated from the central peak by a frequency of 1/360 days^{-1}. Since we are able to clearly distinguish between the periodogram peaks of the P_1 signal and those of the $P_{\rm orb}$ signal, we conclude the P_1 is significantly distinct from the orbital period.

eclipsing binary components, and we adopt it as the rotational period $P_{\rm rot}$ of both components. In §V.4.1, we will discuss how this rotation period provides information about the age of the system as described by tidal evolution theory. The short period (P_2) is considered be too fast to be due to rotation of either of the binary components, and based on the width of the spectral features, there is no evidence of such a rapid rotation in their spectra. Therefore, we propose in this paper that Par 1802 has in fact a third stellar component, which is rotating at the 0.7355 d period (P_2). There is additional observational evidence of the existence of this third body which will be addressed in the later sections.

V.2.2 Spectral Veiling: Evidence for a Third Light in Par 1802

In SMC08, the method of tomographic decomposition was applied on the HRS/HET dataset to recover the spectra of the individual components. It was found that the reconstructed spectra are compatible with an M1V spectral type for the primary, and an M3V type for the secondary. In addition, a detailed analysis of the relative line depths of the components made it possible to recover the luminosity ratio of the two components, which is found to be $L_{\rm prim}/L_{\rm sec} = 1.75$. This luminosity ratio is also consistent with the measured surface temperature ratio and stellar radii recovered from the eclipsing binary modeling of the system.

However, during our analysis of the HRS/HET spectra, we also found that the combined spectra cannot be represented by a simple linear combination of M1V and M3V template spectra. The line depths of the photospheric absorption lines are too

shallow, and an additional featureless component needs to be included in the binary model to reproduce the observations. The presence of such a featureless continuum component is often seen in PMS stars, and is normally referred to as *veiling*. A detailed description of veiling in T Tauri stars and how it can be measured is presented by Stempels and Piskunov (2003).

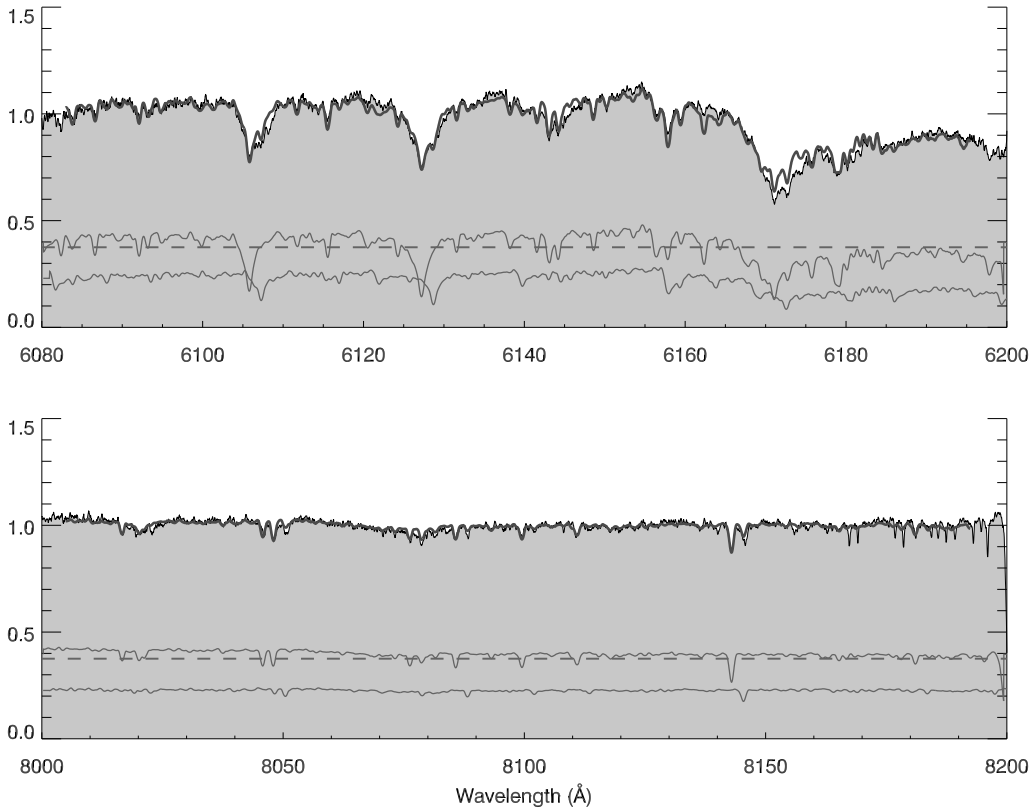

Figure 19: Observed and Model Spectrum of Par 1802. This figure illustrates how the observed spectrum of Par 1802 (black solid line) can be reproduced by a simple three-component model (thick gray line). This model consists of: an M1.5V template for the primary (upper spectrum), an M3V template for the secondary (lower spectrum), as well as a featureless veiling spectrum (dashed line). The components are scaled such that the continuum ratio of the components corresponds to 0.39:0.22:0.39. The gray area represents the area under the observed spectrum of Par 1802. See §V.2.2 for a more complete description.

In order to quantify the contribution of this third component to the total luminosity of the system, we performed a detailed analysis of the contribution from any source other than the M1 and M3 stars. Here, we did not use the HRS/HET spectra, since these were obtained with a fiber-fed spectrograph that does not allow for the direct subtraction of the strong nebular background surrounding Par 1802. Instead, we performed our analysis on the high-resolution Keck/HIRES spectrum, presented in §V.1.3, which was obtained through a long slit and allows for proper background subtraction, including the instrumental scattered light.

Even after subtraction of the nebular background, we find that there is still a contribution from an unidentified third source present in the spectrum. We extended the methods used by Stempels and Piskunov (2003) to a double-lined binary system by first constructing an unveiled model spectrum for Par 1802. This unveiled model spectrum is a combination of two observed template spectra, GL 205 (M1.5V) and GL 251 (M3V), with a luminosity ratio of 1.75:1.0, as mentioned above. We then applied a χ^2-minimization on each individual spectral order to solve for the required contribution of a third component. We find that there is a featureless continuum present in the spectrum of Par 1802, with a luminosity that is approximately equal to that of the primary component. The *normalized* luminosity ratio of all three components is then (primary:secondary:veiling) 0.39:0.22:0.39, in the I_C-band. In terms of the veiling factor, which is defined as the ratio of the contribution of the veiling continuum and the contribution of the stellar continuum, this is equivalent to a veiling value of approximately 0.6. We illustrate our result in Fig. 19, where

we show how the observed spectrum can be reproduced by adding the two eclipsing stellar components and a third featureless component. The double-lined nature of the system is obvious around the narrow absorption lines observed in the redder order.

The analysis above does not assume anything about the nature of the third light source. We only state that an extra featureless component is needed in both the HRS/HET spectra and the Keck/HIRES spectrum, and that this is not an artifact of the reduction process. Given that there is no clear infrared excess in the spectral energy distribution of the system as would be characteristic of disks (see SMC08), and that the Hα emission of a few milliangstroms (CSM07) seen in the eclipsing stellar components is too weak to arise from accretion, we conclude that the veiling must be related to a source other than the eclipsing binary components.

V.2.3 Characterization of the Third Light

We constrain the level of third light in each passband (L_3) from the veiling measurements described above, and from the amount of third light needed to simultaneously fit all of the observed light curves. The details of the eclipsing binary modeling and of the exploration of the parameter correlations are described below in §V.3, as are the uncertainties of the system's fundamental parameters introduced by the uncertainty in the level of third light.

The upper limit of the third light level allowed by the observed light curves is obtained by setting the inclination (i) of the system to 90°, and fitting for L_3. This is the upper limit because at an inclination angle of $i = 90°$ the eclipses are intrinsically

deepest, thus the observed shallow eclipses require the maximum dilution. We find that the maximum level of third light allowed is one that contributes $\sim 75\%$ to the total luminosity of the system in the I_C-band. To further explore the relationship between L_3 and i, we fit the third light levels in each passband individually for inclination angles between 75 and 90°. We find two trends from this analysis. The first one is that, for any given inclination angle, the required level of third light is approximately constant for the $I_C JHK_S$ light curves. The second trend is that Par 1802 has a *blue excess*, i.e., the B and the V-bands require approximately 20% more third light of the total system's luminosity to fit the eclipse depths than in the other passbands.

Without additional information on the contribution of third light, it would not be possible to ascertain what the *real* values of the inclination and third light levels are. Using the spectral veiling measurements described in the section above, we are able to constrain the level of third light found in the light curves. The veiling measurements vary from one order to the next; thus to obtain the third light contribution in the I_C-band (L_{3,I_C}), we averaged the veiling factors in this wavelength range, obtaining and average veiling of 0.6 ± 0.1. The corresponding third light given this veiling measurement is one that contributes $\sim 40\%$ to the system's total I_C-band luminosity (L_{TOT,I_C}). Therefore, we adopt $L_{3,I_C} = 0.40 \times (L_{1,I_C} + L_{2,I_C} + L_{3,I_C}) = 0.40\ L_{TOT,I_C}$. As discussed previously, given that a third light that is more significant in the V-band than in the $I_C JHK_S$-bands is needed for the simultaneous fitting of all of the observed light curves, we ascribe $L_3 = 0.40\ L_{TOT}$ for the JHK_S-bands, and $L_{3,V} = 0.60\ L_{TOT,V}$.

Furthermore, we find that the source of third light cannot be a bare star. In order to probe into the nature of the third light given the available data, we use NextGen stellar atmospheres (Hauschildt et al., 1999) to model the eclipsing components, scaling them with a luminosity ratio of 1.75. We quantify the third light contribution at all observed passbands of a third stellar component with an effective temperature between 3 000 and 6 000 K, by using NextGen atmospheres scaled to contribute 40% of the system's luminosity in the I_C-band, as found from the veiling measurements. This third light contribution is obtained by integrating the scaled spectral energy distributions over the observed passbands; and for each passband, the contribution is given by the ratio of the third component's flux to the system's total flux. We find that the trends identified above from fitting the third light levels to the light curves is not reproduced by any of the stars sampled. The *blue excess* can be modeled by a third component with a temperature above 5 000 K; however contrary to our measurements, for such star the contribution of third light in $I_C JHK_S$ is much larger than that observed in the light curves, and it decreases with increasing wavelength. It is only for a third stellar component with a temperature between 3 400 and 3 700 K, i.e., very similar to that of the eclipsing components, that we find that the third light contribution contributes an equal level in the $I_C JHK_S$-bands, as well as in the V-band, contrary to the observed light excess in the V light curve. In order to reproduce the level of third light in the V-band, an additional source of third light besides a naked star is needed.

Highly active, T Tauri stars are known to show blue excesses in their spectral

energy distributions due to either scattered X-rays or accretion flux (Whitney et al., 2003). And observationally, T Tauri stars with accretion disks are known to have veiling measurements that systematically decrease by $\sim 25\%$ from the V-band to the I_C-band (Hillenbrand et al., 1998). Thus we attribute the measured *blue excess* to the veiling continuum of a T Tauri star of effective temperature similar to that of the eclipsing components. This is consistent with the observed levels of the third light in all light curves and with the veiling measurements of §V.2.2. Even though the veiling measurements have high uncertainties ($\sim 20\%$), we find that a variation in the level of third light, contributing between 5 and 75% of the system's luminosity, does not greatly affect the derived physical parameters of Par 1802 (see §V.3).

V.3 Results: Orbital and Physical Parameters of Par 1802

We use the Wilson-Devinney (WD) based code `PHOEBE` (Prša and Zwitter, 2005) to do the simultaneous modeling of the eclipsing binary's radial velocity and light curves. The modeling tools weight both photometric and spectroscopic data by their passband r.m.s., independently of which parameters are being fitted and disregarding their physical provenance. To minimize the effect of these systematic correlations, we begin our analysis by doing an initial fit to *only* the radial velocity (RV) curves from SMC08, comprised of 11 measurements for the primary and 9 for the secondary.

We adopt the orbital period $P_{\rm orb}$ determined in §V.2.1 and initially set the inclination angle i to 90°, because the RV data provide information about $\sin i$ while i is derived from the light curves later on. The primary effective temperature $T_{\rm eff,1} = 3\,675$

$\pm$ 150 K is obtained by weighting the binary components by a luminosity ratio of 1.75 and adopting a combined effective temperature of $\sim$ 3 560 K (Luhman, 1999) from Par 1802's combined spectral type of M2 (Hillenbrand, 1997); $T_{\rm eff,1}$ remains constant throughout our analysis. The synchronicity parameters are calculated from the rotation period of the eclipsing components determined in §V.2.1, $F_1 = F_2 = P_{\rm orb}/P_{\rm rot}$ = 1.0097 $\pm$ 0.0013. We utilize for the starting point in our model fitting procedure the RV solution the best-values from SMC08 of the parameters to be refined: the semi-major axis ($a \sin i$ = 0.0501 $\pm$ 0.0006 AU), the mass ratio ($q = M_2/M_1$ = 0.98 $\pm$ 0.01), the systemic velocity of the system (v_γ = 23.7 $\pm$ 0.5 km s^{-1}), the argument of periastron (ω = 266.1 $\pm$ 1.8°), and the orbital eccentricity (e = 0.029 $\pm$ 0.005). We fit these parameters to the RV curves and obtain the best-solution which allows for the determination of the parameters that depend solely on the radial velocities, namely $a \sin i$, $M \sin^3 i$, q, and v_γ, while e and ω are later determined through the fit to the RV+LC data. These parameters and their formal uncertainties, derived conservatively from the covariance matrix of the fit to only the RV curves, are given in Table 7 and are marked with a dagger (†). The measured values of $a \sin i$, $M \sin^3 i$, q and v_γ remain fixed throughout the rest of our analysis.

We proceed to constrain the parameters that depend exclusively on the light curve (LC) data, i, $T_{\rm eff,2}$ via the temperature ratio, the surface potentials (Ω_1,Ω_2), and the luminosities, without minimizing for the other parameters. For this task, we include the previously published I_C light curve and the VI_CJHK_S light curves presented in this paper (§V.1.1). Given that the short period, low-amplitude variability is

not attributed to the eclipsing components but to a third body in the system, the light curves are rectified by removing the sinusoidal variability due to the 0.7355 d period. As mentioned in the previous section (§V.2.3), it is not possible to fit the VI_CJHK_S light curves simultaneously without including third light; there is no combination of temperature ratio and inclination that will fit the observed eclipse depths in all bands. When we are able to fit the eclipse depths of the I_CJHK_S light curves, the V-band eclipse depths are overestimated by our model. Adopting the third light levels described in §V.2.3, we are able to fit the observed eclipse depths in all bands to our eclipsing binary model. The effects of the uncertainty in the third light levels on the binary's physical parameters are minimal and are explored in detail below. By fitting the RV and LC data simultaneously (RV+LC), we are able to refine e and ω. We iterate both the LC and RV+LC solutions, until we reach a consistent set of parameters for which the reduced χ^2 of the fit is close to 1. Figure 15 presents the observed light curves with this model overplotted. The physical and orbital parameters of Par 1802 from our best solution are presented in Table 7; it includes both the formal and heuristic parameter uncertainties, as well as the uncertainties associated with our choice of third light levels. The formal statistical errors are determined directly from the WD output. `PHOEBE`'s scripting functionality allows for the Monte-Carlo sampling of parameter hyperspaces in order to determine the heuristic errors and explore the correlations between them. This exploration of the parameter correlations also ensures that the global minimum of the cost function for the solution has been reached.

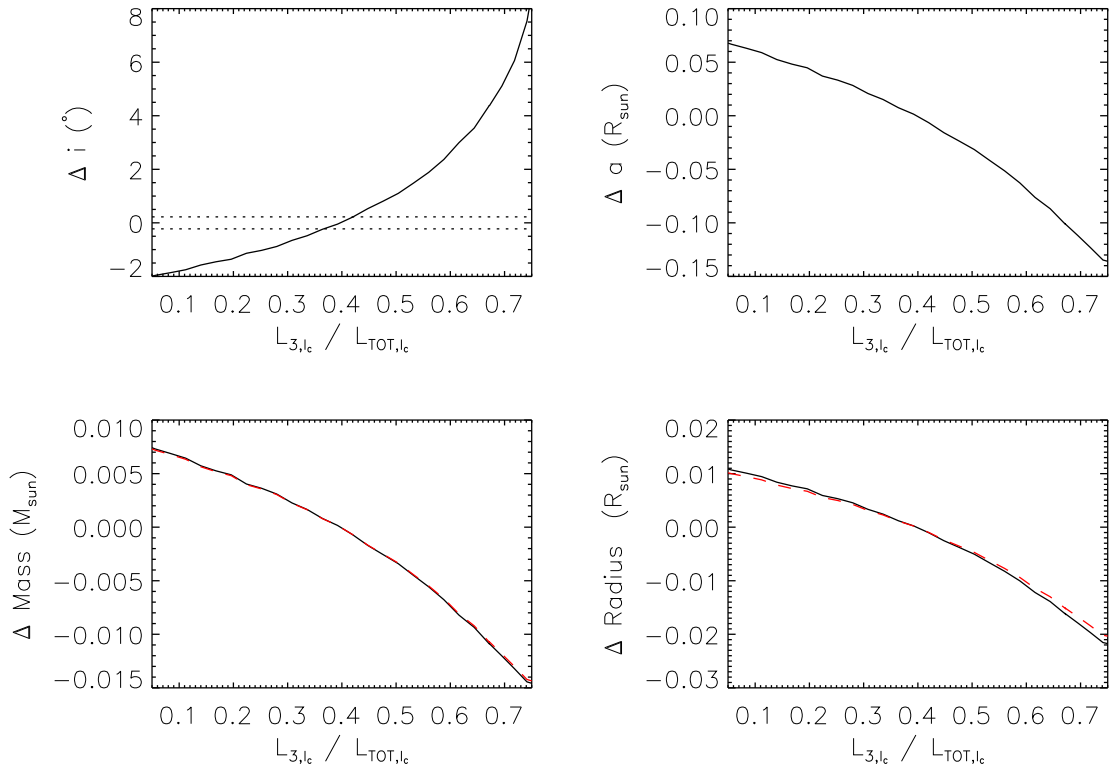

Figure 20: Effects of the I_C Third Light on the System's Parameters. By exploring the effects of the amount of third light on the inclination, we are able to determine that the system's parameters, in particular those that depend directly on i (semi-major axis, radii and masses), do not change significantly with a change in level of the third light component. A variation of the level of third light in the I_C-band, between 5 and 75% of the total luminosity of the system, corresponds to a change in inclination angle between $\sim$ 78 and 88°as shown in the top-left panel. The formal error for the inclination ($\pm 1\sigma$) is denoted by the horizontal dotted lines in the top-left panel; the formal uncertainties for the semi-major axis, the masses and the radii are larger than the effect of the variation of the third light on these parameters. This variation of the third light, and consequently of i, corresponds to a change in the semi-major axis is of less than $\pm$ 1.5% (top-right panel). It also translates into a change of less than $\pm$ 4% in the masses, corresponding to less than $\pm$ 0.015 $M_\odot$ (bottom-left panel). The solid line and dashed line represent the change in the primary and secondary masses, respectively. The change in the radii of the primary and secondary components of +0.01 and –0.02 $R_\odot$ is presented in the bottom-right panel by the solid line and dashed line, respectively.

The inclination angle and the levels of third light are highly degenerate parameters, i.e., an increase in the inclination angle may be compensated by an increase in the amount of third light rendering the same goodness of the fit. The observational limits on the *real* amount of third light are given by the veiling measurements (§V.2.2). The relative contribution of amount of third light in the different bands is constrained by the observed eclipse depths, such that the third light level in the V-band is always higher than in the $I_C JHK_S$-bands. To explore this degeneracy in the parameter space, we quantify the effects of the variation of the levels of third light on the system parameters, in particular those that depend strongly on the inclination. From the radial velocity data, we can measure the values of $M \sin^3 i$ and $a \sin i$; and from the photometry, we can determine the sum of the fractional radii. A change in the inclination would therefore affect most strongly the semi-major axis, the radii, and the masses. The temperature ratio is weakly dependent on a change in the inclination and its corresponding levels of third light, because it is constrained by the observed relative depths of the eclipses in the different passbands. We vary the third light level in the I_C-band, such that it contributes between 5 and 75% of the system's total luminosity, adjusting the third light level in the other bands according to the trends identified in §V.2.3. Figure 20 shows the relationship between the change in third light levels and the inclination angle, the semi-major axis and the measured masses and radii of the eclipsing components. We find that the corresponding value for the inclination angle for this variation in third light lies between $\sim$ 78 and 88°. Since this change in the inclination is greater than its formal error of $\sim 0.2°$, we adopt its

uncertainty in degrees to be $^{+\ 8.0}_{-\ 2.0}$. Accordingly, the change in the value of the semi-major axis as the level of third light is varied is less than ± 2%. Consequently, we are able to determine that the masses vary by less than ± 4% or ± 0.015 $M_{\odot}$, which is comparable to the uncertainties in the masses ($\sim$ 0.02 $M_{\odot}$) if we only include the formal $\sigma_i = 0.2°$. However, these changes are well below our formal uncertainty of 0.032 $M_{\odot}$, which includes the uncertainty in i to be 8.0°. The radii change by $^{+\ 0.01}_{-\ 0.02}$ $R_{\odot}$, or ± 1%. The uncertainty in i due to the level of third light is not the main source of error in the radii. When we include an uncertainty of 8.0° for the value of i, the uncertainty in the radii are 0.11 and 0.08 $R_{\odot}$ for the primary and the secondary, respectively. The uncertainties of the system parameters that depend on i have been calculated with $\sigma_i = 8.0°$ and are marked with a double-dagger (‡) in Table 7.

We are able to determine that the eccentricity of Par 1802 is in fact measurable given our data set and significantly different than zero, $e = 0.0166\ ^{+\ 0.0017}_{-\ 0.0026}$. Initial estimates of e and ω are obtained from the separation in phase between the secondary eclipse minimum $t_{\mathrm{II},ph}$ and primary's $t_{\mathrm{I},ph}$ and from the duration of each eclipse Θ_i. The eccentricity and angle of periastron are related as follows: $e\cos\omega = \pi\ (t_{II,ph} - t_{I,ph} - 1/2)/(1 + \csc^2 i)$ and $e\sin\omega \approx (\Theta_p - \Theta_s)/(\Theta_p + \Theta_s)$ (Kallrath and Milone, 2009). Therefore by measuring the separation between the minima in the light curves, the lower limit for the eccentricity may be estimated, when $|\cos\omega| = 1$. In order to measure the separation and duration of the eclipses, we fit a Gaussian to both minima in the phased I_C-band and obtain from the phases at which they occur that their separation is $t_{II,ph} - t_{I,ph} = 0.49799 \pm 0.00025$; hence, $e \geq 0.0031 \pm 0.0004$. The

separation of the minima in conjunction with the measured durations, $\Theta_p = 0.1010 \pm 0.0007$ and $\Theta_s = 0.0877 \pm 0.0012$, render $\omega = 1.514 \pm 0.004\ \pi$ radians and $e = 0.071 \pm 0.008$.

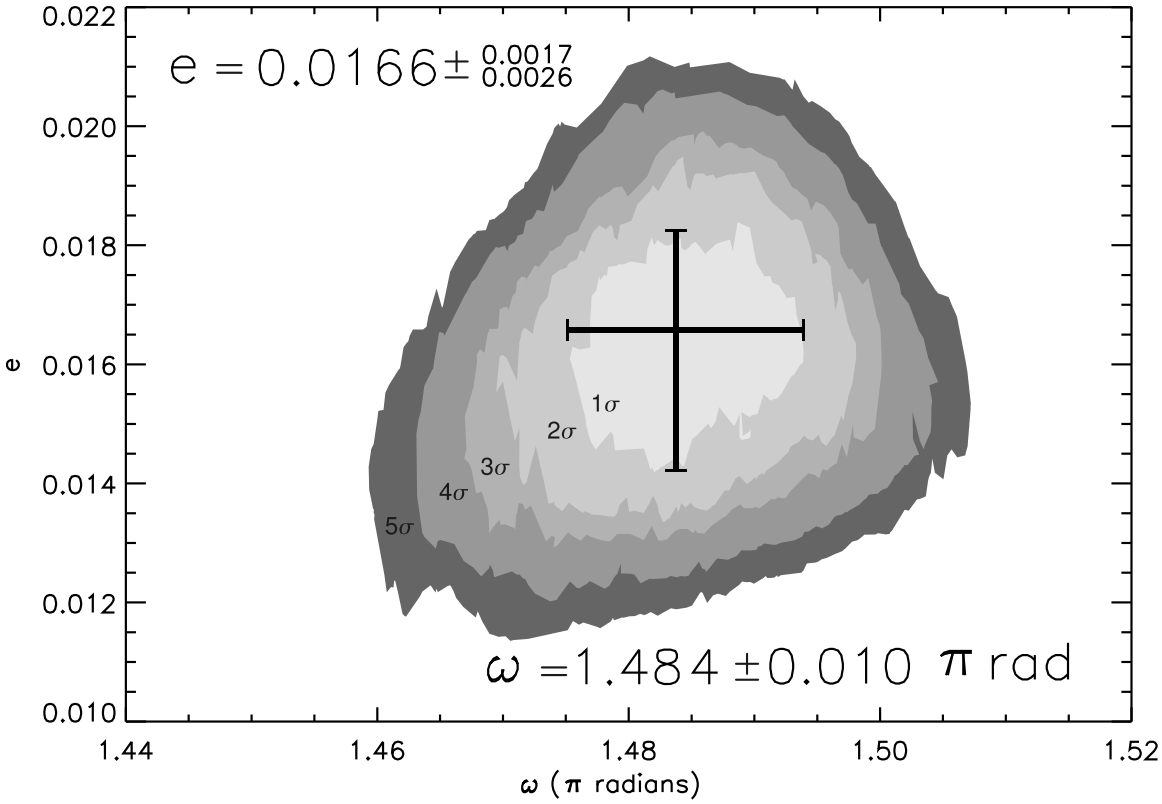

Figure 21: RV+LC Joint Confidence Levels for $e - \omega$. Given our dataset, we are able to measure the very small but significant orbital eccentricity of the eclipsing binary. The heuristic errors of the eccentricity e and the argument of periastron ω are estimated by the variation of a χ^2-distribution with two degrees of freedom with e and ω. The center of the cross marks the point at which the χ^2 of the RV+LC fit attains its minimum value; its length and width indicate the 1-σ uncertainties for the sampled parameters as given by the innermost contour level. Each subsequent contour represents a 1-σ increase. The RV+LC parameter hyperspace is sampled for $0.0 < \omega < 2\pi$ and $0.0 < e < 0.1$; this is the same parameter range sampled for the LC contours shown in Fig. 22.

By sampling the parameter cross-section between e and ω, we are able to determine

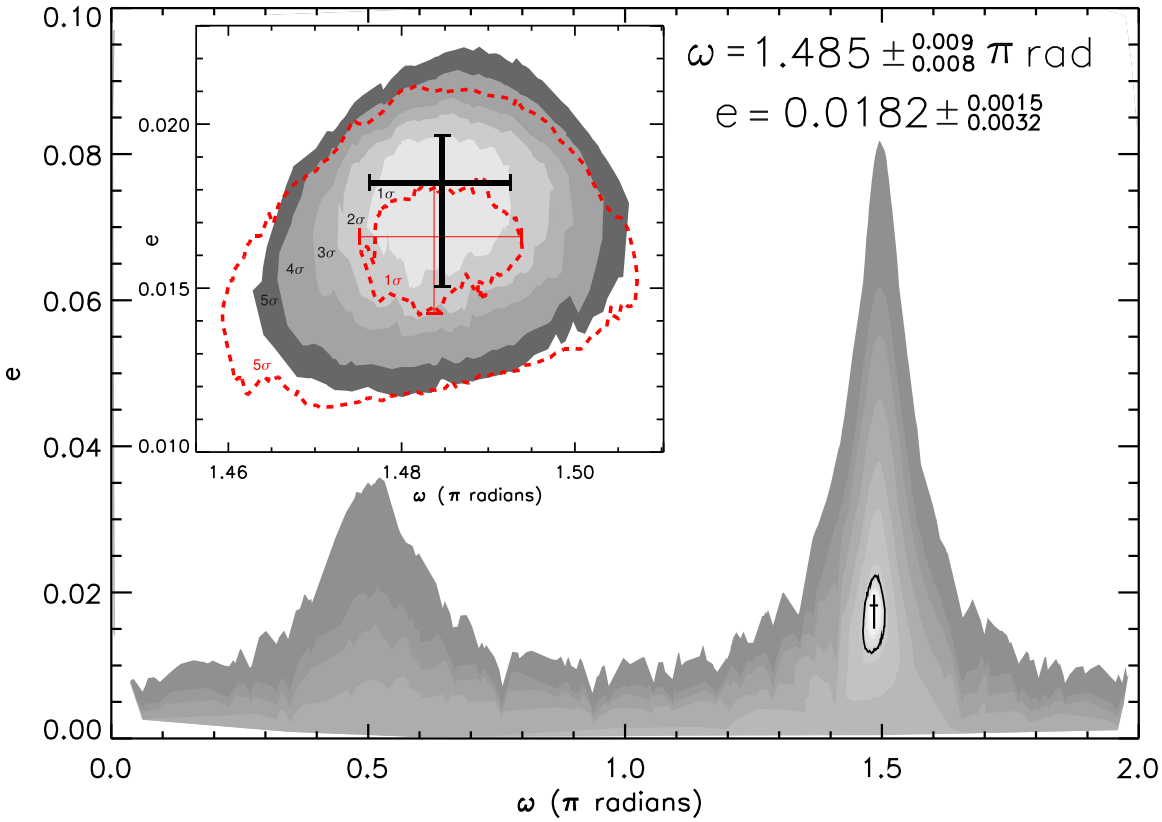

Figure 22: LC Joint Confidence Levels for $e-\omega$. The LC confidence contours allows us to confirm that the values for e and ω from the RV+LC contours are not systematically skewed by the weighting of the data, due to the abundant number of photometric data in comparison to the number of RV measurements. The figure shows the sampled parameter cross section in its entirety. The cross marks the lowest-χ^2 point to the LC fit with 1-σ uncertainties, surrounded by the solid line 5-σ confidence level. The shaded contours beyond 5-σ do not correspond to a particular uncertainty level but are shown to display the two valleys in χ^2 when the orbit's semi-major axis is parallel to the line-of-sight. The inset shows in detail the confidence interval for e and ω within 5-σ and for comparison, the dashed lines denote the 1 and 5-σ RV+LC contours from Fig. 21.

the best-values of these parameters consistent with those estimated above, as well as their heuristic uncertainties. Figure 21 shows the joint confidence levels for e and ω following the variation of a χ^2-distribution with two degrees of freedom around the RV+LC solution's minimum. The innermost contour represents a confidence level of 1-σ, and each subsequent level corresponds to an increment of one σ. This cross section was sampled $\sim$ 1750 times by randomly selecting values for e between 0.0 and 0.1, and for ω between 0 and 2π radians. The phase shift, which gives the orbital phase at which the primary eclipse occurs, is strongly correlated with both explored parameters and is therefore minimized for each set of randomly selected values, whereas the rest of the parameters are less correlated and kept constant at their best-values. In order to verify that e, ω and their uncertainties are not artificially skewed by the weighting of both the RV and light curves as undertaken in `PHOEBE` by WD, given that our data set is comprised mostly of photometric measurements, we sampled the same range in e and ω about 1900 times fitting to the light curves alone and obtaining their LC confidence contour levels. We find that the LC contours, shown in Fig. 22, are very similar to the RV+LC contours (Fig. 21). The minimum value of χ^2 to the RV+LC fit is for $e = 0.0166\ ^{+0.0017}_{-0.0026}$ and for $\omega = 1.484 \pm 0.010\ \pi$ radians; while for the LC fit, it is for $e = 0.0182\ ^{+0.0015}_{-0.0032}$ and for $\omega = 1.485\ ^{+0.009}_{-0.008}\ \pi$ radians. The 5-σ contour level is denoted by the black contour around the lowest-χ^2 point marked by the cross. The shaded contours are for larger changes in χ^2, and do not correspond to specific sigma levels. We plot beyond the 5-σ level to show the two valleys in the parameter hyperspace when ω is close to $\pi/2$ and to $3\pi/2$, i.e., when

the orbit's semi-major axis is aligned with the line-of-sight thus allowing for larger eccentricities. The detailed LC contours up to 5-σ are shown in the inset in Fig. 22; for comparison, the 1 and 5-σ RV+LC contours are overplotted in the dashed lines. We find that both sets of contours are consistent, and thus we adopt the values of e and ω and their heuristic uncertainties from the RV+LC contours.

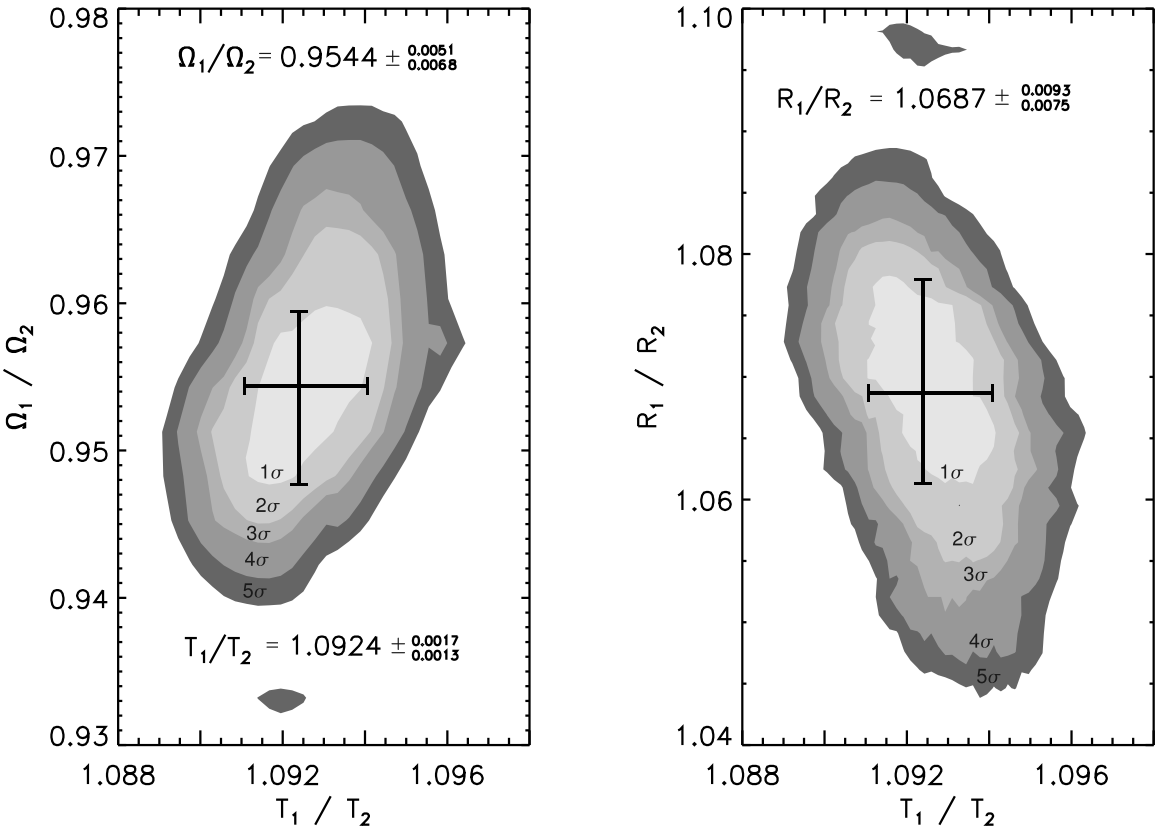

Figure 23: Joint Confidence Levels for $(T_{\rm eff,1}/T_{\rm eff,2})$ – (R_1/R_2). Similar to Fig. 21 and Fig. 22, the significance levels given by the contours are representative of the change in χ^2 as the ratios of temperatures and radii are explored. Even though the masses of the components are almost equal, $q = 0.985 \pm 0.029$, the effective temperatures differ by $\sim 9\%$ and the radii of the eclipsing binary components by $\sim 7\%$.

We confirm that the ratio of effective temperatures as shown in SMC08 is different

Table 7: Orbital and Physical Parameters of Par 1802

	RVs + I_C[1]	RVs + VI_CJHK_S
Orbital period, $P_{\rm orb}$ (d)	4.673843 ± 0.000068	4.673903 ± 0.000060
Eccentricity, e	0.029 ± 0.005	$0.0166\ ^{+\ 0.0017}_{-\ 0.0026}$
Orientation of periastron, ω (π rads)	1.478 ± 0.010	1.484 ± 0.010
Semi-major axis, $a \sin i$ (AU)	0.0501 ± 0.0006	0.0496 ± 0.0008[†]
Inclination angle, i (°)	78.1 ± 0.6	$80.8\ ^{+\ 8.0‡}_{-\ 2.0}$
Systemic velocity, v_γ (km s^{-1})	23.7 ± 0.5	23.4 ± 0.7[†]
Primary semi-amplitude, K_1 (km s^{-1})	57.74 ± 0.75[a]	57.28 ± 1.22
Secondary semi-amplitude, K_2 (km s^{-1})	58.92 ± 0.95[a]	58.19 ± 2.14
Mass ratio, $q \equiv M_2/M_1$	0.98 ± 0.01	0.985 ± 0.029[†]
Total mass, $M \sin^3 i$ ($M_\odot$)	0.768 ± 0.028	0.745 ± 0.034[†]
Primary mass, M_1 ($M_\odot$)	0.414 ± 0.015	0.391 ± 0.032[‡]
Secondary mass, M_2 ($M_\odot$)	0.406 ± 0.014	0.385 ± 0.032[‡]
Primary radius, R_1 ($R_\odot$)	1.82 ± 0.05	1.73 ± 0.11[‡]
Secondary radius, R_2 ($R_\odot$)	1.69 ± 0.05	1.62 ± 0.08[‡]
Primary gravity, $\log g_1$	3.54 ± 0.09[a]	3.55 ± 0.07[‡]
Secondary gravity, $\log g_2$	3.62 ± 0.10[a]	3.61 ± 0.06[‡]
Primary surface potential, Ω_1	...	7.3 ± 0.4
Secondary surface potential, Ω_2	...	7.6 ± 0.3
Primary synchronicity parameter, F_1	...	1.0097 ± 0.0013
Secondary synchronicity parameter, F_2	...	1.0097 ± 0.0013
Effective temperature ratio, $T_{\rm eff,1}/T_{\rm eff,2}$	1.084 ± 0.007	1.0924 ± 0.0017

[1] Previously published results (SMC08).

[a] Calculated from parameters and uncertainties in SMC08.

[†] **The uncertainties in these parameters are conservatively estimated from the formal errors of a fit to the RV data alone. See §V.3.**

[‡] **The uncertainty in the inclination is conservatively estimated from a variation in the level of third light between 5 and 75% of the system's total luminosity, and is propagated into the uncertainty in these parameters, since they depend on i. See §V.3.**

from unity, $T_{\rm eff,1}/T_{\rm eff,2} = 1.0924\ ^{+0.0017}_{-0.0013}$; and we also find this disparity in the case of the ratio of the eclipsing components radii, $R_1/R_2 = 1.0687\ ^{+0.0093}_{-0.0075}$. We sampled the parameter hyperspace between $(T_{\rm eff,1}/T_{\rm eff,2})$ and (R_1/R_2) over 2000 times, shown in Fig. 23, in order to confirm the significance of the differences in the radii and temperatures of the eclipsing components of Par 1802. We explore the temperature ratio between 1.0382 and 1.1271. The radius for the component of a detached eclipsing binary depends on the surface potentials as $\sim 1/\Omega_j$; so the ratio of the radii was sampled by choosing values for Ω_1 between 5.5 and 8.4, and minimizing for Ω_2. To facilitate the convergence of Ω_2, we exploit the fact that the sum of the radii must remain the same due to observational constraints.

The fundamental parameters of Par 1802 and their uncertainties obtained through the modeling of the observed radial and light curves and from the careful exploration of the parameter correlations are summarized in Table 7. The most conservative uncertainties are adopted for each parameter; we include the uncertainty due to a variation on the third light level in the determination of the derived parameters' errors, like those of the individual masses, the radii and the surface gravities.

V.4 Discussion

Par 1802 is a unique system providing important and valuable observational constraints in the low-mass regime at the earliest evolutionary stages. Not only does it provide precise and direct measurements of the mass and the radius of each of its components; but because their masses are almost equal, it also constrains the degree

to which the coevality of binary components should be considered. We are able to measure the radii for the eclipsing components that are large as expected for PMS stars, but they differ by 7%. Their effective temperatures are also confirmed to be dissimilar by 9%. As discussed in SMC08, a difference in age for stars of 0.4 $M_{\odot}$ of $\sim$ 300 000 years would explain this discrepancy, with the larger star being younger than its companion, because there is a fast evolution predicted by the theoretical evolutionary models of D'Antona and Mazzitelli (1997) around an age of 1 Myr. Mass equalizing mechanisms during the formation process may be the cause of this age difference between the components of twin binaries (Simon and Obbie, 2009). The early tidal evolution of close binary systems is also constrained by the measured rotation period of the binary components, which is slightly faster than the orbital period, consistent with quasi-synchronization, and by the small but significant eccentricity of the orbit. Furthermore, we find observational evidence of the existence of a third component in the system.

V.4.1 Eccentricity, Rotation Period and Tidal Evolution

The theory of tidal evolution predicts that the timescales for synchronization of close binaries are shorter than the timescale for their orbits to be circularized (e.g., Mazeh, 2008). According to Zahn (1977), the synchronization period (in years) for a binary where both components have convective envelopes with a mass ratio q and an orbital period $P_{\rm orb}$ (in days) is given by $t_{\rm synch} \sim 10^4((1+q)/(2q))^2 P_{\rm orb}^4$; and the circularization period is $t_{\rm circ} \sim 10^6 q^{-1}((1+q)/2)^{5/3} P_{\rm orb}^{16/3}$ years. For Par 1802, $t_{\rm synch}$

is close to 5 Myrs while $t_{\rm circ}$ is $\sim$ 3.8 Gyrs. And in fact, we find that the components are rotating quasi-synchronously and that the orbit has a non-zero eccentricity.

From the eclipsing binary modeling, we confirm that the orbit is not circular with a non-zero eccentricity of $e = 0.0166 \pm 0.003$. We measure the photometric rotation period of the binary components in §V.2.1 and find it to be $P_{\rm rot} = 4.629 \pm 0.006$ days. This period is very close to but significantly different from the orbital period of the binary; the system is quasi-synchronized. For non-circular orbits, tidal interaction is strongest around periastron and therefore the binary components synchronize to the pseudo-synchronization rotational velocity as described by Hut (1981). If Par 1802 was rotating pseudo-synchronously and considering the system's measured eccentricity, its components would have to rotate with a period of 4.6662 days which is more than 3-σ longer than the measured $P_{\rm rot}$. On the other hand, if we consider $P_{\rm rot}$ to be the pseudo-synchronization period of the binary, then the eccentricity of the orbit would need to be $\sim$ 0.04 which is well outside our 5-σ confidence level for the eccentricity (see Fig. 21 and Fig. 22). The theory of tidal evolution during the PMS phase is not well determined because the initial conditions range from system to system and there are different mechanism that affect the evolution of the rotation of the binary components which may counteract each other: the contraction and conservation of angular momentum spinning up the stars, which is in itself challenging, and the tidal interactions slowing them down. Very small, non-zero eccentricities in close binaries, like the one we are able to precisely measure, are typically ignored and the orbits are considered circular.

V.4.2 The Third Stellar Component

As mentioned in the previous sections, the observational evidence for the existence of a third component in Par 1802 are: a) the VI_CJHK_S light curve modulation by a 0.7355 day period during all observed epochs (§V.2.1), b) the measured excess continuum or veiling found in the spectra (§V.2.2), and c) the need of third light for the simultaneous modeling of the VI_CJHK_S light curves (§V.2.3, §V.3).

Since the ONC is in front of a very dense, optically-thick cloud, the source of third light cannot be a background object, and it is not likely a foreground main sequence star because of the observed spectral veiling, characteristic of T Tauri stars. It is therefore most likely to be associated with the young cluster. The contribution of the third component to the system's luminosity is limited in order to maintain Par 1802 within the ONC, which is at a distance of 436 ± 20 pc (O'Dell and Henney, 2008). Appendix F contains an `IDL` script that calculates the distance to Par 1802 taking into account different values of interstellar extinction. Considering a third body that contributes 40% to the system's total luminosity, as we have determined for the I_C-band, the distance to Par 1802 with an extinction of $A_V = 0.0$ visual magnitudes is 390 ± 65 pc; for an extinction of $A_V = 0.5$, as proposed in SMC08, the distance would be 490 ± 65 pc. Both of these distances are consistent with the distance to the low-mass stellar population associated with the Orion Nebula. A third component that contributes more than 40% of the system's total luminosity would therefore set the distance to Par 1802 beyond that of the ONC. Par 1802's third stellar component is therefore unlikely to be an early-type star with a PMS radius that would dominate

the light of the system.

The observed short-period, low-amplitude variability is likely to arise from a rapidly rotating star and cannot be attributed to either of the binary components because there is no evidence for such rapid rotation in their spectra. The fact that we detect the short-period variability in all filters indicates that there is a contribution of the third star at those wavelengths. Therefore, the third body cannot be an early-type star that is still embedded within its parent cloud. Even though this would satisfy the low contribution to the system's luminosity, we would not be able to observe the spot-induced modulation in all light curves. On the other hand, an active late-type star, that is contributing 40% of the system's luminosity and is rotating with a 0.7355 d period can cause the observed spot modulation ($\sim 3\%$ in the I_C-band) if its intrinsic variability is $\sim 5\%$, which is within the typical observed variability for PMS stars. Moreover, other low-mass stars in the ONC have been found to have similarly fast rotation periods (e.g. Stassun et al., 1999).

The spectrum of a rapidly rotating late-type star, which is diluted by the eclipsing binary's light, would not be easily identified in the spectra of the system. This may explain the featureless extra continuum or veiling found in the spectra. Studies based on the modeling of the spectral energy distributions of T Tauri stars are known to show veiling in the blue part of the spectrum for highly active stars (Whitney et al., 2003). The third body might be such an active, late-type stellar component, which would explain the blue excess found for Par 1802 in the levels of third light in the light curve modeling and from the veiling measurements. And though the binary

components are shown in SMC08 to not have circumstellar or circumbinary material, these might have been removed by tidal forces, which would not have as strong an effect on the third body's circumstellar material.

The observational constraints described above do not provide enough information to enable us to determine the mass nor the spectral type of the third component of Par 1802. In fact, we cannot entirely rule out the possibility that the third star is an unrelated star along the line of sight. However, as we discuss above, it is very unlikely to be either a foreground or background field star, so it is likely within the ONC, in which case the probability of being projected within $\sim$ 1" line of sight is very low. Moreover, we are able to set limits to the amount of light the third body contributes to the system. As a consistency check, we fit the broadband photometry for Par 1802 to a composite model spectral energy distribution, which includes the eclipsing pair and a third stellar component of similar effective temperature and radius with a blue excess typical of T Tauri stars. We find that with a level of third light and blue excess, the broadband photometry agrees with the effective temperatures and radii of the eclipsing components.

A third stellar component in Par 1802 has been previously suggested (CSM07) by a long term trend identified in the residuals of the orbit solution. The data span about 10 years; the oldest of which are found to be well above 3-σ from the calculated orbit. If we consider a third body with a mass similar to the EB components ($\sim$ 0.4 $M_{\odot}$), as suggested by above, orbiting the EB with a period of $\sim$ 15 years at a distance of about 6 AU, the maximum shift in the radial velocities of the EB would be $\sim$ 18

km s^{-1}. Such third body in Par 1802 would be consistent with the scatter found in residuals presented in CSM07. In fact, the existence of the third body in an eccentric orbit may be the cause for the low-eccentricity found in the EB.

We propose that the third body of Par 1802 is a rapidly rotating, PMS late-type star, explaining the observed low-amplitude variability in the light curves with the 0.7355 d period. Because of its fast rotation and because its light it diluted with the light from the eclipsing pair, we are unable to identify any of its spectral features. Motivated by the observed spot-modulation in the light curves, this third body is probably active and may still have circumstellar material from which it is accreting or which is scattering X-rays causing the observed blue excess found in the levels of third light needed to fit the light curves, and perhaps also causing the spectral veiling.

CHAPTER VI

ECLIPSING BROWN DWARFS

This chapter exemplifies the use of the analyses and techniques described in the previous chapters to model the eclipsing binary system, 2MASS J05352184-0546085, and has been published as Gómez Maqueo Chew et al. (2009).

The discovery of the system 2MASS J05352184–0546085 (hereafter 2M0535−05), the first eclipsing binary system comprised of two brown dwarfs, was presented by Stassun et al. (2006), hereafter SMV06. With a reported orbital period of $P_{\rm orb} = 9.779621 \pm 0.000042$ d, 2M0535−05 was found as part of a photometric survey searching for variability in the Orion Nebula Cluster. Through the simultaneous radial velocity and I_C-band light curve analysis of this fully detached system, they obtained masses of $M_1 = 0.054 \pm 0.005$ $M_\odot$ and $M_2 = 0.034 \pm 0.003$ $M_\odot$ for the primary and secondary components, respectively, with corresponding radii of $R_1 = 0.669 \pm 0.018$ $R_\odot$ and $R_2 = 0.511 \pm 0.026$ $R_\odot$. They found a surprising reversal of surface brightnesses in which the less massive component radiates more per unit surface area (i.e., has a higher effective temperature) than the more massive one, contrary to what is expected for coeval brown dwarfs (Baraffe et al., 1998).

A follow-up analysis of 2M0535−05 was presented by Stassun et al. (2007, hereafter SMV07) in which it was suggested that the apparent temperature reversal in 2M0535−05 could be the result of preferentially strong magnetic activity on the pri-

mary brown dwarf. This hypothesis was shown by Chabrier et al. (2007) to be theoretically plausible, and was then reinforced empirically when Reiners et al. (2007) found that the primary brown dwarf rotates $\gtrsim$ 2× faster and exhibits $\gtrsim$ 7× stronger Hα emission than the secondary. One manifestation of enhanced activity on the primary brown dwarf should be the presence of large, cool surface spots (Chabrier et al., 2007). If present, such spots should produce photometric variations that are periodically modulated by the rotation of the brown dwarf. Indeed, the presence of low-amplitude variations in the I_C-band light curve of 2M0535−05 was noted in SMV07; however an analysis of such variation was deferred to the present study.

This work broadens the previous analyses of 2M0535−05 with the addition of near-infrared (JHK_S) light curves, and investigates the intrinsic variability of the light curves in more detail. The near-infrared observations and their reduction are described in Sec. VI.1 and analyzed in Sec. VI.2. A periodicity analysis of the out-of-eclipse phases of the light curves in Sec. VI.2.1 yields the rotation periods of the two components of the binary to be $P_{\rm rot,1} = 3.293 \pm 0.001$ d and $P_{\rm rot,2} = 14.05 \pm 0.05$ d, consistent with the $v \sin i$ measured by Reiners et al. (2007) and the previously measured radii. The modeling of the JHK_S light curves together with the previously published I_C light curve and radial velocity data is described in Sec. VI.2.2, from which we determine refined measurements of the system's physical parameters. The apparent temperature reversal found in the previous studies is confirmed again with the addition of the JHK_S light curves to the analysis.

Section VI.3 incorporates surface spots into the light curve modeling. In par-

ticular, we assess the properties (areal coverage and temperature) of the spots that are required to both reproduce the observed low-amplitude variations and permit the surrounding photospheric temperatures of the two brown dwarfs to be in agreement with theoretical expectation for young brown dwarfs. We find that a small cool spot ($\sim$ 10% areal coverage and $\sim$ 10% cooler than the surrounding photosphere) on each of the brown dwarfs can reproduce the observed low-amplitude variations. Then, by introducing additional spots that uniformly cover $\sim$ 65% of the primary's surface, we are able to simultaneously reproduce the observed surface brightness ratio of the two brown dwarfs (i.e., the apparent temperature reversal) while bringing the underlying temperature of the primary into agreement with the predictions of theoretical models. Finally, we discuss our findings in Sec. VI.4.

VI.1 Near-Infrared Light Curves

The primary focus of this work is primarily to extend the published spectroscopic and photometric analyses (SMV06, SMV07) of 2M0535−05 with the addition of the near-infrared photometric light curves in the J (1.2 μ m), H (1.6 μ m) and K_S (2.2 μ m) passbands. The inclusion of more light curves in the modeling allows us to further constrain the system's parameters, in particular the temperatures and radii of the components. The multi-band analysis also probes the nature of the low-amplitude variability.

VI.1.1 Near-Infrared Photometric Observations

As mentioned in Chapter II, the observations of 2M0535−05 here presented were taken in the 2MASS near-infrared bands JHK_S from 2003 October to 2006 April at Cerro Tololo Inter-American Observatory in Chile. They were observed with the SMARTS 1.3-m telescope using the ANDICAM instrument which allows for simultaneous optical and infrared imaging (the optical measurements have been reported in SMV06 and SMV07). The observations in the near-infrared were made in sets of 7 dither positions providing a total of 362 measurements in J, 567 in H and 385 in K_S spread over five observing seasons. The integration times were typically of 490 seconds for the JHK_S passbands. Table 8 describes the observing campaigns in full detail, while Appendix G contains Tables 16–18 that provide a sample of the individual measurements in the JHK_S bands. The full data set may be found in the online version of the paper by Gómez Maqueo Chew et al. (2009). The mean near-infrared magnitudes of 2M0535−05 are $J = 14.646 \pm 0.031$, $H = 13.901 \pm 0.043$, and $K_S = 13.473 \pm 0.031$ (Skrutskie et al., 2006).

VI.1.2 Data Reduction

The data were reduced differently depending on the dome flat acquisition as described in Chapter II. For observations made between October 2003 and March 2004, those comprising the data set I and affecting more than 50 percent of the H light curve, the dome flats were obtained without information of the mirror's position. A composite dome flat was created by subtracting a median combination of ∼10 images

Table 8: Photometric Time Series Observations of 2M0535−05

	UT Dates	Julian Dates Range	Filter	Exp[a]	Obs[b]
I	2003 10 09 – 2004 03 16	2452922.728 – 2453081.568	H	525	303
II	2004 10 01 – 2004 11 30	2453280.731 – 2453340.726	J	490	105
		2453280.736 – 2453340.733	K_s	490	104
III	2005 02 01 – 2005 03 15	2453403.540 – 2453445.589	J	490	123
		2453403.532 – 2453445.579	H	490	123
		2453403.547 – 2453445.595	K_s	490	115
IV	2005 10 02 – 2005 12 23	2453646.828 – 2453728.701	J	490	55
		2453646.821 – 2453728.694	H	490	53
		2453646.836 – 2453728.717	K_s	490	103
V	2006 01 09 – 2006 04 09	2453745.651 – 2453835.506	J	490	81
		2453745.643 – 2453835.498	H	490	89
		2453745.658 – 2453835.514	K_s	490	64

[a] Total exposure time in seconds of the seven dithered positions.

[b] Number of observations per season.

taken with the dome lights on minus the median combination of ∼10 images taken with the lights off in order to reduce the infrared contribution in the final images of sources such as the telescope, optical components and the sky. The procedure to then reduce data set I consisted of the following steps: a sky image is formed from the median combination of the 7 dithers; it was then normalized to the background of each individual image and subtracted from each separately; every image was then divided by the normalized flat; the dithers were aligned; the images were cropped, and they were combined by doing a pixel-by-pixel average.

For images taken from October 2004 onward, dome flats were provided individually for each of the 7 dither positions, proving essentially helpful in removing the interference pattern of sky emission lines characteristic of each of the mirror posi-

tions as well as the other infrared contributions. Each of the seven furnished dome flats follow the same combination as did the dome flats described in the previous paragraph. The individual dome flats for each of the mirror's dithers allowed for the creation of separate flats for each mirror position. Sky flats were created from the median combination of ∼10 images with slightly different star fields for each distinct dither position, so that the stars present in the field averaged out and provided a flat image. This was possible since the observed field is not a very crowded one. For each of the remaining observing seasons, new sky flats were created in order to correct for any changes in the dithering and for any physical changes in the instrument. The reduction process is slightly different than for the first data set: the dark was first subtracted from the raw image; followed by the corresponding normalized sky flat, which depended on the mirror position at which the images were taken. The image was then divided by the corresponding normalized dome flat. Once this was done, the calibration resembles that of data set I: the dithered images were shifted and cropped in order to be median combined as to obtain the final image.

Differential aperture photometry was done using the `IRAF` package `APPHOT`. The comparison star was chosen because it appears in all of the reduced observations of 2M0535−05 and because it is non-variable in the I_C-band observations. The phased JHK_S light curves are presented in Fig. 24.

We do not report uncertainties on the individual differential photometric measurements in Tables 16–18, because the light curves precision is dominated by systematics. However, the standard deviation of the out-of-eclipse portions of the light curves gives

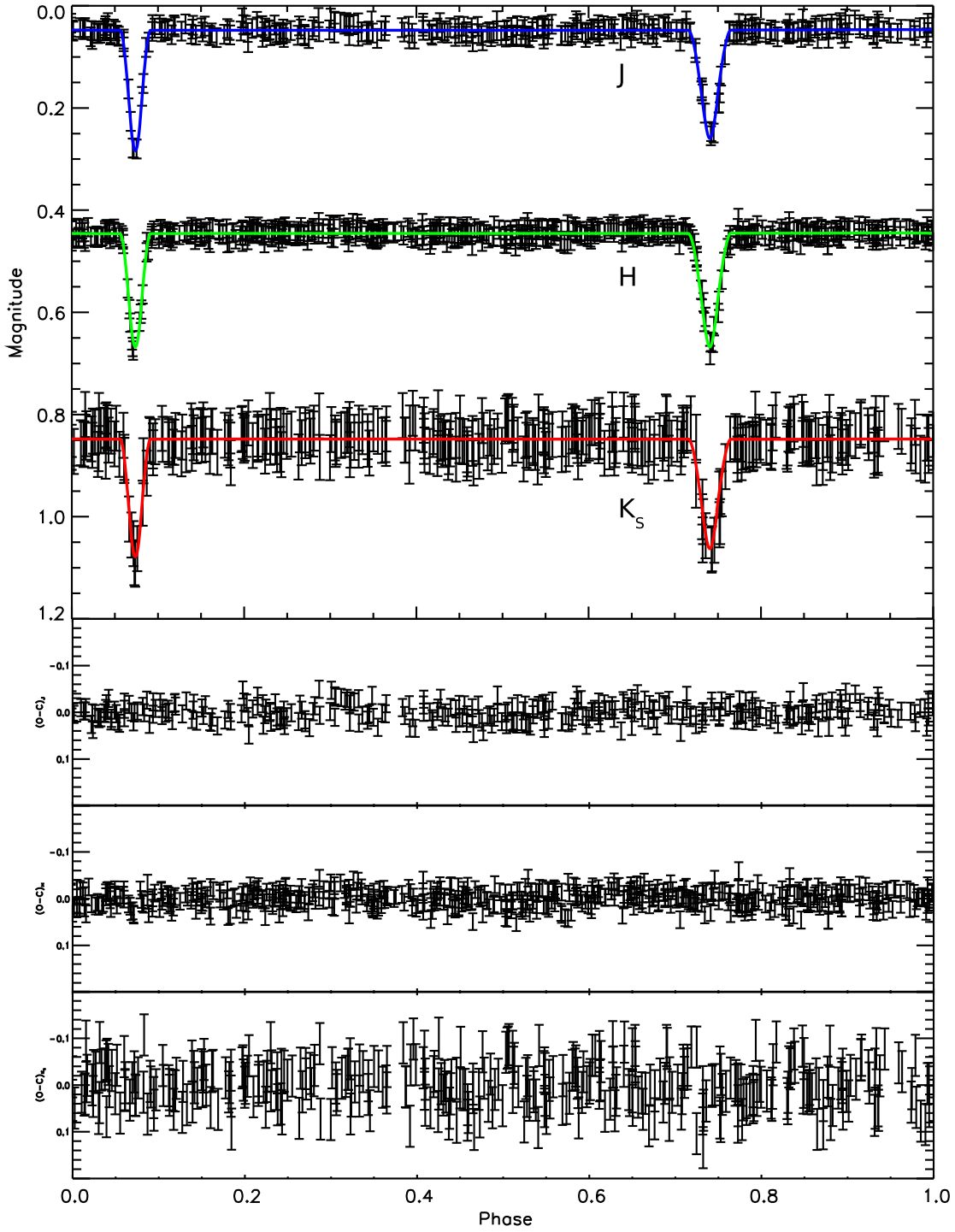

Figure 24: JHK_S light curves of 2M0535−05. The observed data points for each band are plotted with their corresponding uncertainties as described on §VI.1.2 and are displaced by 0.7 magnitudes for clarity from the light curve above. The solid lines represent the light curve model of the simultaneous fit to the radial velocity measurements and the $I_C JHK_S$ photometric data (see §VI.2.2 for discussion of the modeling procedure, and see Table 10 for parameters). The residuals of the fits are also shown.

a measure of the photometric scatter in each of the bands. While the JH light curves present a similar scatter, $\sigma_J = \sigma_H = 0.02$, the interference pattern of the sky emission lines is more significant in the K_S-band making the scatter larger, $\sigma_{K_S} = 0.04$. As we show below, this photometric scatter includes low-amplitude intrinsic variations due to the rotation of 2M0535−05's components.

VI.2 Light Curve Analysis

The JHK_S light curves described in the previous section are analyzed for periodicities apart from those due to the eclipsing nature of the binary (§VI.2.1). Then they are modeled in conjunction with the available radial velocities and I_C light curve in order to obtain the system's physical parameters (§VI.2.2). The thorough treatment of surface spots is introduced to the light curve solution in Sec. VI.3.

VI.2.1 Rotation periods

The light curves, both in the I_C and the JHK_S bands, present several periodicities. The most obvious period corresponds to that of the eclipses which recur on the orbital period, $P_{\rm orb} = 9.779556 \pm 0.000019$ d (Stassun et al., 2007). In addition, the light curves in the observed bandpasses present a low-amplitude variability, with a peak-to-peak amplitude of ∼0.02–0.04 magnitudes, noticeable in the out-of-eclipse phases. We speculate that this type of periodic signal is due to the rotation of one or both components, resulting from spots on their surfaces rotating in and out of view (e.g., Bouvier et al., 1993; Stassun et al., 1999). Another possible explanation for the

low-amplitude variations is intrinsic pulsation of one or both of the components. However, young brown dwarfs are expected to pulsate with periods of only a few hours (Palla and Baraffe, 2005), whereas we find periods of $P_1 = 3.293 \pm 0.001$ d and $P_2 = 14.05 \pm 0.05$ d (see below). Thus in what follows, for consistency we refer to these periods as $P_{\rm rot,1}$ and $P_{\rm rot,2}$.

The light-curve data in the I_C and JHK_S bands corresponding to the out-of-eclipse phases were searched for periods between 0.1 and 20 d using the Lomb-Scargle periodogram (Scargle, 1982), well suited for unevenly sampled data. The resulting periodograms (Fig. 25) show the power spectra in frequency units of d^{-1} and present multiple strong peaks. These represent a combination of one or more true independent frequencies together with aliases due to the finite data sampling (Wall and Jenkins, 2003). The windowing of the data acquisition is of more relevance in the JHK_S bands because a more significant aliasing is produced by including only data taken through the SMARTS queue observing which has a strong one-day sampling frequency.

The amplitudes of the periodograms are normalized according to the formulation of Horne and Baliunas (1986) by the total variance of the data, yielding the appropriate statistical behavior which allows for the calculation of the false-alarm probability (FAP). The FAP presents the statistical significance of the periodogram by describing the probability that a peak of such height would occur from pure noise. To calculate FAPs for the most significant peaks in the periodogram, a Monte Carlo bootstrapping method (e.g., Stassun et al., 1999) was applied; it randomizes the differential magnitudes, keeping the Julian Dates fixed in order to preserve the statistical

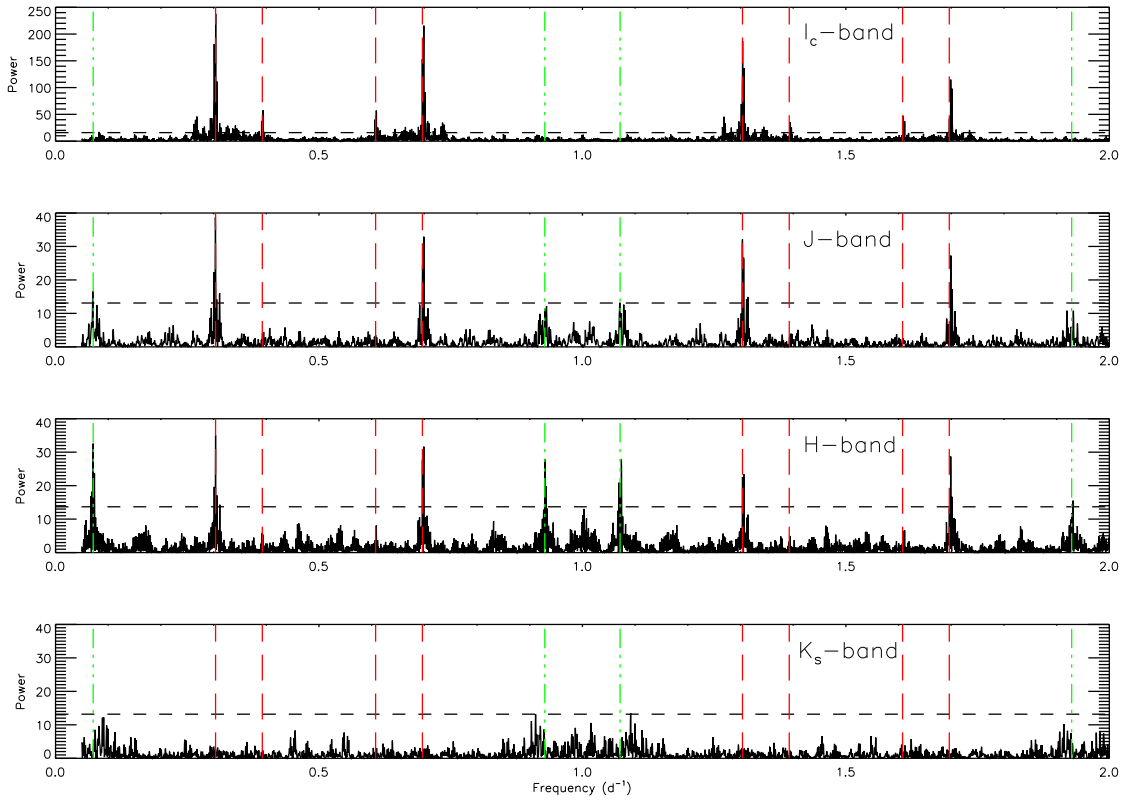

Figure 25: Lomb-Scargle Periodograms of 2M0535−05. The out-of-eclipse light curves were searched for periodicities using the Lomb-Scargle periodogram technique (Scargle, 1982) finding two independent signals with frequencies of ~ 0.30 and ~ 0.07 d^{-1} corresponding to periods of $P_{\rm rot,1} = 3.293 \pm 0.001$ and $P_{\rm rot,2} = 14.05 \pm 0.05$ d respectively. To assess the statistical significance of each of the predominant peaks in the power spectrum, the false-alarm probability (FAP) was calculated via a Monte Carlo bootstrapping method (e.g., Stassun et al., 1999). The horizontal, dashed line denotes the 0.1% FAP. The vertical, long-dashed lines correspond to $P_{\rm rot,1}$ and its corresponding aliases and beats; while the vertical, dot-dot-dot-dashed lines correspond to $P_{\rm rot,2}$ and its aliases and beats. The out-of-eclipse $I_C JH$ light curves folded over these two identified periods are shown in Fig. 26.

characteristics of the data. One thousand random combinations of the out-of-eclipse magnitudes were done with this procedure to obtain the FAP in each band. The resulting 0.1% FAP level is indicated in the periodograms by the dashed line in Fig. 25. Except for the K_S periodogram, multiple peaks are found well above the 0.1% FAP level and are therefore highly significant. The K_S measurements are much noisier than in the $I_C JH$ bands (Sec. VI.1), so the lack of significant periodicity in that light curve is not surprising and we do not consider the K_S light curve further in our periodicity analysis.

To distinguish the independent periods from their aliases, a sinusoid was fitted to each light curve and subtracted from the data in order to filter out the periodicity corresponding to the strongest peak in the periodograms. This peak in the $I_C JH$ bands is that which corresponds to the 3.293 $\pm$ 0.001 d period previously identified in SMV07, at a frequency of $\sim$0.30 d^{-1}. This period is not found in the K_S light curve owing to a larger scatter of the data in that bandpass (§VI.1.2). As expected, the subtraction of the 3.293-d periodic signal removed the strongest peak and also its aliases. The residual light curves were then reanalyzed to identify any additional periods.

This process revealed another independent frequency at $\sim$0.07 d^{-1} which corresponds to a period of 14.05 $\pm$ 0.05 d. This 14.05-d period also manifests itself as a three-peaked structure centered at 1 d^{-1} in the JH bands. The two exterior peaks of this structure have frequencies of 0.93 and 1.07 d^{-1}, corresponding to the beat frequencies between the 14.05-day period and a 1-day period. The 1-day period is most

likely due to the sampling of the observations, since the JH bands were observed roughly once per night. The I_C light curve does not show strong beats against a 1-day period because this band includes high-cadence data from many observing runs which disrupt the 1-day sampling period. The subsequent filtering of the 14.05-day period, as above, also removes its aliases and beats from the periodograms.

Figure 26 shows the out-of-eclipse light curves of 2M0535−05 phased on these two periods, together with best-fit sinusoids to guide the eye and to quantify the amplitudes of the variability as a function of wavelength. Regardless of the order of the filtering, these two independent periods were always obtained via this analysis. No other significant periods are found. We furthermore confirmed that these periods were not present in the light curves of the comparison star used for the differential photometry (§VI.1.2).

The uncertainty of the periods is given with a confidence interval of one sigma in the vicinity of the period peaks via the *post mortem* analysis described by Schwarzenberg-Czerny (1991). This method consists of determining the width of the periodogram's peak at the mean noise power level. The 3.293-d period has 1-σ uncertainties of 0.001 d, 0.003 d and 0.002 d for the I_C-, J- and H-bands respectively; while for the 14.05-d period the 1-σ levels are 0.1 d for the J-band and 0.05 d for the H-band.

Reiners et al. (2007) reported $v \sin i$ measurements of 2M0535−05 to be $\approx$ 10 km s^{-1} for the primary and $<$ 5 km s^{-1} (upper limit) for the secondary, i.e., the primary rotates at least twice as fast as the secondary. Moreover, these $v \sin i$ values, together with the radii from SMV07 and $\sin i \approx 1$, correspond to rotation periods of

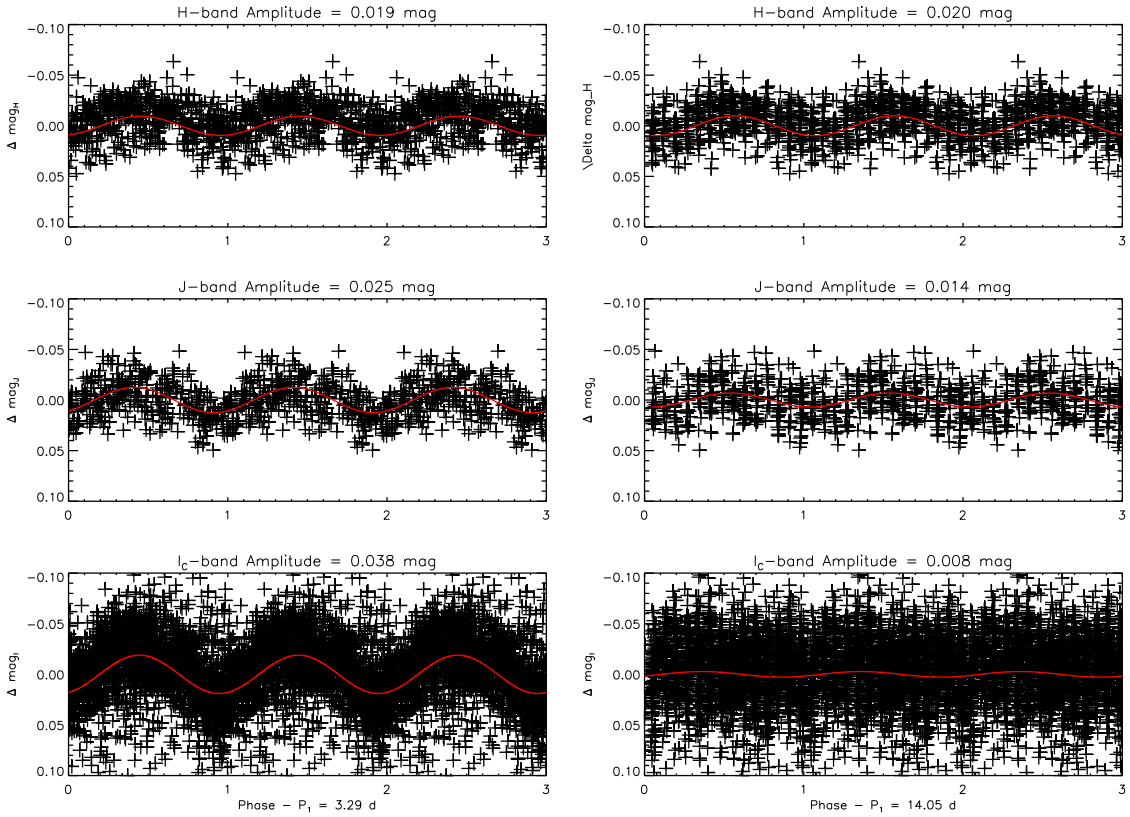

Figure 26: Out-of-Eclipse $I_C JH$-band Light Curves. The low-amplitude photometric variability is made evident by phasing the out-of-eclipse light curves to the two individual periods found from the periodogram analysis (see Fig. 25). The 3.293-d period attributed to the rotation of the more massive brown dwarf is used to phase the $I_C JH$ light curves shown in the left-column panels. The amplitude of this variation increases toward shorter wavelengths. The actual observations are repeated over each phase. The right-column panels are phased to the secondary's rotation period of 14.05 d; interestingly, its amplitudes decreases toward shorter wavelengths. Superimposed in each panel is a sinusoid fit representing the modulation due to the rotation of each component as described in §VI.3.

Table 9: Periodicities Detected by Season and Passband

Season[a]	$P_{\rm rot,1} = 3.29$ d		$P_{\rm rot,2} = 14.05$ d	
	I_C	JH	I_C	JH
I[b]	✓	✓	...	✓
II[b]	✓	✓	✓	✓
III	✓	✓	...	✓
IV	✓	✓	...	✓
V	✓	✓	✓	...

[a] See Table 8 for details of the observing campaigns.
[b] Only J or H were observed during this season.

$\approx 3.3 \pm 0.1$ d and > 6 d for the primary and secondary components, respectively. These are consistent with the periods of 3.293 ± 0.001 d and 14.05 ± 0.05 d that we have identified photometrically.

Table 9 summarizes the appearances of these two periods as a function of observing season and passband. The 3.29-d period is found consistently in nearly every season of observations in all three of the $I_C JH$ filters. We fit a sinusoid with a 3.29-d period separately to the data from each of the observing seasons and found that while the amplitude of the variability remained similar for each, the phase varied from season to season. Evidently, the 3.29-d period is caused by long-lived features that drift in longitude. The 14.05-d period is manifested less strongly in the data. While it is found in the JH light curves in most (but not all) seasons, it is detected in only two seasons of the I_C-band data.

Interestingly, while the 3.29-d period manifests an increasing amplitude of variability toward shorter wavelengths (Fig. 26, left panels), as is expected for spots

(either hot or cool; e.g., Bouvier et al., 1993), the amplitude of the 14.05-d periodicity *declines* toward shorter wavelengths. Maiti (2007) found a similar behavior in the optical variability of the field L dwarf 2MASSW J0036+1821, and suggested that the photometric variability in that object is therefore likely caused not by magnetic spots but rather by dust clouds formed near the surface (e.g., Zapatero Osorio et al., 2005). Perhaps the feature on the 2M0535−05 secondary that is responsible for the observed 14.05-d period is of similar origin. Indeed, this would be consistent with the findings of Reiners et al. (2007) that the 2M0535−05 secondary has a much weaker magnetic field compared to the primary, and thus may be less likely to produce strong magnetic spots.

In §VI.3 below, we include spots in our modeling of the 2M0535−05 light curves in order to demonstrate the effects that spots may have on the properties of the magnetically active primary. The true physical nature of the inhomogeneity on the magnetically inactive secondary does not affect that analysis. For our purposes we emphasize that the 14.05-d period is consistent with the secondary's measured $v \sin i$ and radius, and thus we can confidently ascribe that period to the rotation of the secondary.

VI.2.2 Orbital and Physical Parameters of 2M0535−05

Light-curve solution encompassing the multi-epoch, multi-band photometric data and radial-velocity measurements is calculated using the software `PHOEBE` (Prša and Zwitter, 2005) built on top of the 2007 version of the Wilson-Devinney algorithm

(WD; Wilson and Devinney 1971). A square root limb-darkening law was adopted, its coefficients linearly interpolated by `PHOEBE` from the van Hamme (1993) tables with each iteration. Emergent passband intensities are computed based on the passband transmission functions.

Table 10: Orbital and Physical Parameters of 2M0535−05

	RVs + I_C[a]			RVs + JHK_S + I_C		
Orbital period, $P_{\rm orb}$ (days)	9.779556 ± 0.000019					
Eccentricity, e	0.3276	±	0.0033	0.3216	±	0.0019
Orientation of periastron, ω ($^\circ$)	217.0	±	0.9	215.3	±	0.5
Semi-major axis, $a \sin i$ (AU)	0.0406	±	0.0010	0.0407	±	0.0008[b]
Inclination angle, i ($^\circ$)	89.2	±	0.2	88.49	±	0.06
Systemic velocity, v_γ (km s^{-1})	24.1	±	0.4	24.1	±	0.3[b]
Primary semi-amplitude, K_1 (km s^{-1})	18.49	±	0.67	18.61	±	0.55
Secondary semi-amplitude, K_2 (km s^{-1})	29.30	±	0.81	29.14	±	1.40
Mass ratio, $q \equiv M_2/M_1$	0.631	±	0.015	0.639	±	0.024[b]
Total mass, $M \sin^3 i$ ($M_\odot$)	0.0932	±	0.0073	0.0936	±	0.0051[b]
Primary mass, M_1 ($M_\odot$)	0.0572	±	0.0045	0.0572	±	0.0033
Secondary mass, M_2 ($M_\odot$)	0.0360	±	0.0028	0.0366	±	0.0022
Primary radius, R_1 ($R_\odot$)	0.675	±	0.023	0.690	±	0.011
Secondary radius, R_2 ($R_\odot$)	0.486	±	0.018	0.540	±	0.009
Primary gravity, log g_1	3.54	±	0.09	3.52	±	0.03
Secondary gravity, log g_2	3.62	±	0.10	3.54	±	0.03
Primary surface potential, Ω_1		...		13.63	±	0.18
Secondary surface potential, Ω_2		...		12.00	±	0.16
Primary synchronicity parameter, F_1		...		2.9725	±	0.0009
Secondary synchronicity parameter, F_2		...		0.6985	±	0.0025
Effective temperature ratio, $T_{\rm eff,2}/T_{\rm eff,1}$	1.064	±	0.004	1.0495	±	$^{0.0039}_{0.0038}$

[a] Previously published results (SMV07).

[b] The uncertainties in these parameters were conservatively estimated from the formal errors of a fit to the RV data alone. See §VI.2.2.

The simultaneous fit of the radial velocities and the $I_C JHK_S$ light curves was done using the published results from SMV07 as initial parameters for the modeling. The first column of Table 10 lists these starting values. The solution was then iterated. Since we do not have reliable errors on the individual JHK_S measurements (see §VI.1.2), the individual data points were assigned equal weight and then the overall weight of each light curves was set to the inverse-square of the r.m.s. of the residuals relative to the fit from the previous iteration. The primary's temperature is taken to be $T_{\rm eff,1} = 2715 \pm 200$ K, where the uncertainty is dominated by the systematic uncertainty of the spectral-type–$T_{\rm eff}$ scale (SMV07). We emphasize that the uncertainty on the individual component temperatures does not represent the high accuracy with which the quantities directly involved in the light curve fitting are determined, namely the ratio of the temperatures. In addition to setting $T_{\rm eff,1}$ to a fixed value, the orbital period $P_{\rm orb}$ was also kept constant. The synchronicity parameters are obtained from the rotation periods (§VI.2.1) such that $F_1 = \omega_{\rm rot,1}/\omega_{\rm orbital} = 2.9725 \pm 0.0009$ and $F_2 = \omega_{\rm rot,2}/\omega_{\rm orbital} = 0.6985 \pm 0.0025$. The free parameters to be obtained from the modeling were: the inclination angle i, the semi-major axis a, the orbital eccentricity e, the argument of the periastron ω, the systemic radial velocity v_γ, the mass ratio q and the secondary's surface temperature $T_{\rm eff,2}$, through the determination of the temperature ratio $T_{\rm eff,2}/T_{\rm eff,1}$. Because the primary's radius is small compared to the semi-major axis ($R_1/a = 0.08$), reflection effects are assumed to be negligible (reflection effects generally only become important for $R_1/a \gtrsim 15\%$; e.g., Wilson, 1990).

A direct output of the Wilson-Devinney algorithm that underlies PHOEBE is the formal statistical errors associated with each of the fit parameters, as well as a correlation matrix that provides insight into the often complex interdependencies of the parameters. In order to explore these parameter correlations and solution degeneracies more carefully, and to thus determine more robust parameter uncertainties, we performed a thorough Monte Carlo sampling of the parameter hyperspace using the PHOEBE code's scripting capability. An examination of the parameter correlation matrix revealed that there are two particularly strong parameter degeneracies in our dataset: (1) between the inclination, i, and the surface potentials, Ω; and (2) between the temperature ratio, $T_{\rm eff,2}/T_{\rm eff,1}$, and the radius ratio, R_2/R_1.

Figure 27 shows the resulting joint confidence interval for i and Ω_1 given by the variation of χ^2 with these two parameters around the solution's minimum. The shaded contours correspond to confidence intervals following a χ^2 distribution with two degrees of freedom, with the first contour at the 1-σ confidence level and each subsequent level corresponding to an increment of 1 σ. The i–Ω_1 cross section was sampled by randomly selecting a value for i between 87° and 90°, and one for Ω_1 between 12.0 and 14.5, rendering a more complete coverage of the parameter hyperspace. We marginalized over the remaining system parameters, notably the strongly correlated Ω_2. This analysis yields uncertainties around the best-fit values of: $i = 88.49^{+0.03}_{-0.06}$ degrees and $\Omega_1 = 13.63 \pm 0.18$, the latter corresponding to a primary radius of $R_1 = 0.691^{+0.009}_{-0.010}$ $R_\odot$. The secondary's best-fit radius and its uncertainties follow directly through the ratio of the radii (discussed in the next paragraph).

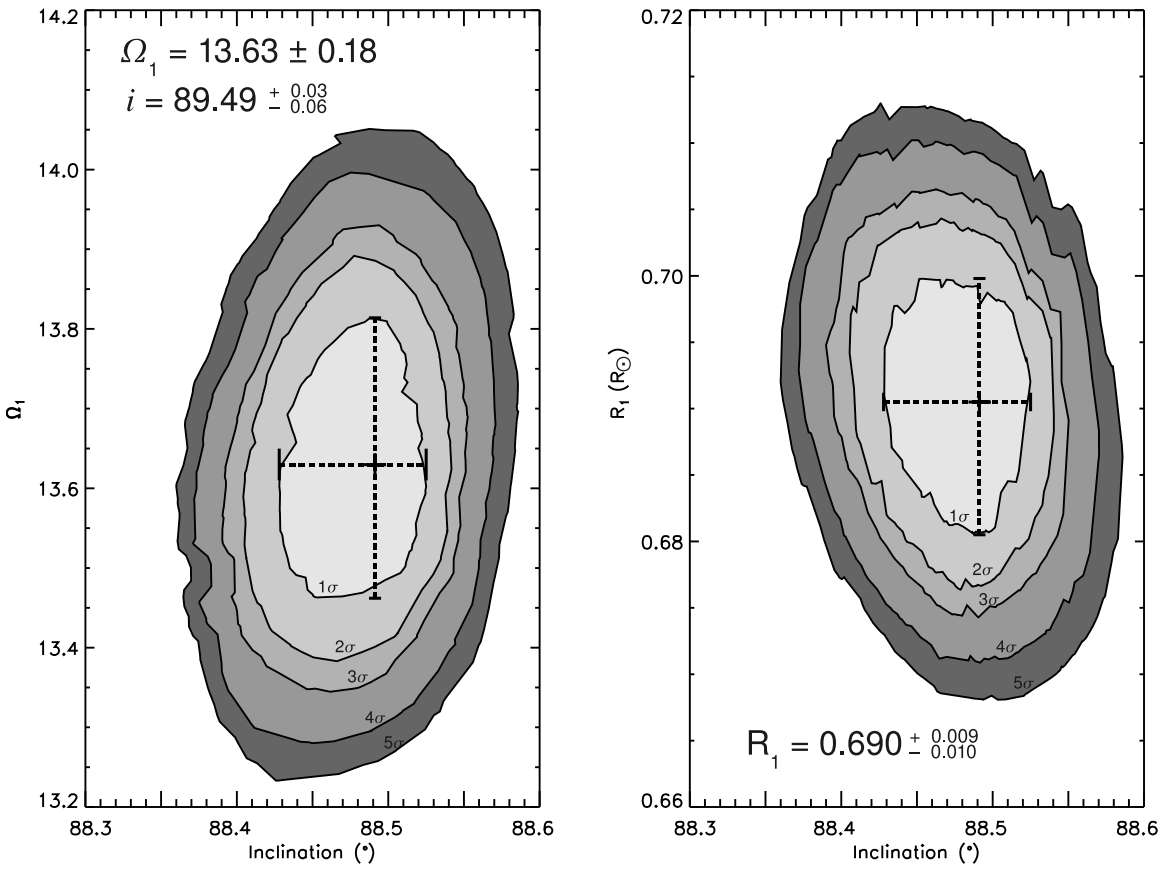

Figure 27: Joint Confidence Interval between the Inclination Angle i and the Primary Surface Potential Ω_1. The Monte Carlo sampling of this cross section allows for the heuristic errors associated with the available data to be estimated given by the variation of χ^2 with i and Ω_1 (§VI.2.2). Because of the intrinsic degeneracy of the binary problem and the data's uncertainties, closely correlated parameters must be explored to ensure that the system's solution falls within the global minimum of the cost function. The cross represents the point at which the χ^2 of the fit attains its minimum value and shows the 1-σ uncertainties for each of the parameters given by the smallest contour. Each subsequent contour symbolizes an increase of 1 σ. The right panel shows the same sampling of the $i-\Omega_1$ cross section in terms of the primary radius.

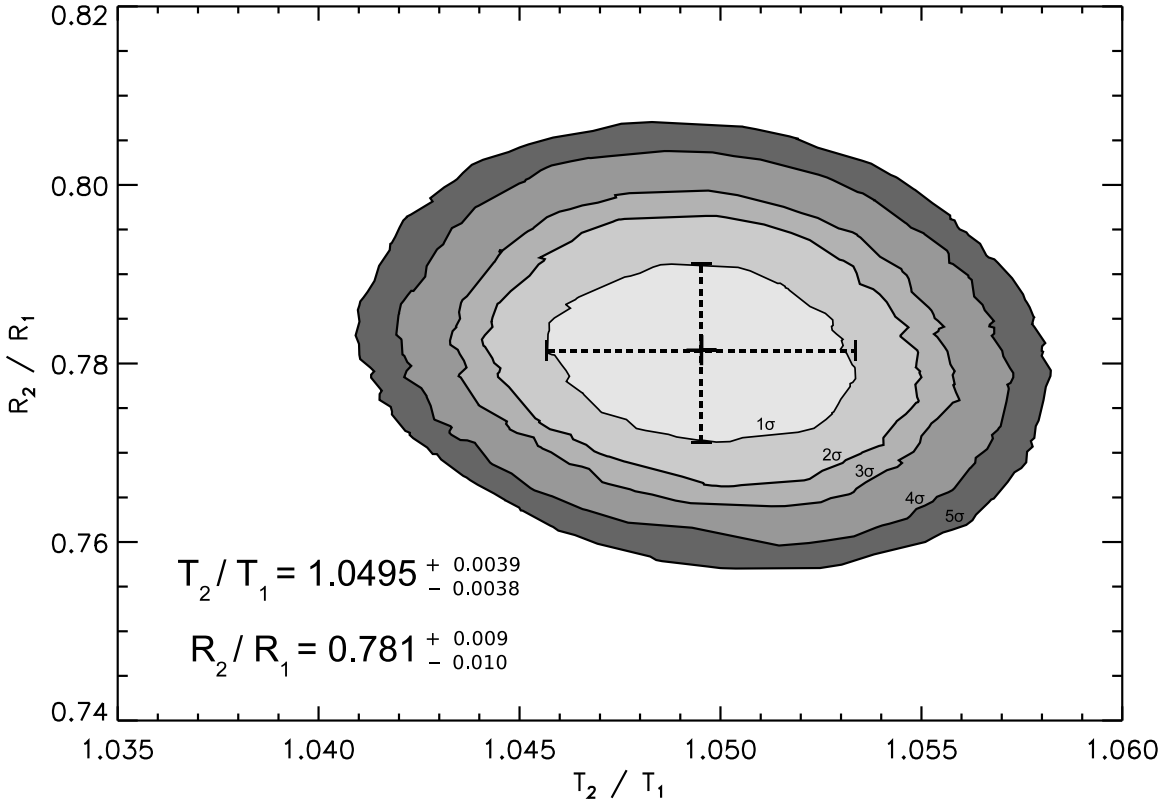

Figure 28: Joint Confidence Interval between $(T_{\rm eff,2}/T_{\rm eff,1})$ and (R_2/R_1). This parameter hyperspace is of particular interest in the case of 2M0535−05 because of the apparent temperature reversal it presents. Similar to Fig. 27, the cross represents the point at which the χ^2 of the fit attains its minimimum value and shows the 1-σ uncertainties for each of the parameters given by the smallest contour. Each subsequent contour symbolizes an increase of 1 σ.

The $(T_{\rm eff_2}/T_{\rm eff,1})$–$(R_2/R_1)$ plane, shown in Fig. 28, is of particular interest because of the apparent temperature reversal that 2M0535−05 presents. This parameter cross section was explored keeping the $T_{\rm eff}$ of the primary fixed at 2715 K while varying the $T_{\rm eff}$ of the secondary between 2700 and 2925 K. The primary radius was varied randomly between 0.635 and 0.758 $R_\odot$, while minimizing for the secondary radius. The resulting uncertainties about the best-fit values are: $T_{\rm eff,2}/T_{\rm eff,1} = 1.0495^{+0.0039}_{-0.0038}$ and $R_2/R_1 = 0.781^{+0.009}_{-0.010}$. Note that these errors determined from our Monte Carlo sampling procedure are larger than the formal statistical errors by ∼50%.

Finally, we separately performed a fit of the radial velocity data alone for the orbital parameters that most directly determine the masses, namely: $a\ sin\ i$, q, and v_γ in order to more carefully estimate the uncertainties in these parameters.These orbital parameters should not depend on the light curves; however we found that purely statistical correlations between these parameters and other system parameters tended to drive down the formal errors in the masses to unrealistically small values. We include e, ω, and the time of periastron in the fit, but for these parameters we deferred error estimates to the simultaneous fit to the radial velocity and light curve data. Therefore we adopted the uncertainties in $a\ sin\ i$, q, and v_γ from the radial velocity fit, the uncertainties in i, Ω_1, Ω_2, and T_2/T_1 from the Monte Carlo sampling, and the uncertainties of other parameters from the simultaneous fit to the radial velocity and light curve data. We then propagated these uncertainties into the final errors of the parameters that depend on these quantities, such as the masses and radii.

The final parameters for 2M0535−05 resulting from our joint analysis of the radial velocities and $I_C JHK_S$ light curves, and with uncertainties determined as described above, are summarized in the last column of Table 10. The results are in agreement with those previously published, although the uncertainties in many parameters have now improved compared to those reported in SMV07. For example, the uncertainties in the component masses has decreased from ∼10% to ∼6.5%, and in the radii from ∼ 5% to ∼1.5%. This improvement arises primarily because of the improved determination of e and ω through the addition of the JHK_S light curves, thus improving the determination of the time of periastron passage.

As in the previous analyses of 2M0535−05 (SMV06, SMV07), we find again a reversal of effective temperatures from what would be expected from the observed mass ratio (i.e., the higher mass primary is cooler than the secondary) at high statistical significance. This surprising result is now confirmed on the basis of a full analysis including radial velocities and four light curves ($I_C JHK_S$) together.

VI.3 Surface Spots

In §VI.2.1 we found clear evidence of two separate low-amplitude variations in the light curves of 2M0535−05 with periods of 3.29 d and 14.05 d. PMS objects are typically found to be photometrically variable (e.g., Bouvier et al., 1993; Carpenter et al., 2001), and this variability is in almost all cases attributable to the presence of magnetic "spots" (akin to sunspots), to accretion from a circumstellar disk, or both. However 2M0535−05 has been shown to not possess circumstellar or circumbinary

material and thus is not currently accreting (Mohanty et al., 2009). Pulsations have been suggested in a few brown dwarfs, but are expected to have characteristic periods of only a few hours (Palla and Baraffe, 2005).

In this section we explore the effects of surface spots on the light curves for the purpose of explaining the periodic variations found in §VI.2.1, and to assess whether such spots might be able to explain the surprising reversal of effective temperatures in the system (§VI.2.2).

We begin by determining the properties of spots on the primary required to reproduce the low-amplitude, periodic variability observed in the light curves. The primary's variability amplitudes were measured by fitting a sum of two sinusoids to the out-of-eclipse data in each of the $I_C JH$ bands, one sinusoid corresponding to the rotation period of the primary at 3.293 d and another for the secondary at 14.05 d (Fig. 26). The amplitudes of the 3.29-d signal were then scaled up by the components' relative luminosities, since the observed amplitudes are diluted by the light from the secondary.

These amplitudes were fit using an analytic model based on a two-component blackbody as described by Bouvier et al. (1993). The free parameters are the spot temperature relative to the photosphere and the spot areal coverage. The areal coverage parameter is an "effective" area, i.e., it is really a measure of the ratio in spot coverage between the least and most spotted faces of the surface and is thus a measure of the degree of spot asymmetry. The results of this first-order analysis of the spot parameters are shown in Fig. 29. A family of solutions is found, such that a

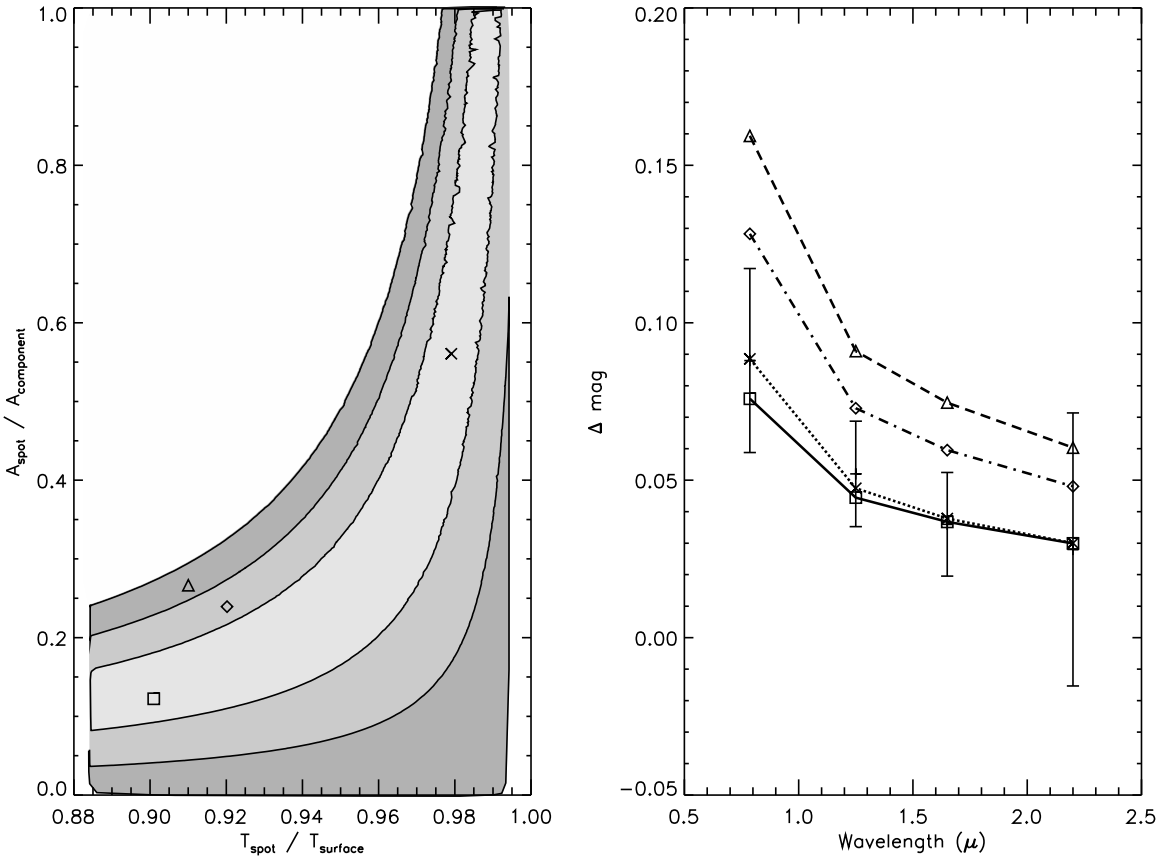

Figure 29: Modeling of the Wavelength-Dependent Photometric Variability Using an Analytical Inversion Technique. Using this technique, based on a two-component blackbody radiation (Bouvier et al., 1993), to fit the measured low-amplitude photometric variability of 2M0535−05's light curves, we can estimate the spot temperature relative to the photosphere and the effective areal coverage of the spots. Because of the inherent degeneracy of spot modeling, a change in the temperature ratio maybe counteracted with an appropriate change in the areal coverage; the inversion technique renders not a single spot configuration but a family of solutions that describe the observed variability. In the left-hand panel, the central region of the contours corresponds to those solutions for which the analytical amplitudes (Δ mag) fall within the 1-σ photometric uncertainties of all of the observed bands. The second level of contours represents the solutions that fall within the 2-σ photometric uncertainties and the third those that fall within the 3-σ uncertainties. The right-hand panel shows the observed amplitudes of the photometric variation at the different wavelengths with 1-σ error bars; for comparison the modeled amplitudes corresponding to the spot parameters marked by the four points in the left-hand panel are overplotted. The cross-point and the dotted line correspond to the fit with lowest χ^2; the square-point and the continuous line are representative of the parameters chosen for the treatment of spots in the subsequent light curve modeling; the diamond-point and the dot-dash line denote a point on the second level contours, and the triangle-point and the dashed line correspond to a solution on the third contour level.

change in the spot temperature factor may be counterbalanced by a change in the areal coverage. As one example, the observed light-curve variations can be fit with a spot that is $\sim$ 10% cooler than the photosphere and that has an effective areal coverage of $\sim$ 10%. For the purposes of our modeling, and for simplicity, we placed a small cool spot with this temperature and area at the equator of the primary and allowed `PHOEBE` to adjust the spot's longitude to match the phasing of the observed variations (Fig. 26). We emphasize that the spot parameters are degenerate and we do not claim that the adopted parameters are accurate in an absolute sense. Rather, they should be taken as representative of the asymmetric component of the primary's spot distribution that causes the observed low-amplitude variability modulated on the primary's 3.29-d rotation period (Fig. 26).

We ran a new light curve solution with `PHOEBE`, this time including the small spot on the primary as above, in order to check the influence of the spot specifically on the derived temperature ratio. The best-fit system parameters are changed insignificantly. The temperature ratio in particular is changed from the value in Table 10 by less than 1σ. This is not surprising given the small areal coverage and temperature contrast of the spot and considering that in SMV07 we obtained a nearly identical temperature ratio with a purely spotless model. The inclusion of a small spot on the primary as required to fit the observed low-amplitude variability is by itself not sufficient to explain the observed temperature reversal in the system.

As a next test, we added a large cool spot at the pole of the primary in addition to the small cool spot. Assuming that the rotational and orbital axes of the system are

parallel, and since $i \approx 90°$, the effective areal coverage of a polar spot will not change with rotational phase as seen by the observer. Thus this polar spot represents the *symmetric* component of the primary's spot distribution that, if it covers a sufficiently large area, may cause an overall suppression of the primary's effective temperature without producing additional variations with rotational phase[1]. The evolutionary models of Baraffe et al. (1998) predict an effective temperature of 2880 K for a brown dwarf with the mass of the 2M0535−05 primary at an age of 1 Myr, so we set the photospheric temperature of the primary to this value and re-fit the light curves with `PHOEBE`, this time including both a small equatorial spot as before together with a large polar spot as described above, both with temperatures 10% cooler than the photosphere. The areal coverages of the two spots were left as free parameters, and attained best-fit values of 8% and 65%, respectively.

Finally, we added a small equatorial spot on the secondary, again with a temperature 10% cooler than the photosphere, representing the surface inhomogeneity that produces the observed variations modulated on the secondary's 14.05-d rotation period (Fig. 26). Using `PHOEBE` we performed a final simultaneous fit for the sizes of the spots on both the primary and secondary. The final best-fit spot areal coverage factors for the smal spot on the primary, the small spot on the secondary, and the large spot on the primary were 7%, 3%, and 65%, respectively.

In reality, the observed variability of the magnetically inactive secondary is not

[1]In fact, even a polar spot will cause a small variation *during eclipse*, however this effect is $\sim 0.05\%$ in the $I_C JHK_S$ bands for the adopted spot parameters, and is thus below the threshold of detectability given our photometric precision of $\sim 1\%$.

likely to be caused by a magnetic spot, because the secondary is less active, it is rotating slower than the primary, and the amplitude of its variability does not decrease with increasing wavelength as expected for magnetic spots. So perhaps, the observed variability is more likely due to dust in its atmosphere (§VI.2.1). Our light-curve modeling code does not currently incorporate a physical treatment of such dust features, and thus we use the spot modeling capability as a surrogate. In addition, we found that there is a near-total degeneracy between the sizes of the small spots on the primary and secondary if their temperatures are left as free parameters. That is, in the same way that the temperature and size of an individual spot are degenerate (see Fig. 29), the sizes of the two spots relative to one another are degenerate unless their temperatures are fixed. Thus we have taken the simplifying approach of fixing the spot temperatures to be 10% cooler than the surrounding photosphere on both the primary and secondary. The spot sizes are then constrained by the observed variability amplitudes (Fig. 26). Similarly, we have chosen not to include a large polar spot on the secondary as we have on the primary. The spot areas that we quote above are the formal best-fit values, however we caution that the properties we have determined for the inhomogeneity on the secondary should be taken as qualitative. More important for our analysis here, the properties of the spots on the magnetically active primary are minimally affected by the presence of the low-amplitude variability from the secondary, regardless of its true nature.

Finally, we have not included a polar spot on the secondary, although from the standpoint of the light curve modeling alone it is possible to achieve equivalent

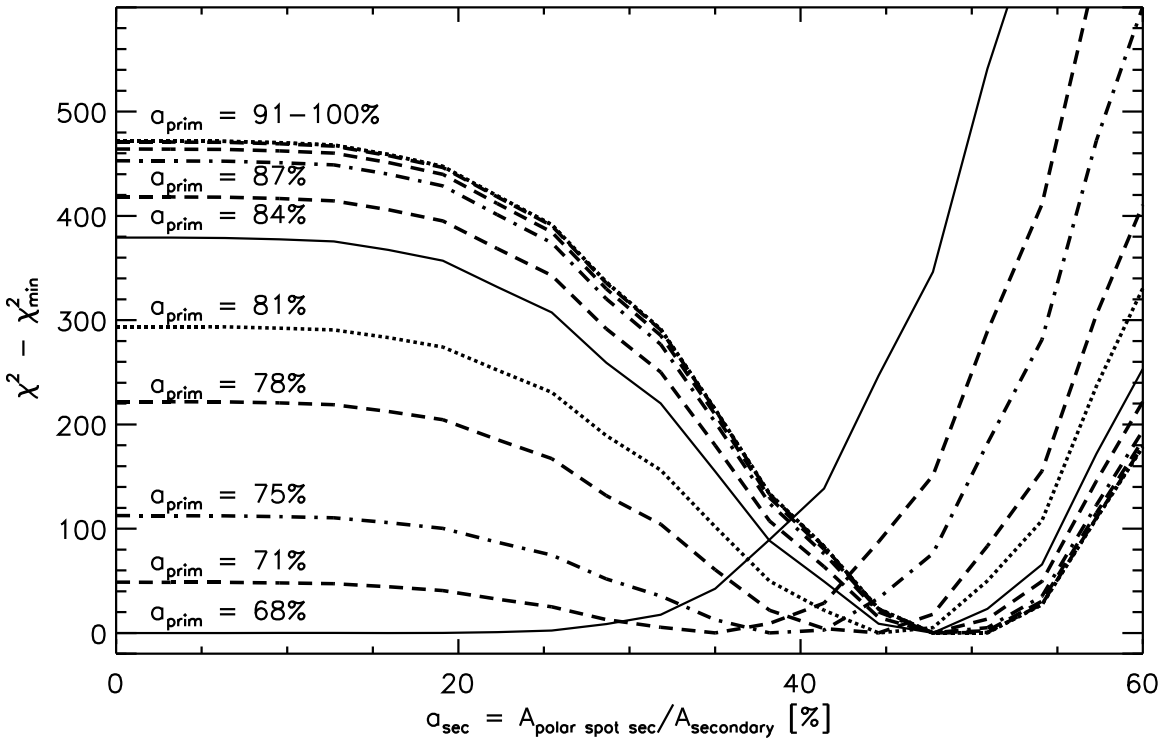

Figure 30: Degeneracy Between Large Polar Spots on the Primary and the Secondary Components of 2M0535−05. This figure shows the χ^2 convergence of the light curve fitting of 2M0535−05 when large polar spots are included on both of the components, with the temperatures of the components fixed at the values predicted by the theoretical evolutionary models of Baraffe et al. (1998). If a polar spot is included only on the primary, its areal coverage is required to be 5% (see §VI.3). If a polar spot is also included on the secondary, the areal coverage of the primary's polar spot must be increased to maintain the required temperature ratio of the components. All of the solutions shown in the figure are equivalent in terms of χ^2 and thus produce equally good fits to the data.

goodness-of-fit with polar spots on both components if their relative areal coverages are adjusted so as to preserve the adopted photospheric temperature ratio (see Fig. 30). We have taken the simplifying approach of including a polar spot on the primary only because (1) the evidence suggests that the primary is the more magnetically active of the two components (Reiners et al., 2007), (2) the secondary's temperature is already in good agreement with the predictions of theoretical models (SMV07) and thus does not need to be suppressed by a large spot, and (3) as discussed above, the secondary's variability amplitudes do not indicate that it possesses magnetic spots.

Figure 31 presents a comparison of the spotted and unspotted light curve models for the I_C band, the band in which the spot effects are most pronounced. The synthetic light curves shown have been calculated over a single orbital period. In view of the fact that the components do not rotate synchronously with one another or with the orbital period, the effects of the spots on the light curves (such as the dip in the model at a phase of $\sim$0.4) will shift in orbital phase from one orbit to the next, and thus these variations are averaged out in the observed light curve which is phased over many orbital periods. We furthermore verified that the effects of the spots on the radial velocities are negligible and thus do not affect any of the system's physical parameters that are determined kinematically (e.g., the masses).

The primary conclusion to be drawn from the above is that the light curves of 2M0535$-$05 can be well modeled by having the primary component's photospheric temperature at the theoretically expected value if $\sim$ 65% of its surface is covered

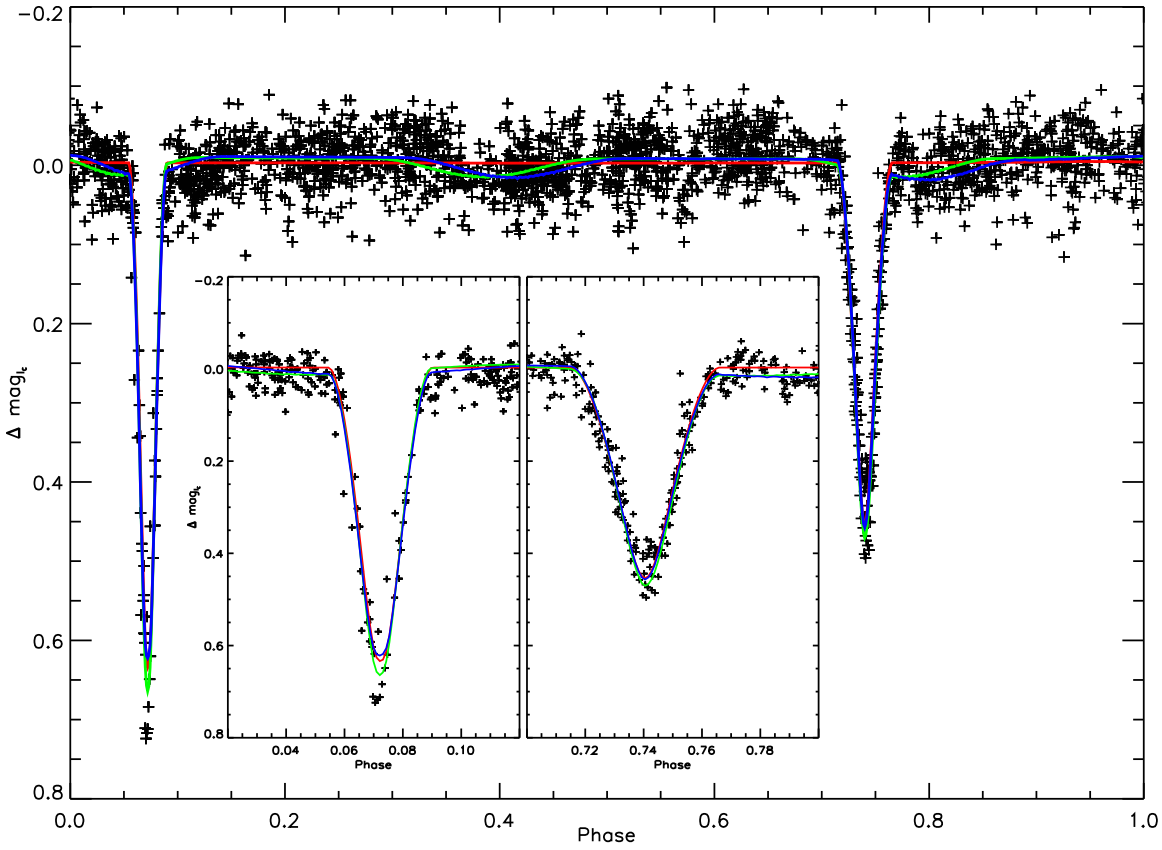

Figure 31: Light Curve Modeling Including Treatment of Spots. The observed I_C light curve is plotted superimposed with three different synthetic models each corresponding to a single orbital period starting at the time of periastron: the red curve represents the spotless model; the green curve is for the model where only the primary brown dwarf is spotted, and the blue curve describes one in which both components have spots. Both spotted models are proposed to have spots that are 10% cooler than the surrounding photosphere and have an asymmetric constituent that describes the low-amplitude photometric variability, by the use of a small, equatorial spot on one or both of the components, and a symmetric constituent in order to reconcile the more massive brown dwarf's effective temperature with that expected from the evolutionary models (e.g., D'Antona and Mazzitelli, 1997), described by polar spots with a large areal coverage. The green model, with spots only on the primary, has an equatorial spot that covers 10% of the surface (See Fig. 29), and a polar spot with an areal coverage of 65%. In the case where both components have spots (blue curve), the low amplitude variability is described by an equatorial spot on the primary that covers 7% of its surface and another on the secondary with an areal coverage of 3%. Note that the non-synchronicity of the rotation with the orbital period causes the effect of the spots on the light curve to change in phase over time, rendering them noncoherent in the phase-folded data.

with cool spots in a roughly symmetric distribution. The small spot in our model represents the $\sim 10\%$ asymmetry in the spot distribution that produces the observed low-amplitude periodic variations.

VI.4 Discussion

In order to simultaneously explain the observed low-amplitude variations and the anomalously low effective temperature of the primary (more massive) component in 2M0535−05, we have produced a model that includes a simple spot configuration of a small equatorial spot together with a very large polar spot. The former represents the asymmetric component of the spot distribution that produces the low-amplitude variations modulated on the primary's rotation period, while the latter represents the symmetric component of the spot distribution that causes an overall suppression of the effective temperature below its theoretically predicted value. In this model, the unspotted regions of the primary's surface have the theoretically predicted value of 2880 K (Baraffe et al., 1998).

The true distribution of spots on the primary's surface is probably more complex. For example, a more realistic spot configuration might be one that resembles Jupiter's bands. In that case, a symmetric equatorial band with a temperature 10% cooler than the photosphere and extending 40° above and below the equator would reproduce similarly the effect of the polar spot. The same result could be obtained by a leopard-print pattern as that described by Linnell (1991) with an equivalent areal coverage and equal spot temperature factor as the polar spot we modeled. Either of these

might describe more accurately a physical configuration of spots for the primary. Without direct Doppler imaging of 2M0535−05, it is not possible to more accurately pinpoint the true spot properties.

We emphasize that there is nothing in our treatment of spots that prefers the primary's effective temperature to be 2880 K as dictated by the evolutionary models. We could have chosen any other effective temperature for the photosphere surrounding the spots and achieved an equally good fit of the light curves by adjusting the spot temperature and/or areal coverage to compensate. Thus our adoption of a primary effective temperature of 2880 K in the light curve solution of Fig. 31 should not be interpreted as a verification of the theoretical models. In addition, it should be noted that in our model the *overall* surface brightnesses of the components (integrating over both spotted and unspotted surface regions) are unchanged, such that the primary's overall effective temperature is still lower than that of the secondary. This is an unavoidable consequence of the observed eclipse depths, which ultimately require the secondary to be *effectively* hotter than the primary. The luminosities of the brown dwarfs thus also remain the same regardless of the chosen effective temperature and corresponding spot configuration, because the overall surface brightnesses and radii are unaltered by our spot treatment.

Moreover, our modeling of spots treats only the radiative behavior of the surfaces of the brown dwarfs, not their underlying structure. Consequently our modeling does not serve as a detailed test of any structural or evolutionary effects caused by the surface magnetism that is likely responsible for the spots that we have modeled.

For example, Chabrier et al. (2007) have proposed that the temperature reversal in 2M0535−05 could be explained by a magnetically active primary with a spot covering fraction of 50% together with surface convection that has been magnetically suppressed to a very low $\alpha = 0.5$ (as opposed to the usual $\alpha \approx 1$–2; e.g., Stassun et al., 2004). They also suggest that suppressed convection may explain why the measured radius of the primary is $\sim 10\%$ larger than predicted by their theoretical mass-radius relationship. Their exploratory treatment assumes "black" (i.e., 0 K) spots, whereas our modeled spots have a more physically realistic temperature 10% cooler than the photosphere, so the total spot-covering fraction of $\sim 75\%$ that we find for the primary (large polar spot plus small equatorial spot) may in fact be consistent with the $\sim 50\%$ coverage adopted by Chabrier et al. (2007). In addition, we have empirically determined the radii of 2M0535−05 with an accuracy of $\sim 1\%$, however our light curve modeling cannot confirm whether the radii have been altered in some way by the presence of spots or by magnetically suppressed convection.

CHAPTER VII

CONCLUSIONS

VII.1 Summmary

Parenago 1802 and 2M0535−05 are two of only six known pre-main sequence eclipsing binary systems where both components have masses below 1.5 $M_{\odot}$. Par 1802, recently discovered to be a double-lined, detached eclipsing binary, is the youngest example of a low-mass system with a mass ratio of almost unity. 2M0535−05 is the first known eclipsing binary in which both components are brown dwarfs. Their eclipsing nature allows for precise direct measurements of the components' masses and radii, and are therefore of paramount importance for providing observational constraints against which theoretical early-age evolutionary models of low-mass stars and brown dwarfs are compared. This is the first multi-band analysis which better constrains the radii of the eclipsing components. The masses of the eclipsing components of Par 1802 have been determined within an uncertainty of $\sim 8\%$ and their radii within $\sim 6\%$. The masses of the components of 2M0535−05 previously reported to have uncertainties of $\sim$10% (SMV07) have been here determined with an accuracy of $\sim$6.5%, and the radii with an accuracy of $\sim$1.5%. Our multi-band analysis permits a detailed modeling of magnetic spots on 2M0535−05's brown dwarfs that may be altering their surface properties, and of a third light source in the case of Par 1802.

Through a detailed analysis of the variability observed in the light curves out of

eclipse, we are able to identify the rotation periods of the components in both systems. The measured rotation periods are consistent with the radii and the spectroscopically measured values of $v \sin i$. In the case of Par 1802, the components are rotating quasi-synchronously with a period that is close to but significantly different from the orbital period of the binary. The components have almost synchronized their rotation to the orbital motion; however, because of Par 1802's young age, its orbit has not had time to circularize, presenting a very small, but significant eccentricity. This represents one of the shortest period PMS binaries for which the eccentricity has been measured to be different than zero (e.g., Melo et al., 2001). The rotation periods of the brown dwarf components of 2M0535−05 are measured to be $P_{\rm rot,1} = 3.293$ d and $P_{\rm rot,2} = 14.05$ d. Thus the brown dwarfs rotate non-synchronously relative to their orbital motion, perhaps due to the youth of the system ($\sim$ 1 Myr; Stassun et al., 2006, 2007). They also rotate asynchronously relative to one another, with the more massive brown dwarf rotating faster. These characteristics of the rotation and the orbital motion provide important observational constraints for the theory of tidal interactions at very young ages that lead to the synchronization and circularization of low-mass binaries.

In both cases, we find unanticipated results when studying these eclipsing systems in detail. Theoretical evolutionary models predict for stars of the same mass, composition and age. We find that for masses that are equal within 3%, the radii of the eclipsing components of Par 1802 differ by 7% and their effective temperatures by 9%. This result challenges the current understanding of the formation and evolution

of *twin* stars, like how strictly coevality of binary components should be considered. A lag of 300 000 years in the formation of the primary component is able to reproduce the difference in radii and effective temperatures between the components of Par 1802 (Cargile, 2010). 2M0535−05 is established to have substellar binary components, and shows a surprising reversal of temperatures in which the primary (more massive) brown dwarf appears cooler than the secondary. Since binary formation predicts that the components of a system will be formed from the same collapsing cloud, the components should thus have the same composition and age. Though this prediction is challenged by Par 1802's results. Therefore, equal-mass components of a binary are predicted to have the same effective temperature and radii; and the more massive of the components in an unequal mass binary is anticipated to be hotter than its less massive companion.

The characteristics of these pre-main sequence systems shed light into the complexity of the processes involved in star formation and early evolution. Both systems present different modeling challenges. In order to explain the observed data, we proposed that Par 1802 has a faint, unresolved, third component that is rapidly rotating. The presence of this fast stellar rotator in the system explains the short-period photometric variability observed in all light curves and the excess continuum found in Par 1802's spectra. It also provides the third light source that is required for the multi-band light curve modeling. The addition of third light in the modeling affects particularly the system's inclination angle, and therefore the system parameters that depend on it. However, the dynamically deduced properties of Par 1802, like the

mass ratio, remain unaffected.

In order to reconcile the observed effective temperatures of the components of 2M0535−05 with those predicted by theoretical models, the primary brown dwarf must be heavily spotted. Through the detailed spectroscopic and photometric modeling of 2M0535−05, including the treatment of spots, we are able to reproduce the apparent reversal of the temperature ratio. This 'spottedness' must be more or less symmetric to agree with the low-amplitude variability observed in the light curves, and it must have large effective areal coverage. Thus we modeled a two-spot configuration on the primary's surface: a large polar spot with an areal coverage of ∼65% to account for the lower-than-expected surface brightness, and an equatorial spot covering ∼10% of the surface for the purpose of introducing the asymmetry responsible for the observed low-amplitude photometric variability modulated on the rotation period. With this configuration, we are able to successfully reproduce the observed light curves with the primary having an effective temperature at the theoretically predicted value. Other geometries for the spot configuration—such as an equatorial band akin to those on Jupiter—would achieve the same effect. To be clear, from the standpoint of the light-curve modeling alone there is no need for a large spot-covering fraction on either brown dwarf. A small areal coverage of ∼10% is sufficient to model the low-amplitude variations that we observe in the light curves. Our aim here has been to demonstrate as proof of concept that the spots on the primary are capable of explaining its suppressed effective temperature in a manner that is consistent both with recent empirical findings of enhanced activity on the primary (Reiners et al.,

2007) and recent theoretical results on the effects of such activity on the physical properties of young brown dwarfs (Chabrier et al., 2007; MacDonald and Mullan, 2009).

The departure of the two systems' parameters from the expected trends may be the result of one or more physical phenomena affecting these young low-mass stellar and substellar objects that may not be well modeled. For example, evolutionary models have typically not included the effects of magnetic fields because of the complexity and difficulty involved in their modeling. Magnetic activity, as mentioned above, may be the cause of the highly spotted surface and thus the apparent temperature reversal of 2M0535−05. However, magnetic activity is unlikely to be causing the disparate radii and temperature reversal found between the twin components of Par 1802. Par 1802's nearly equal-mass components are found to be rotating at the same rate making it improbable that the components have different magnetic activity levels. Furthermore, increased magnetic activity reduces the convective efficiency of the star, thus lowering the effective temperature and increasing the radius in order to maintain the star's luminosity (Chabrier et al., 2007). If magnetic activity were the cause of the discrepant radii and effective temperatures we observe in Par 1802, we would expect the cooler eclipsing component to have the larger radius. We find however that the eclipsing component of Par 1802 with the lower effective temperature is also the smaller star.

The dissimilar radii and temperatures, and thus luminosities of the components of Par 1802 has been proposed to be due to a difference in age (SMC08; Cargile, 2010).

Figure 32 shows the how a change in a few thousand years can explain the differences in the physical parameters of the twin stellar components. The only theoretical models that show a fast evolution at young ages and that would allow for the differences presented by the eclipsing components of Par 1802 are those by D'Antona and Mazzitelli (1997). However, this evolutionary model approximates low-mass stars and brown dwarfs as having grey atmospheres. For effective temperatures below 4 000 K, the presence of molecules in the atmospheres causes the models to overestimate the effective temperatures for a given mass (Chabrier and Baraffe, 2000). The evolutionary tracks by Baraffe et al. (1998) use a treatment of the atmospheres with model NextGen atmospheres instead of the grey approximation. Baraffe et al. (1998) predict that the surface temperature of the components of Par 1802 will not change significantly with age; they get hotter by $\sim$ 200 K over 100 Myrs (Cargile, 2010). However, they do not model ages younger than 1 Myr, which precludes our making a direct comparison with the models by D'Antona and Mazzitelli (1997) shown in Fig. 32.

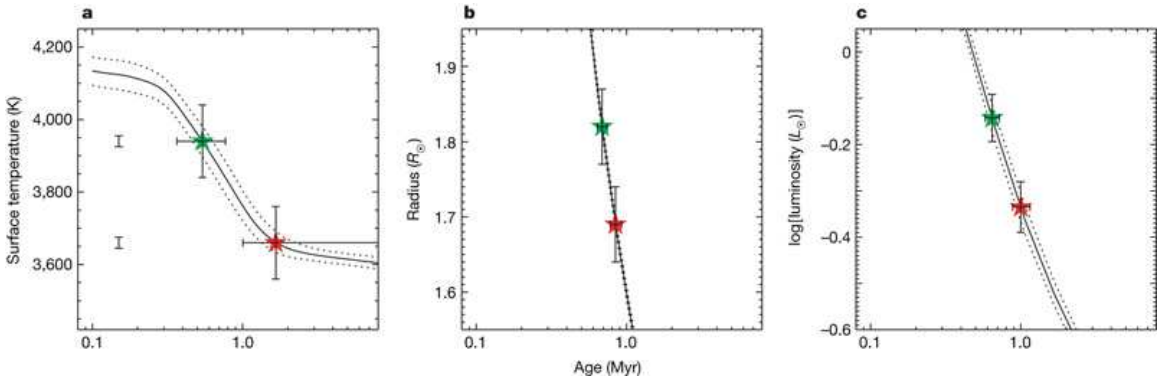

Figure 32: Comparison of Physical Properties of Par 1802 with Theoretical Models. This figure is adopted from SMC08.

Another source of discrepancy between the evolutionary tracks and the physical properties of young, low-mass eclipsing binary components may be due to uncertainties in theoretical spectra of cool objects. These spectra are characterized by having molecular lines and line blanketing which are not yet modeled satisfactorily, and may affect the determination of the effective temperatures from fitting model atmospheres to observed spectra.

The particularities of these pre-main sequence, low-mass systems, Par 1802 and 2M0535−05, may well be due to intrinsic differences between young stellar and substellar objects at these young ages. It could be that because they are so young ($\sim$ 1 Myrs), they still strongly affected by initial conditions associated with their formation. More precise measurements of the physical properties of young, low-mass objects will allow us to determine whether Par 1802 and 2M0535−05 are the exception or the rule.

VII.2 Results in Context

We compare the current evolutionary models of Baraffe et al. (1998) to the available observational constraints provided by Par 1802, 2M0535−05, and the four other known low-mass, PMS eclipsing binaries (see Table 1).

Theoretical evolutionary tracks by Baraffe et al. (1998) of ages younger than 1 Myrs are not available because the definition of the birthline which marks the beginning of the PMS evolution is uncertain and varies from one model to another. The theoretical tracks shown in Figures 33 and 34 model non-rotating stars with a

low-efficiency convection, modeled by a mixing-length parameter of $\alpha = 1.0$. This choice of α has been found to be more appropriate for reproducing the levels of lithium depletion found in PMS stars (e.g., Stassun et al., 2004), as well as reproducing the larger radii observed in active eclipsing binaries (e.g., Morales et al., 2010). Their radiative properties are determined using model atmospheres. Though spectral line lists have greatly improved in the recent past, molecular lines remain a challenge for the modeling cool stars and brown dwarfs.

In general, the models of PMS evolution fit the observed properties of the low-mass components of young eclipsing binaries well. They predict correctly that the more massive component will have a larger radius than its companion, as shown in Figure 33. This success in describing the evolution of the internal structure is mostly attributed to a suitable equation of state. Even in the substellar regime, the models are consistent with the measured radii and masses of the components of 2M0535−05. However, as mentioned above, the observed properties of Par 1802's components cannot be reproduced by a single isochrone. This is perhaps due to a difference in age, in convection efficiency, or in magnetic activity.

As shown in Fig. 34, the models predict that the more massive object is going to have a larger radius and a higher effective temperature than its lower-mass companion. The theory generally agrees with the observed properties of the other PMS EBs. However, both Par 1802 and 2M0535−05 deviate from this trend. Par 1802's secondary component falls on the 0.4 $M_{\odot}$ track as expected from its measured mass, however the primary's effective temperature is too high to be described by the same

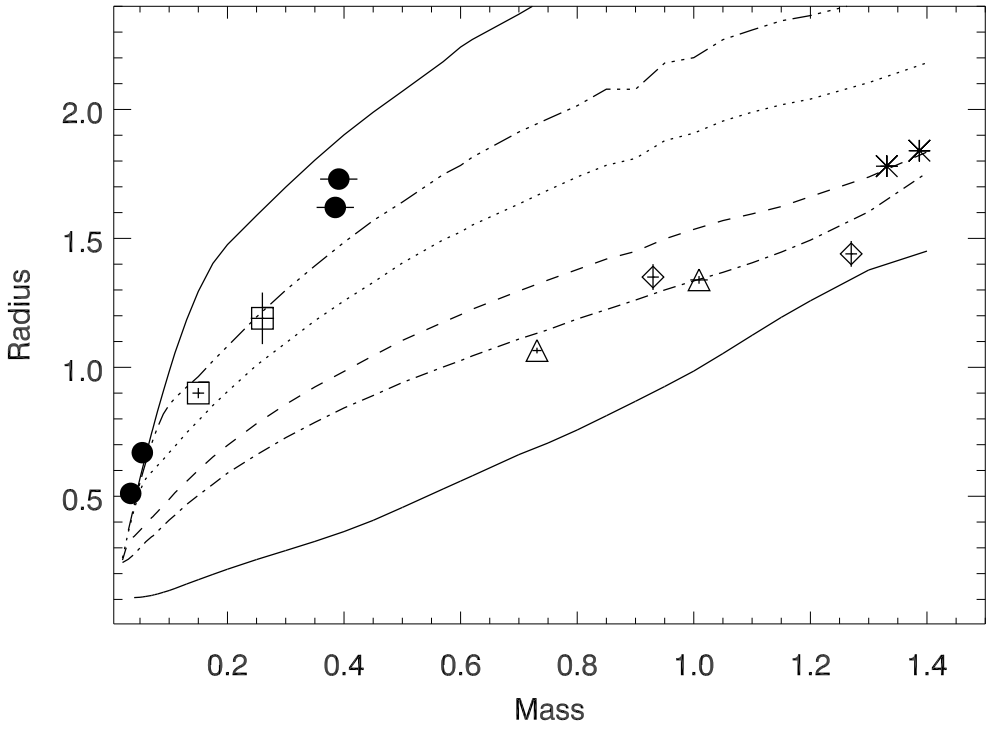

Figure 33: Observed and Theoretical Mass-Radius Relationship. The components of Par 1802 and 2M0535−05 are marked by the filled circles; the rest of the EBs in Table 1 are shown with the open symbols. They are compared to the theoretical isochrones of (Baraffe et al., 1998) (lines from the left-top to the right-bottom corner) that correspond to ages of 1, 2, 3, 6.5, 10, and 300 Myrs.

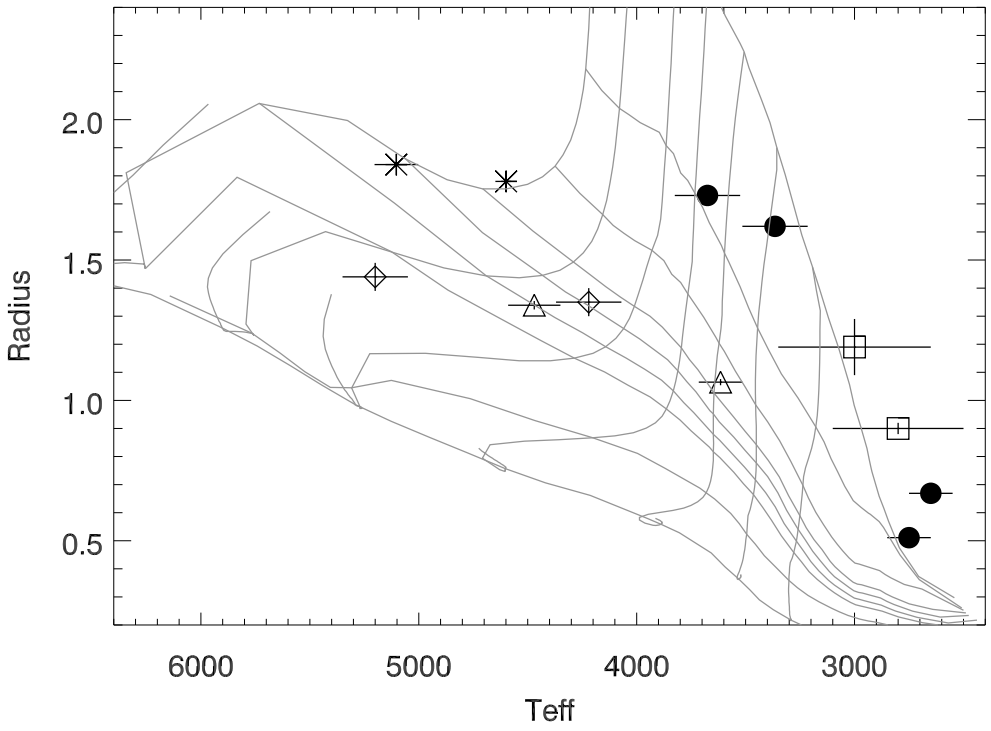

Figure 34: Observed and Theoretical Effective Temperature-Radius Relationship. The EB are marked with the same symbols used in Fig. 33. The slanted lines from the top-right to the bottom-left corner represent isochrones that correspond to ages of 1, 3, 6.5, 15.8, 20, 40, 60, 100, and 300 Myrs. The lines that start at the 1 Myr isochrone (or at the top of the plot) and descend almost vertically during the first few Myrs represent the evolution of different mass stars. From right to left, they correspond to masses of 0.2, 0.4, 0.6, 0.8, 1.0, 1.2, and 1.4 $M_{\odot}$.

evolutionary track. Moreover, this models do not allow for a difference in age to explain the observed radii and temperatures for Par 1802. Maybe differences in their magnetic activity and/or the convective efficiency in their interiors could reproduce our observations. Contrary to the trend, the more massive component of 2M0535−05 is cooler than its companion. A difference in activity levels of the brown dwarfs, supported by the measured rotation periods and Hα measurements, may explain the apparent temperature reversal.

Par 1802, 2M0535−05 and the other four low-mass, PMS EBs are an important source of observational constraints that, as larger telescopes and techniques, such as Doppler imaging, are developed, will continue to provide insight into the nature of young, low-mass stars and brown dwarfs. For example, these improvements will allow to better characterize the spot configuration of the EB components, probing their magnetic field structure.

VII.3 In Progress and Future Work

To better understand the particularities of Par 1802, we intend to analyze new 3.6 μm and 4.5 μm light curves together with our previous data. These data extend the observed wavelength range further into the infrared, with the inclusion of Spitzer's Infrared Array Camera[1] (IRAC) passbands centered at 3.6 μm and 4.5 μm. These light curves will also allow us to search for evidence of the third body at redder wavelengths, and thus test our proposed scenario. We are currently working with

[1] http://ssc.spitzer.caltech.edu/irac/

Andrej Prša to expand PHOEBE's capabilities in order to enable the modeling of IRAC passbands. As part of this work, we will need to extend the current spectral line lists in PHOEBE beyond 4μm.

Each IRAC light curve spans about 40 days, during which Par 1802 was observed 81 times in the bluer band and 162 in the redder band (see Figure 35). Additionally, we have additional J-band data (31 points) that span two months at the end of 2009 and that cover the time of the Spitzer observations. The J-band data was obtained with the 3.8-m UKIRT[2] telescope in Mauna Kea, Hawai'i. These new light curves were kindly provided by John Stauffer from Caltech, and are also shown in Fig. 35.

Both IRAC light curves are calibrated in absolute magnitudes. There is a definite variation of the light curves larger than the uncertainty of each measurement, the mean of which is ~ 0.004 magnitudes at 4.5μm and ~ 0.003i at 3.6μm. The J-band light curve, as provided to us, did not have individual uncertainty measurements so I calculated the mean of the out-of-eclipse portion of the light curve to assign as an upper limit to the photometry's uncertainty in this band, $\sigma_J \sim 0.006$. The addition of absolute light curves to the differential light curves we have analyzed will enable us to better constrain the temperatures of the components. For example, it has been shown by Wilson (2008) that it is possible to determine the effective temperatures of both components in an eclipsing binary when the light curves are computed in physical units of flux.

A periodicity analysis on the light curves will also be performed. The IRAC

[2]http://www.jach.hawaii.edu/UKIRT/

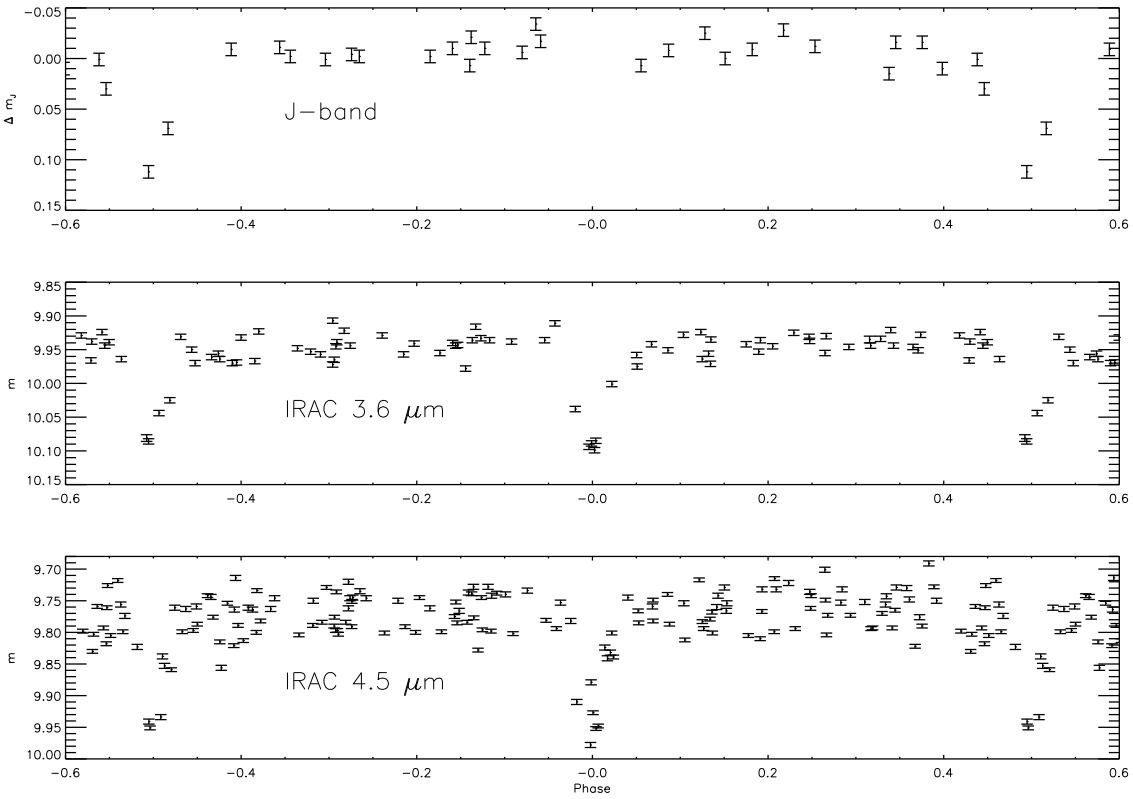

Figure 35: Spitzer IRAC and new J Light Curves of Par 1802.

light curves are not limited to only the nighttime, as are ground-based observations, and do not contain any effects of a 1.0-day sampling window. The time between observations of Par 1802 varies from several hours ($\sim$ 5 h) to less than a day ($\sim$ 0.8 d). The amplitude of the variation due to spots decreases with increasing wavelength; however the IRAC and UKIRT light curves are more precise than the previously analyzed light curves and show variability, in particular at 4.5 μm, greater than the photometric precision.

The determination of the fundamental properties of PMS eclipsing binaries, like those presented in this work, provides fundamental observational constraints for the understanding of the formation and early evolution of low-mass stars and brown dwarfs.

APPENDIX A

PHOEBE: CONFIGURATION FILE

This appendix presents a sample configuration file for the modeling of 2M0535−05 with PHOEBE, which is compatible for use with both the graphical interface and the back-end scripter.

```
# Parameter file conforming to PHOEBE svn
phoebe_rvno = 2
phoebe_spots_no = 0
phoebe_spno = 0
phoebe_lcno = 4
phoebe_opsf[1].VAL = 0.000000
phoebe_opsf[2].VAL = 0.000000
phoebe_opsf[3].VAL = 0.000000
phoebe_opsf[4].VAL = 0.000000
phoebe_opsf.ADJ = 0
phoebe_opsf.STEP = 1.000000e-02
phoebe_opsf.MIN = 0.000000
phoebe_opsf.MAX = 10000000000.000000
phoebe_name = "SM 4147 - swapped"
phoebe_ld_ybol1 = 0.500000
phoebe_reffect_switch = 0
phoebe_ld_ybol2 = 0.500000
phoebe_dpdt.VAL = 0.000000000000
phoebe_dpdt.ADJ = 0
phoebe_dpdt.STEP = 1.000000e-06
phoebe_dpdt.MIN = -1.000000
phoebe_dpdt.MAX = 1.000000
phoebe_logg1 = 3.516953
phoebe_rv_filename[1] = "sm4147.rv.p.phoebe.dat"
phoebe_rv_filename[2] = "sm4147.rv.s.phoebe.dat"
phoebe_logg2 = 3.536255
phoebe_lc_dep[1] = "Magnitude"
phoebe_lc_dep[2] = "Magnitude"
phoebe_lc_dep[3] = "Magnitude"
```

```
phoebe_lc_dep[4] = "Magnitude"
phoebe_ld_lcy1[1] = 0.500000
phoebe_ld_lcy1[2] = 0.500000
phoebe_ld_lcy1[3] = 0.500000
phoebe_ld_lcy1[4] = 0.500000
phoebe_compute_hla_switch = 0
phoebe_bins_switch = 0
phoebe_ld_lcy2[1] = 0.500000
phoebe_ld_lcy2[2] = 0.500000
phoebe_ld_lcy2[3] = 0.500000
phoebe_ld_lcy2[4] = 0.500000
phoebe_lc_filter[1] = "Johnson:H"
phoebe_lc_filter[2] = "Johnson:J"
phoebe_lc_filter[3] = "Johnson:K"
phoebe_lc_filter[4] = "Cousins:I"
phoebe_dc_spot2id = 1
phoebe_el3_units = "Total light"
phoebe_reffect_reflections = 2
phoebe_sma.VAL = 8.740220
phoebe_sma.ADJ = 0
phoebe_sma.STEP = 1.000000e-02
phoebe_sma.MIN = 0.000000
phoebe_sma.MAX = 10000000000.000000
phoebe_ie_factor = 3.100000
phoebe_nms_accuracy = 0.010000
phoebe_grb1.VAL = 0.320000
phoebe_grb1.ADJ = 0
phoebe_grb1.STEP = 1.000000e-02
phoebe_grb1.MIN = 0.000000
phoebe_grb1.MAX = 1.000000
phoebe_lc_indep[1] = "Time (HJD)"
phoebe_lc_indep[2] = "Time (HJD)"
phoebe_lc_indep[3] = "Time (HJD)"
phoebe_lc_indep[4] = "Time (HJD)"
phoebe_grb2.VAL = 0.320000
phoebe_grb2.ADJ = 0
phoebe_grb2.STEP = 1.000000e-02
phoebe_grb2.MIN = 0.000000
phoebe_grb2.MAX = 1.000000
phoebe_incl.VAL = 88.491300
phoebe_incl.ADJ = 1
phoebe_incl.STEP = 1.000000e-02
phoebe_incl.MIN = 0.000000
```

```
phoebe_incl.MAX = 180.000000
phoebe_period.VAL = 9.779560017000
phoebe_period.ADJ = 0
phoebe_period.STEP = 1.000000e-04
phoebe_period.MIN = 0.000000
phoebe_period.MAX = 10000000000.000000
phoebe_indep = "Time (HJD)"
phoebe_grid_coarsesize1 = 10
phoebe_hla[1].VAL = 7.848573
phoebe_hla[2].VAL = 7.176495
phoebe_hla[3].VAL = 7.402460
phoebe_hla[4].VAL = 7.010534
phoebe_hla.ADJ = 1
phoebe_hla.STEP = 1.000000e-02
phoebe_hla.MIN = 0.000000
phoebe_hla.MAX = 10000000000.000000
phoebe_grid_coarsesize2 = 10
phoebe_atm1_switch = 1
phoebe_ld_model = "Square root law"
scripter_ordinate_reversed_switch = 0
wd_spots_lat1.VAL = 0.000000
wd_spots_lat1.ADJ = 0
wd_spots_lat1.STEP = 1.000000e-02
wd_spots_lat1.MIN = 0.000000
wd_spots_lat1.MAX = 3.141593
phoebe_f1.VAL = 2.972510
phoebe_f1.ADJ = 0
phoebe_f1.STEP = 1.000000e-02
phoebe_f1.MIN = 1.000000
phoebe_f1.MAX = 10.000000
wd_spots_lat2.VAL = 0.000000
wd_spots_lat2.ADJ = 0
wd_spots_lat2.STEP = 1.000000e-02
wd_spots_lat2.MIN = 0.000000
wd_spots_lat2.MAX = 3.141593
phoebe_f2.VAL = 0.698540
phoebe_f2.ADJ = 0
phoebe_f2.STEP = 1.000000e-02
phoebe_f2.MIN = 0.000000
phoebe_f2.MAX = 1.000000
phoebe_rv_indep[1] = "Time (HJD)"
phoebe_rv_indep[2] = "Time (HJD)"
phoebe_model = "Detached binary"
```

```
phoebe_bins = 100
phoebe_atm2_switch = 1
phoebe_vga.VAL = 24.057371
phoebe_vga.ADJ = 0
phoebe_vga.STEP = 1.000000e-01
phoebe_vga.MIN = -1000.000000
phoebe_vga.MAX = 1000.000000
phoebe_nms_iters_max = 200
phoebe_hjd0.VAL = 2452617.177000000142
phoebe_hjd0.ADJ = 0
phoebe_hjd0.STEP = 1.000000e-04
phoebe_hjd0.MIN = -10000000000.000000
phoebe_hjd0.MAX = 10000000000.000000
phoebe_dperdt.VAL = 0.000000000000
phoebe_dperdt.ADJ = 0
phoebe_dperdt.STEP = 1.000000e-06
phoebe_dperdt.MIN = -1.000000
phoebe_dperdt.MAX = 1.000000
phoebe_dc_spot1src = 1
phoebe_lc_active[1] = 0
phoebe_lc_active[2] = 0
phoebe_lc_active[3] = 0
phoebe_lc_active[4] = 0
phoebe_lc_indweight[1] = "Unavailable"
phoebe_lc_indweight[2] = "Unavailable"
phoebe_lc_indweight[3] = "Unavailable"
phoebe_lc_indweight[4] = "Standard deviation"
phoebe_synscatter_seed = 150000000.000000
phoebe_mbol1 = 8.825751
phoebe_synscatter_switch = 0
phoebe_proximity_rv2_switch = 1
phoebe_mbol2 = 9.151553
phoebe_spots_corotate1 = 1
phoebe_spots_corotate2 = 1
phoebe_pshift.VAL = -0.427230
phoebe_pshift.ADJ = 1
phoebe_pshift.STEP = 1.000000e-04
phoebe_pshift.MIN = -0.500000
phoebe_pshift.MAX = 0.500000
phoebe_rm.VAL = 0.638690
phoebe_rm.ADJ = 0
phoebe_rm.STEP = 1.000000e-02
phoebe_rm.MIN = 0.000000
```

```
phoebe_rm.MAX = 10000000000.000000
phoebe_lc_filename[1] = "sm4147.H.20070926.lc"
phoebe_lc_filename[2] = "sm4147.J.20070926.lc"
phoebe_lc_filename[3] = "sm4147.K.20070926.lc"
phoebe_lc_filename[4] = "sm4147.I.unrect.20060624.txt"
phoebe_ld_rvx1[1] = 0.500000
phoebe_ld_rvx1[2] = 0.500000
phoebe_ld_rvx2[1] = 0.500000
phoebe_ld_rvx2[2] = 0.500000
phoebe_lc_sigma[1] = 0.017992
phoebe_lc_sigma[2] = 0.018902
phoebe_lc_sigma[3] = 0.043457
phoebe_lc_sigma[4] = 0.010000
phoebe_sbr1 = 5.534031
phoebe_synscatter_sigma = 0.010000
phoebe_rv_id[1] = "Primary RV"
phoebe_rv_id[2] = "Undefined"
phoebe_rv_id[3] = "Undefined"
phoebe_sbr2 = 5.534031
phoebe_spectra_disptype = "Linear"
phoebe_ecc.VAL = 0.321603
phoebe_ecc.ADJ = 1
phoebe_ecc.STEP = 1.000000e-03
phoebe_ecc.MIN = 0.000000
phoebe_ecc.MAX = 1.000000
phoebe_cla[1].VAL = 4.794885
phoebe_cla[2].VAL = 5.400436
phoebe_cla[3].VAL = 5.211816
phoebe_cla[4].VAL = 5.599514
phoebe_cla.ADJ = 0
phoebe_cla.STEP = 1.000000e-02
phoebe_cla.MIN = 0.000000
phoebe_cla.MAX = 10000000000.000000
phoebe_perr0.VAL = 3.757110
phoebe_perr0.ADJ = 1
phoebe_perr0.STEP = 1.000000e-03
phoebe_perr0.MIN = 0.000000
phoebe_perr0.MAX = 6.283185
phoebe_mnorm = 0.000000
phoebe_rv_sigma[1] = 1.591197
phoebe_rv_sigma[2] = 1.673940
phoebe_mass1 = 0.057237
phoebe_dc_spot2src = 2
```

```
phoebe_mass2 = 0.036557
phoebe_ie_excess = 0.000000
phoebe_rv_filter[1] = "Johnson:H"
phoebe_rv_filter[2] = "Johnson:H"
phoebe_grid_finesize1 = 40
phoebe_grid_finesize2 = 40
phoebe_passband_mode = "Interpolation"
phoebe_rv_indweight[1] = "Standard deviation"
phoebe_rv_indweight[2] = "Standard deviation"
phoebe_plum1 = 1.000000
phoebe_met1.VAL = 0.000000
phoebe_met1.ADJ = 0
phoebe_met1.STEP = 1.000000e-02
phoebe_met1.MIN = -10.000000
phoebe_met1.MAX = 10.000000
phoebe_pot1.VAL = 13.629750
phoebe_pot1.ADJ = 1
phoebe_pot1.STEP = 1.000000e-01
phoebe_pot1.MIN = 0.000000
phoebe_pot1.MAX = 10000000000.000000
scripter_verbosity_level = 1
phoebe_plum2 = 0.610924
phoebe_met2.VAL = 0.000000
phoebe_met2.ADJ = 0
phoebe_met2.STEP = 1.000000e-02
phoebe_met2.MIN = -10.000000
phoebe_met2.MAX = 10.000000
phoebe_pot2.VAL = 11.999050
phoebe_pot2.ADJ = 1
phoebe_pot2.STEP = 1.000000e-01
phoebe_pot2.MIN = 0.000000
phoebe_pot2.MAX = 10000000000.000000
phoebe_lc_levweight[1] = "None"
phoebe_lc_levweight[2] = "None"
phoebe_lc_levweight[3] = "None"
phoebe_lc_levweight[4] = "None"
phoebe_extinction[1].VAL = 0.000000
phoebe_extinction[2].VAL = 0.000000
phoebe_extinction[3].VAL = 0.000000
phoebe_extinction[4].VAL = 0.000000
phoebe_extinction.ADJ = 0
phoebe_extinction.STEP = 1.000000e-02
phoebe_extinction.MIN = 0.000000
```

```
phoebe_extinction.MAX = 100.000000
phoebe_proximity_rv1_switch = 1
phoebe_spots_units = "Radians"
phoebe_ie_switch = 0
phoebe_lc_id[1] = "Undefined"
phoebe_lc_id[2] = "Undefined"
phoebe_lc_id[3] = "Undefined"
phoebe_lc_id[4] = "Undefined"
wd_spots_temp1.VAL = 0.900000
wd_spots_temp1.ADJ = 0
wd_spots_temp1.STEP = 1.000000e-02
wd_spots_temp1.MIN = 0.000000
wd_spots_temp1.MAX = 100.000000
wd_spots_temp2.VAL = 0.900000
wd_spots_temp2.ADJ = 0
wd_spots_temp2.STEP = 1.000000e-02
wd_spots_temp2.MIN = 0.000000
wd_spots_temp2.MAX = 100.000000
phoebe_usecla_switch = 0
phoebe_ld_rvy1[1] = 0.500000
phoebe_ld_rvy1[2] = 0.500000
phoebe_el3[1].VAL = 0.000000
phoebe_el3[2].VAL = 0.000000
phoebe_el3[3].VAL = 0.000000
phoebe_el3[4].VAL = 0.000000
phoebe_el3.ADJ = 0
phoebe_el3.STEP = 1.000000e-02
phoebe_el3.MIN = 0.000000
phoebe_el3.MAX = 1000.000000
phoebe_ld_rvy2[1] = 0.500000
phoebe_ld_rvy2[2] = 0.500000
phoebe_dc_symder_switch = 1
phoebe_alb1.VAL = 0.600000
phoebe_alb1.ADJ = 0
phoebe_alb1.STEP = 1.000000e-02
phoebe_alb1.MIN = 0.000000
phoebe_alb1.MAX = 1.000000
phoebe_ld_lcx1[1].VAL = 0.500000
phoebe_ld_lcx1[2].VAL = 0.500000
phoebe_ld_lcx1[3].VAL = 0.500000
phoebe_ld_lcx1[4].VAL = 0.500000
phoebe_ld_lcx1.ADJ = 0
phoebe_ld_lcx1.STEP = 1.000000e-02
```

```
phoebe_ld_lcx1.MIN = 0.000000
phoebe_ld_lcx1.MAX = 1.000000
phoebe_dc_spot1id = 1
phoebe_alb2.VAL = 0.600000
phoebe_alb2.ADJ = 0
phoebe_alb2.STEP = 1.000000e-02
phoebe_alb2.MIN = 0.000000
phoebe_alb2.MAX = 1.000000
phoebe_ld_lcx2[1].VAL = 0.500000
phoebe_ld_lcx2[2].VAL = 0.500000
phoebe_ld_lcx2[3].VAL = 0.500000
phoebe_ld_lcx2[4].VAL = 0.500000
phoebe_ld_lcx2.ADJ = 0
phoebe_ld_lcx2.STEP = 1.000000e-02
phoebe_ld_lcx2.MIN = 0.000000
phoebe_ld_lcx2.MAX = 1.000000
phoebe_radius1 = 0.690503
wd_spots_rad1.VAL = 0.200000
wd_spots_rad1.ADJ = 0
wd_spots_rad1.STEP = 1.000000e-02
wd_spots_rad1.MIN = 0.000000
wd_spots_rad1.MAX = 3.141593
phoebe_ld_xbol1 = 0.500000
phoebe_radius2 = 0.539710
wd_spots_rad2.VAL = 0.200000
wd_spots_rad2.ADJ = 0
wd_spots_rad2.STEP = 1.000000e-02
wd_spots_rad2.MIN = 0.000000
wd_spots_rad2.MAX = 3.141593
phoebe_ld_xbol2 = 0.500000
phoebe_rv_dep[1] = "Primary RV"
phoebe_rv_dep[2] = "Secondary RV"
phoebe_synscatter_levweight = "Poissonian scatter"
phoebe_dc_lambda = 0.001000
phoebe_teff1.VAL = 2715.000000
phoebe_teff1.ADJ = 0
phoebe_teff1.STEP = 5.000000e+00
phoebe_teff1.MIN = 2000.000000
phoebe_teff1.MAX = 50000.000000
phoebe_compute_vga_switch = 0
phoebe_teff2.VAL = 2849.000000
phoebe_teff2.ADJ = 1
phoebe_teff2.STEP = 1.000000e+01
```

```
phoebe_teff2.MIN = 2000.000000
phoebe_teff2.MAX = 50000.000000
wd_spots_long1.VAL = 0.000000
wd_spots_long1.ADJ = 0
wd_spots_long1.STEP = 1.000000e-02
wd_spots_long1.MIN = 0.000000
wd_spots_long1.MAX = 6.283185
wd_spots_long2.VAL = 0.000000
wd_spots_long2.ADJ = 0
wd_spots_long2.STEP = 1.000000e-02
wd_spots_long2.MIN = 0.000000
wd_spots_long2.MAX = 6.283185
phoebe_rv_active[1] = 1
phoebe_rv_active[2] = 1
```

APPENDIX B

PHOEBE: MODELING SCRIPT

This appendix presents a sample of commands utilized in PHOEBE's Back-end Scripter to model the radial velocity and the light curves of the double-lined, detached eclipsing binary Par 1802.

```
# Ephemeris:
set_parameter_value (phoebe_hjd0,2452947.618)
set_parameter_value (phoebe_period,4.673843)
set_parameter_value (phoebe_pshift,0.0012)
set_parameter_value (phoebe_dpdt,0.0)

# Initial values of e and omega:
set_parameter_value (phoebe_ecc,0.07)
set_parameter_value (phoebe_perr0,CONST_PI*1.514)

# Synchronicity parameter:
set_parameter_value (phoebe_f1,1.009700) # From periodicity analysis
set_parameter_value (phoebe_f2,1.009700)
# Redefine limits for sub-synchronous rotation:
set_parameter_limits (phoebe_f1,0.0,4.0)
set_parameter_limits (phoebe_f2,0.0,4.0)

# Curves will be modeled in:
set_parameter_value (phoebe_indep,1) # Time

# Load RV files:
set_parameter_value (phoebe_rvno,2)
set_parameter_value (phoebe_rv_filename,"sm2654.rv.p.20070922.txt",1)
set_parameter_value (phoebe_rv_filename,"sm2654.rv.s.20070922a.txt",2)
set_parameter_value (phoebe_rv_dep,1,1) #Primary RV
set_parameter_value (phoebe_rv_dep,2,2) #Secondary RV
set_parameter_value (phoebe_rv_indep,1,1) # JDs
set_parameter_value (phoebe_rv_indep,1,2) # JDs
set_parameter_value (phoebe_rv_indweight,2,1) #Standard deviation
set_parameter_value (phoebe_rv_indweight,2,2) #Standard deviation
set_parameter_value (phoebe_rv_sigma,1.0,1)#When indvweights are STDDEV
set_parameter_value (phoebe_rv_sigma,1.0,2)#que no se dupliquen.
```

```
# RV Passbands:
set_parameter_value (phoebe_rv_filter,8,1) # R cousins
set_parameter_value (phoebe_rv_filter,8,2) # R cousins

#Set Limb Darkening law:
set_parameter_value (phoebe_ld_model,3)

# Inclination angle to 90:
set_parameter_value (phoebe_incl,90.0)

# Initial estimates:
set_parameter_value (phoebe_sma,10.00)
set_parameter_value (phoebe_rm,1.0)
set_parameter_value (phoebe_vga,25)

execute "calc_sigmas.script"

set sigmarv1 = calc_rv_sigma(1)
set sigmarv2 = calc_rv_sigma(2)
#print sigmarv1,"",sigmarv2
#info phoebe_rv_sigma
#set_parameter_value (phoebe_rv_sigma,sigmarv1,1)
#set_parameter_value (phoebe_rv_sigma,sigmarv2,2)

save_parameter_file ("rvs.090420.01.phoebe")

# Minimize for adjustable parameters
mark_for_adjustment(phoebe_pshift,1)
mark_for_adjustment(phoebe_sma,1)
mark_for_adjustment(phoebe_rm,1)
mark_for_adjustment(phoebe_vga,1)
#mark_for_adjustment(phoebe_ecc,1) # Because it tends to values < 0.
#mark_for_adjustment(phoebe_perr0,1) #Same as above

set_parameter_value (phoebe_rv_active,1,1)
set_parameter_value (phoebe_rv_active,1,2)

for (i=1;i<=3;i++) {
set a = minimize_using_dc()
print a
adopt_minimizer_results(a) }

#verify steps of adjustable parameters
```

```
set_parameter_step(phoebe_pshift,0.0001)
set_parameter_step(phoebe_sma,0.01)
set_parameter_step(phoebe_rm,0.001)
set_parameter_step(phoebe_vga,0.1)
set_parameter_step(phoebe_ecc,0.001)
set_parameter_step(phoebe_perr0,0.001)

#turn on proximity effects
set_parameter_value (phoebe_proximity_rv2_switch,1)
set_parameter_value (phoebe_proximity_rv1_switch,1)

# Minimize again and update sigmas
for (i=1;i<=3;i++) {
set a = minimize_using_dc()
print a
adopt_minimizer_results(a) }

#set sigmarv1 = calc_rv_sigma(1) #Don't UPDATE SIGMAS BECAUSE
#set sigmarv2 = calc_rv_sigma(2) #THE RVs HAVE INDIVIDUAL WEIGHTS!
#set_parameter_value (phoebe_rv_sigma,sigmarv1,1)
#set_parameter_value (phoebe_rv_sigma,sigmarv2,2)

#Set grids to be finer
set_parameter_value (phoebe_grid_coarsesize1,10)
set_parameter_value (phoebe_grid_coarsesize2,10)
set_parameter_value (phoebe_grid_finesize1,40)
set_parameter_value (phoebe_grid_finesize2,40)

mark_for_adjustment(phoebe_pshift,0)
mark_for_adjustment(phoebe_sma,0)
mark_for_adjustment(phoebe_rm,0)
mark_for_adjustment(phoebe_vga,0)
mark_for_adjustment(phoebe_ecc,0)
mark_for_adjustment(phoebe_perr0,0)

#save_parameter_file ("rvs.phoebe")
save_parameter_file ("rvs.090420.02.phoebe")

#value of sma at 90°that will use from now on, when changing inclination
#set aconst = get_parameter_value (phoebe_sma)
#For 20090420, sm2654:
set aconst = 10.669816
```

```
#if not fitting rm, sma nor vga or ECC & Perr0, then de-activate RVs
set_parameter_value (phoebe_rv_active,0,1)
set_parameter_value (phoebe_rv_active,0,2)

# routine to change the value of the semi-major axis as i changes
macro sma (a) {
set_parameter_value (phoebe_sma,a/sin(get_parameter_value (phoebe_incl)*
   CONST_PI/180.0))}

#ADD LCS
set_parameter_value (phoebe_lcno,6)
set_parameter_value (phoebe_lc_filename,"sm2654.H.20081120.lc",1)
set_parameter_value (phoebe_lc_filename,"sm2654.J.20081120.lc",2)
set_parameter_value (phoebe_lc_filename,"sm2654.K.20081120.lc",3)
set_parameter_value (phoebe_lc_filename,"sm2654.I.20090418.unrect.txt",4)
set_parameter_value (phoebe_lc_filename,"sm2654.V.20090418.unrect.txt",5)
set_parameter_value (phoebe_lc_filename,"sm2654.B.20090418.unrect.txt",6)

set_parameter_value (phoebe_lc_indep,1,1)
set_parameter_value (phoebe_lc_indep,1,2)
set_parameter_value (phoebe_lc_indep,1,3)
set_parameter_value (phoebe_lc_indep,1,4)
set_parameter_value (phoebe_lc_indep,1,5)
set_parameter_value (phoebe_lc_indep,1,6)

set_parameter_value (phoebe_lc_dep,1,1)
set_parameter_value (phoebe_lc_dep,1,2)
set_parameter_value (phoebe_lc_dep,1,3)
set_parameter_value (phoebe_lc_dep,1,4)
set_parameter_value (phoebe_lc_dep,1,5)
set_parameter_value (phoebe_lc_dep,1,6)

set_parameter_value (phoebe_lc_indweight,3,1)
set_parameter_value (phoebe_lc_indweight,3,2) # 3 = Unavailable
set_parameter_value (phoebe_lc_indweight,3,3)
set_parameter_value (phoebe_lc_indweight,2,4)
set_parameter_value (phoebe_lc_indweight,2,5) # 2 = Standard deviation
set_parameter_value (phoebe_lc_indweight,2,6)

set_parameter_value (phoebe_lc_levweight,1,1) # 1 = None
set_parameter_value (phoebe_lc_levweight,1,2)
set_parameter_value (phoebe_lc_levweight,1,3)
set_parameter_value (phoebe_lc_levweight,1,4)
```

```
set_parameter_value (phoebe_lc_levweight,1,5)
set_parameter_value (phoebe_lc_levweight,1,6)

set_parameter_value (phoebe_lc_filter,65,1) #H
set_parameter_value (phoebe_lc_filter,64,2) #J
set_parameter_value (phoebe_lc_filter,66,3) #Ks
set_parameter_value (phoebe_lc_filter,9,4) #Ic
set_parameter_value (phoebe_lc_filter,61,5) #V
set_parameter_value (phoebe_lc_filter,60,6) #B
#print get_parameter_value (phoebe_lc_filter)

set_parameter_value (phoebe_name,"sm2654")
set_parameter_value (phoebe_lc_id,"H-band",1)
set_parameter_value (phoebe_lc_id,"J-band",2)
set_parameter_value (phoebe_lc_id,"Ks-band",3)
set_parameter_value (phoebe_lc_id,"Ic-band",4)
set_parameter_value (phoebe_lc_id,"V-band",5)
set_parameter_value (phoebe_lc_id,"B-band",6)

#unset all adjustable params
mark_for_adjustment(phoebe_pshift,0)
mark_for_adjustment(phoebe_sma,0)
mark_for_adjustment(phoebe_rm,0)
mark_for_adjustment(phoebe_vga,0)
mark_for_adjustment(phoebe_ecc,0)
mark_for_adjustment(phoebe_perr0,0)

# Passband sigmas
set_parameter_value (phoebe_lc_sigma,0.02,1)
set_parameter_value (phoebe_lc_sigma,0.02,2)
set_parameter_value (phoebe_lc_sigma,0.03,3)
set_parameter_value (phoebe_lc_sigma,1.0,4)
set_parameter_value (phoebe_lc_sigma,1.0,5)
set_parameter_value (phoebe_lc_sigma,1.0,6)

set_parameter_value (phoebe_model,4)
set_parameter_value (phoebe_reffect_switch,0) # 0 = Off
set_parameter_value (phoebe_mnorm,0.0)

set_parameter_value (phoebe_pot1,1/0.12)
set_parameter_value (phoebe_pot2,1/0.12)

set_parameter_value (phoebe_teff1,3850) # from broadband photometry
```

```
set_parameter_value (phoebe_teff2,3600)

#compute light levels
set hla = compute_light_levels()
for (i=1 ; i<=dim(hla) ; i++) { set_parameter_value (phoebe_hla,hla[i],i)
}

#Set LC sigmas:
#     JHK (start with Photometric scatter -> RMS of fit), BVI (1.0)
set sigh = calc_sigma(1)
set sigj = calc_sigma(2)
set sigk = calc_sigma(3)
set sigi = calc_sigma (4)
set sigv = calc_sigma (5)
set sigb = calc_sigma (6)
print sigh,"",sigj,"",sigk,"",sigi,"",sigv,"",sigb
print get_parameter_value (phoebe_lc_sigma)

#set_parameter_value (phoebe_lc_sigma,sigh,1)
#set_parameter_value (phoebe_lc_sigma,sigj,2)
#set_parameter_value (phoebe_lc_sigma,sigk,3)
#set_parameter_value (phoebe_lc_sigma,sigi,4)
#set_parameter_value (phoebe_lc_sigma,sigv,5)
#set_parameter_value (phoebe_lc_sigma,sigb,6)

#We are going to fit for the INCL and TEFF2, so we don't need RV curves
set_parameter_value (phoebe_rv_active,0,1)
set_parameter_value (phoebe_rv_active,0,2)

set_parameter_value (phoebe_incl,89.9)
sma(aconst)

mark_for_adjustment(phoebe_incl,1)
mark_for_adjustment(phoebe_teff2,1)
mark_for_adjustment(phoebe_pot1,1)
mark_for_adjustment(phoebe_pot2,1)

for (j = 1 ; j <= 3 ; j++) {
set a = minimize_using_dc()
print a
adopt_minimizer_results(a)
sma(aconst)
set hla = compute_light_levels()
```

```
for (i=1 ; i<=dim(hla) ; i++) { set_parameter_value (phoebe_hla,hla[i],i)
} }

mark_for_adjustment(phoebe_incl,0)
mark_for_adjustment(phoebe_teff2,0)
mark_for_adjustment(phoebe_pot1,0)
mark_for_adjustment(phoebe_pot2,0)

#adjust e,w,pshift for adjustment
mark_for_adjustment(phoebe_pshift,1)
mark_for_adjustment(phoebe_ecc,1)
mark_for_adjustment(phoebe_perr0,1)

set_parameter_value (phoebe_rv_active,1,1)
set_parameter_value (phoebe_rv_active,1,2)

for (j = 1 ; j <= 3 ; j++) {
set a = minimize_using_dc()
print a
adopt_minimizer_results(a) }

set_parameter_step (phoebe_ecc,0.001)
set_parameter_step (phoebe_pshift,0.0001)

mark_for_adjustment(phoebe_pshift,0)
mark_for_adjustment(phoebe_sma,0)
mark_for_adjustment(phoebe_rm,0)
mark_for_adjustment(phoebe_vga,0)
mark_for_adjustment(phoebe_ecc,0)
mark_for_adjustment(phoebe_perr0,0)
mark_for_adjustment(phoebe_incl,0)
mark_for_adjustment(phoebe_teff2,0)
mark_for_adjustment(phoebe_pot1,0)
mark_for_adjustment(phoebe_pot2,0)

save_parameter_file ("bvijhk.090420.02.phoebe")

#adjust all parameters
mark_for_adjustment(phoebe_pshift,1)
mark_for_adjustment(phoebe_sma,1)
mark_for_adjustment(phoebe_rm,1)
mark_for_adjustment(phoebe_vga,1)
mark_for_adjustment(phoebe_ecc,1)
```

```
mark_for_adjustment(phoebe_perr0,1)
mark_for_adjustment(phoebe_pshift,1)
mark_for_adjustment(phoebe_hla,1)
mark_for_adjustment(phoebe_incl,1)
mark_for_adjustment(phoebe_teff1,1)
mark_for_adjustment(phoebe_pot1,1)
mark_for_adjustment(phoebe_pot2,1)
mark_for_adjustment(phoebe_period,1)
mark_for_adjustment(phoebe_hjd0,1)
mark_for_adjustment(phoebe_teff2,1)

set_parameter_value (phoebe_rv_active,1,1)
set_parameter_value (phoebe_rv_active,1,2)

#DO NOT ADOPT MINIMIZATION RESULTS!
set a = minimize_using_dc()
print a
```

APPENDIX C

PHOEBE: PARAMETER CROSS SECTION SCANNING SCRIPT

This appendix presents a sample script written to scan the parameter cross section between the ratio of effective temperatures and the radii of radii, $(T_{\rm eff,1}/T_{\rm eff,2})$–$(R_2/R_1)$.

```
define sum (arr) {
        set retval = 0.0
        for (i = 1; i <= dim(arr); i++)
                set retval += arr[i]
        return retval }

define calc_sigma (index) {
        set_parameter_value (phoebe_indep,
                get_parameter_value (phoebe_lc_indep, index))

        set obs  = get_parameter_value (phoebe_lc_filename, index)
        set mag0 = get_parameter_value (phoebe_mnorm)

        set hjd = column (obs, 1)
        set mag = column (obs, 2)

        set lc = compute_lc (hjd, index)

        set diff = 10^(-2/5*(mag-mag0)) - lc.dep

        set sig_flux = sqrt(sum(diff^2)/(dim(diff)-1))

        return 5/2 * log(sig_flux+1)        }

#macro go (INDEX_NO) {
set INDEX_NO = 1

        open_parameter_file ("thlflux.ew.nt1.phoebe")

        set_parameter_value (phoebe_rv_active,0,1)
        set_parameter_value (phoebe_rv_active,0,2)

        mark_for_adjustment (phoebe_pot2,1)
```

```
mark_for_adjustment (phoebe_hla,0)
mark_for_adjustment (phoebe_pshift,0)

set t10= 30
set p10 = 0.4

set t2 = 3600
set p1 = 7.00
set p2 = get_parameter_value (phoebe_pot2)
set p1o = get_parameter_value (phoebe_pot1)

set chi2 = compute_chi2()
set minchi2 = sum(chi2)

print "Initial Chi2 ","\t",sum(chi2)

for (index = 1; index <= INDEX_NO; index++) {

        set t2r = t2 + rand(t10)
        set p1r = p1 + rand(p10)

        set_parameter_value (phoebe_teff2, t2r)
        set_parameter_value (phoebe_pot1,p1r)
        set_parameter_value (phoebe_pot2,
                p2+(p1o-get_parameter_value (phoebe_pot1)))

        set hla  = compute_light_levels()
        for (i = 1 ; i <= dim(hla) ; i++) {
                set_parameter_value (phoebe_hla,hla[i],i) }

        print " "
        print "Secondary Teff: ","\t", t2r
        print "Primary potential: ", "\t", p1r
        print " "

        set r = minimize_using_dc ()
        adopt_minimizer_results(r)
        print r
        set hla  = compute_light_levels()
        for (i = 1 ; i <= dim(hla) ; i++) {
                set_parameter_value (phoebe_hla,hla[i],i) }

        set tol = 1.5 # or whatever is appropriate
```

```
                set cfval = r.cfval

                for (j = 1 ; j < 3 ; j ++) {
                        set r = minimize_using_dc()
                        adopt_minimizer_results (r)
                        set hla  = compute_light_levels()
                        for (i = 1 ; i <= dim(hla) ; i++) {
                          set_parameter_value (phoebe_hla,hla[i],i) }
                        print r
                }

                while (cfval - r.cfval > tol) {
                        set cfval = r.cfval
                        set r = minimize_using_dc ()
                        print r
                        if (cfval - r.cfval > 0.0) {
                          adopt_minimizer_results(r)
                          set hla  = compute_light_levels()
                             for (i = 1 ; i <= dim(hla) ; i++) {
                                    set_parameter_value
                                        (phoebe_hla,hla[i],i) }
                                }
                }

                set cfval = compute_chi2 ()

                print index,"\t",get_parameter_value (phoebe_teff2),"\t",
                        get_parameter_value (phoebe_radius1), "\t",
                        get_parameter_value(phoebe_radius2), "\t",
                        get_parameter_value (phoebe_pot1), "\t",
                        get_parameter_value (phoebe_pot2),"\t",
                        r.cfval, "\t", sum(cfval), "\t", cfval[1], "\t",
                        cfval[2], "\t", cfval[3], "\t", cfval[4], "\t",
                        cfval[5], "\t", cfval[6], "\t", cfval[7], "\t",
                        cfval[8], "\n" ->> "vijhk.tr.100123.results"
        }
}
```

APPENDIX D

PHOEBE: UNCERTAINTY DETERMINATION SCRIPT

This appendix contains the PHOEBE script used to determine the parameter uncertainties of the best RV+LC solution of Par 1802.

```
# Open the best fit parameter file
open_parameter_file ("thli40.phoebe")

#define variables
set m1 = get_parameter_value (phoebe_mass1)
set m2 = get_parameter_value (phoebe_mass2)
set r1 = get_parameter_value (phoebe_radius1)
set r2 = get_parameter_value (phoebe_radius2)
set a = get_parameter_value (phoebe_sma)
set e = get_parameter_value (phoebe_ecc)
set w = get_parameter_value (phoebe_perr0)
set psh = get_parameter_value (phoebe_pshift)
set incl = get_parameter_value (phoebe_incl)
set vga = get_parameter_value (phoebe_vga)
set q = get_parameter_value (phoebe_rm)
set p = get_parameter_value (phoebe_period)
set f1 = get_parameter_value (phoebe_f1)
set f2 = get_parameter_value (phoebe_f2)
set teff2 = get_parameter_value (phoebe_teff2)
set teff1 = get_parameter_value (phoebe_teff1)
set p1 = get_parameter_value (phoebe_pot1)
set p2 = get_parameter_value (phoebe_pot2)

set akm = a*6.955e5 # Convert to km from R_sun

#This one comes independent of the EB modeling in days
set sigper = 0.000060
set sigpersec = sigper*24*3600 # convert from days to s
set psec = p*24*3600

# from periodicity analysis
set prot1 = 4.629
set prot2 = 4.629
set sigprot1 = 0.006
```

```
set sigprot2 = 0.006

# comes from determination of rotation period.
set sigf1 = f1*sqrt((sigper/p)^2 + (sigprot1/prot1)^2)
set sigf2 = f2*sqrt((sigper/p)^2 + (sigprot2/prot2)^2)

# From errors manuscript: #1
#find uncertainties of q and a sin i, vga
set_parameter_value (phoebe_rv_active,1,1)
set_parameter_value (phoebe_rv_active,1,2)

set_parameter_value (phoebe_lc_active,0,1)
set_parameter_value (phoebe_lc_active,0,2)
set_parameter_value (phoebe_lc_active,0,3)
set_parameter_value (phoebe_lc_active,0,4)
set_parameter_value (phoebe_lc_active,0,5)
set_parameter_value (phoebe_lc_active,0,6)

# #2
set aconst = a * sin(incl*CONST_PI/180.0)
macro sma (aa) { set_parameter_value (phoebe_sma,
aa/sin(get_parameter_value (phoebe_incl)*CONST_PI/180.0))}

set_parameter_value (phoebe_incl,90.0)

mark_for_adjustment (phoebe_sma,1)
mark_for_adjustment (phoebe_rm,1)
mark_for_adjustment (phoebe_vga,1)
mark_for_adjustment (phoebe_perr0,1)
mark_for_adjustment (phoebe_ecc,1)
mark_for_adjustment (phoebe_pshift,1)

mark_for_adjustment (phoebe_pot1,0)
mark_for_adjustment (phoebe_pot2,0)
mark_for_adjustment (phoebe_teff2,0)
mark_for_adjustment (phoebe_teff1,0)
mark_for_adjustment (phoebe_hla,0)

#set rvs = minimize_using_dc()
print rvs

set sigasini = rvs.ferrors[1]
set sigvga = rvs.ferrors[5]
```

```
set sigq = rvs.ferrors[6]

print "sasini = ",sigasini,"\t","sigvga = ",sigvga,"\t","sigq = ",sigq

# From ERRORS paper: #3
set_parameter_value (phoebe_incl, incl)
sma(aconst)

# From errors: #4
set_parameter_value (phoebe_rv_active,1,1)
set_parameter_value (phoebe_rv_active,1,2)

set_parameter_value (phoebe_lc_active,1,1)
set_parameter_value (phoebe_lc_active,1,2)
set_parameter_value (phoebe_lc_active,1,3)
set_parameter_value (phoebe_lc_active,1,4)
set_parameter_value (phoebe_lc_active,1,5)
set_parameter_value (phoebe_lc_active,0,6)

mark_for_adjustment (phoebe_sma,0)
mark_for_adjustment (phoebe_rm,0)
mark_for_adjustment (phoebe_vga,0)

mark_for_adjustment (phoebe_pshift,1)
mark_for_adjustment (phoebe_incl,1)
mark_for_adjustment (phoebe_perr0,1)
mark_for_adjustment (phoebe_ecc,1)
mark_for_adjustment (phoebe_teff2,1)
mark_for_adjustment (phoebe_pot1,1)
mark_for_adjustment (phoebe_pot2,1)

mark_for_adjustment (phoebe_hla,1)

mark_for_adjustment (phoebe_el3,0)

#set b = minimize_using_dc()
print b

set sigpsh = b.ferrors[3]
set siginca = b.ferrors[4]
set sigperr0 = b.ferrors[2]
set sigecc = b.ferrors[1]
set sigteff2 = b.ferrors[5]
```

```
set sigp1 = b.ferrors[6]
set sigp2 = b.ferrors[7]

set siginclf = siginca*CONST_PI/180.0 #in radians

set siginclf = siginclf
##  from third light uncertainty
set siginclf = 8*CONST_PI/180.0 #in radians

## formal errors for:
set sigeccf = sigecc
set sigperr0f = sigperr0

## From heuristics:
set sigecc = 0.0026
set sigperr0 = 0.010*CONST_PI #In radians
set sigt1t2 = 0.0017


## Now #5:
set siga = sqrt((sigasini/sin(incl*CONST_PI/180.0))^2 +
(a* cos(incl*CONST_PI/180.0)*siginclf/sin(incl*CONST_PI/180.0))^2)
set sigakm = siga*6.955e5

## Now #6: Deferring to point #8
#print "R_1:   ",get_parameter_value ( phoebe_radius1),"  $\pm$  ",sigr1
#print get_parameter_value ( phoebe_radius2)

## Now #7
set sigm1 = m1 * sqrt((3*siga/a)^2 + (2*sigper/p)^2 + (sigq/(q+1))^2)

set sigm2 =  m2 * sqrt((3*siga/a)^2 + (2*sigper/p)^2 + (sigq/(q*(q+1)))^2)


### Now #8:
set den1 = (r1/a)^2 + (1-e)^2 - 2* r1/a * (1-e)
set a1p = -1/(r1/a)^2 - (q*(r1/a + e -1))/den1^(3/2)
  - q/(1-e)^2 + f1^2*(1 + q)*r1/a
set a2p = 1/den1^(1/2) - (r1/a)/(1-e)^2 + 0.5 * f1^2*(r1/a)^2
set a3p = - q*(r1/a + e -1)/den1^(3/2) - 2*q*r1/a/(1-e)^3
set a4p = f1*(1+q)*(r1/a)^2

set den2 = (r2/a)^2 + (1-e)^2 - 2* r2/a * (1-e)
```

```
set a1s = -1/(r2/a)^2 - (q*(r2/a + e -1))/den2^(3/2)
  - q/(1-e)^2 + f2^2*(1 + q)*r2/a
set a2s = 1/den2^(1/2) - r2/a/(1-e)^2 + 0.5 * f2^2*(r2/a)^2
set a3s = - q*(r2/a + e -1)/den2^(3/2) - 2*q*r2/a/(1-e)^3
set a4s = f2*(1+q)*(r2/a)^2

set sigrr1 = sqrt( (sigp1/a1p)^2 + (a2p*sigq/a1p)^2 +
   (a3p*sigecc/a1p)^2 + (a4p*sigf1/a1p)^2)
set sigrr2 = sqrt( (sigp2/a1s)^2 + (a2s*sigq/a1s)^2 +
   (a3s*sigecc/a1s)^2 + (a4s*sigf2/a1s)^2)

set sigr1 = r1*sqrt((siga/a)^2+(sigrr1/(r1/a))^2)
set sigr2 = r2*sqrt((siga/a)^2+(sigrr2/(r2/a))^2)

set sigr1f = sigr1
set sigr2f = sigr2

## From third light uncertainty:
set sigr1 = 0.020
set sigr2 = 0.020

define rsun2au (arsun) {
        set aau = arsun*6.9599e10/1.4960e13
        return aau }

### Calculate K's and logg's
set k1=2*CONST_PI*(akm/(1+1/q))/(psec)/sqrt(1-e^2)*sin(incl*CONST_PI/180)
set sigk1 = k1 * sqrt((sigasini/(aconst))^2+(sigpersec/psec)^2
      +(sigq/(q^2*(1+1/q)))^2+(e*sigecc/(1-e^2))^2)
set k2 = k1/q
set sigk2 = k2 * sqrt ( (sigk1/k1)^2 + (sigq/q)^2)

# g = 2.74e4 * (m/msun) * (rsun/r)^2 = Gm/r^2 [=] cm/s^2
set logg1 = log(m1/r1^2)+4.438
set siglogg1 = 1/ln(10) * sqrt ((sigm1/m1)^2+((2*sigr1)/r1)^2)

set logg2 = log(m2/r2^2)+4.438
set siglogg2 = 1/ln(10) * sqrt ((sigm2/m2)^2+((2*sigr2)/r2)^2)

### Calculate Total Mass from RV solution
# gravitational constant in (1/Msun 1/days^2 Rsun^3)
#set g = 6.67259e-8*(24.*3600.)^2*1.989e33/(6.955e10)^3
set g = 2944.8645 #Calculation above done in IDL
```

```
set msin3i = 4*CONST_PI^2*(aconst)^3/(g*p^2)
set sigmsin3i = msin3i *sqrt( (3*sigasini/aconst)^2 + (2*sigper/p)^2 )

# Printing out all errors:
print "     p =  ",get_parameter_value(phoebe_period),
 "  $\\pm$  ",sigper," (",sigper/p*100," %)"
print "     e =  ",get_parameter_value(phoebe_ecc),
         "  $\\pm$  ",sigecc," (",sigecc/e*100," %)"
print "     w =  ",get_parameter_value(phoebe_perr0)/CONST_PI,
 " pi  $\\pm$  ",sigperr0," (",sigperr0/w*100," %)"
print "   psh =  ",get_parameter_value(phoebe_pshift),
 "  $\\pm$  ",sigpsh," (",sigpsh/psh*100," %)"
print "     a =  ",get_parameter_value(phoebe_sma),
 "  $\\pm$  ",siga," (",siga/a*100," %)"
print "a (au) =  ",rsun2au(get_parameter_value(phoebe_sma))," $\\pm$  ",
   rsun2au(siga)," (",rsun2au(siga)/rsun2au(a)*100," %)"
print " asini =  ",rsun2au(aconst)," $\\pm$  ",rsun2au(sigasini),
 " (",sigasini/(aconst)*100," %)"
print "     i =  ",incl," $\\pm$  ",sigincl*180/CONST_PI," (",
   sigincl*180/CONST_PI/incl*100," %)"
print " gamma =  ",get_parameter_value(phoebe_vga)," $\\pm$  ",
   sigvga," (",sigvga/vga*100," %)"
print "    k1 =  ",k1," $\\pm$  ",sigk1," (",sigk1/k1*100," %)"
print "    k2 =  ",k2," $\\pm$  ",sigk2," (",sigk2/k2*100," %)"
print "     q =  ",q," $\\pm$  ",sigq," (",sigq/q*100," %)"
print "Msin3i =  ",msin3i," $\\pm$  ",sigmsin3i," (",
   sigmsin3i/msin3i*100," %)"
print "   M_1 =  ",get_parameter_value(phoebe_mass1),
 "  $\\pm$  ",sigm1," (",sigm1/m1*100," %)"
print "   M_2 =  ",get_parameter_value(phoebe_mass2),
 "  $\\pm$  ",sigm2," (",sigm2/m2*100," %)"
print "   R_1 =  ",get_parameter_value(phoebe_radius1),
 "  $\\pm$  ",sigr1," (",sigr1/r1*100," %)"
print "   R_2 =  ",get_parameter_value(phoebe_radius2),
 "  $\\pm$  ",sigr2," (",sigr2/r2*100," %)"
print " logg1 =  ",logg1," $\\pm$  ",siglogg1,
 " (",siglogg1/logg1*100," %)"
print " logg2 =  ",logg2," $\\pm$  ",siglogg2,
 " (",siglogg2/logg2*100," %)"
print "  pot1 =  ",get_parameter_value(phoebe_pot1),
 "  $\\pm$  ",sigp1," (",sigp1/p1*100," %)"
print "  pot2 =  ",get_parameter_value(phoebe_pot2),
 "  $\\pm$  ",sigp2," (",sigp2/p2*100," %)"
```

```
print "    f1 =  ",get_parameter_value (phoebe_f1),
 "  $\\pm$  ",sigf1," (",sigf1/f1*100," %)"
print "    f2 =  ",get_parameter_value (phoebe_f2),
 "  $\\pm$  ",sigf2," (",sigf2/f2*100," %)"
print " t1/t2 =  ",teff1/teff2,"  $\\pm$  ",sigt1t2,
 " (",sigt1t2/teff1*teff2*100," %)"
print " teff2 =  ",get_parameter_value(phoebe_teff2),
 "  $\\pm$  ",sigteff2," (",sigteff2/teff2*100," %)"
print " "
print " Formal errors: "
print " sigma_r1 = ",sigr1f
print " sigma_r2 = ",sigr2f
print "  sigma_e = ",sigeccf
print "  sigma_w = ",sigperr0f
print "  sigma_i = ",siginclf
```

APPENDIX E

Par 1802: ABRIDGED VI_CJHK_S LIGHT CURVES

The tables presented in this Appendix will be published in its entirety in a machine-readable form in the online version of the paper by Gómez Maqueo Chew et al. (2010). A portion of each table is shown here for guidance regarding their form and content.

Table 11: Differential V band Light Curve of Par 1802

HJD[a]	Δm[b]	σ_m
2451930.557737	0.006	0.010
2451930.569416	-0.001	0.010
2451930.581025	0.007	0.010
2451930.592365	-0.007	0.010
2451930.603794	0.007	0.010
2451930.615404	0.000	0.010
2451930.626933	0.001	0.010
2451930.638092	-0.005	0.010
2451930.656051	-0.001	0.010
2451930.667491	0.001	0.011
2451930.679160	0.006	0.011
2451930.693249	-0.006	0.010
2451930.704649	0.007	0.010
2451930.735757	0.003	0.011
2451930.748306	-0.008	0.011

[a] Heliocentric Julian Date

[b] Differential V magnitude

Table 12: Differential I_C band Light Curve of Par 1802

HJD[a]	Δm[b]	σ_m
2449701.860452	-0.040	0.020
2449701.913182	-0.026	0.020
2449701.938571	-0.026	0.020
2449701.976661	0.006	0.020
2449702.006931	-0.001	0.020
2449702.687600	-0.012	0.020
2449702.716890	-0.015	0.020
2449702.745210	0.003	0.020
2449702.773530	0.007	0.020
2449702.805760	0.009	0.020
2449702.861430	0.028	0.020
2449702.889750	0.027	0.020
2449702.918070	0.031	0.020
2449702.950290	0.032	0.020
2449702.981540	0.030	0.020

[a] Heliocentric Julian Date

[b] Differential I_C magnitude

Table 13: Differential J band Light Curve of Par 1802

HJD[a]	Δm[b]
2454013.794832	-0.010
2454040.717805	-0.002
2454041.709868	0.012
2454005.796854	-0.006
2453981.864644	0.018
2453999.786555	0.002
2454071.679609	0.150
2454002.846548	-0.025
2454003.778756	0.036
2454019.797322	-0.008
2454020.805072	0.013
2453993.868102	-0.027
2454023.779094	0.025
2454049.717259	0.008
2454050.713167	0.136
2454024.794247	-0.021

[a] Heliocentric Julian Date

[b] Differential J magnitude

Table 14: Differential H band Light Curve of Par 1802

HJD[a]	Δm[b]
2454376.787242	-0.014
2454377.789689	0.143
2454378.775544	-0.020
2454378.785284	0.012
2454380.739724	-0.019
2454381.776602	-0.025
2454381.886711	-0.012
2454382.748298	0.008
2454383.729640	0.004
2454383.859218	0.005
2454384.742592	0.047
2454384.862200	0.122
2454385.741196	-0.008
2454385.851496	-0.004

[a] Heliocentric Julian Date

[b] Differential H magnitude

Table 15: Differential K_S band Light Curve of Par 1802

HJD[a]	Δm[b]
2454013.798334	-0.006
2454040.721410	0.005
2454041.713265	0.001
2454005.800356	-0.011
2453981.868447	0.015
2453999.790149	0.012
2454071.683111	0.151
2454002.850061	-0.017
2454003.782373	0.043
2454019.800928	-0.002
2454020.808574	-0.009
2453993.871639	-0.011
2454023.782514	0.027
2454049.720749	0.003
2454050.716645	0.133

[a] Heliocentric Julian Date

[b] Differential K_S magnitude

APPENDIX F

Par 1802: DISTANCE ESTIMATION SCRIPT

This appendix contains IDL script used to calculate the distance to Par 1802 varying the contribution of the third body to the system's luminosity and given different values of the interstellar extinction.

```
;fractional contribution of third component
;frac=0.25 ; 1/5 th of total lum, 20% of total lum
;frac=0.5  ; 1/3 th of total lum, 33% of total lum
;frac=0.11 ; 10% of total lum
frac=1.   ; 50% of total lum
;frac=2/3. ; 40% of total lum

;r1=1.737;in Rsun
;r2=1.625;in Rsun
;with revised cooler temperatures
r1 = 1.730; in Rsun
r2 = 1.618; in Rsun

sr1=0.1;in Rsun
sr2=0.1;in Rsun

;t1=3.945e3;in K
t1=3.665e3
t2=t1/1.092
;t2=3.611e3;in K

st1=100.;in K
st2=100.;in K

;Constants:
sb=5.67051e-8; in W /(m^2  K^4)

lumsun=3.845e26 ;in W

rsun=6.95508e8;in m

mbolsun=4.74;from Allen's Aph, p 341
smbolsun=0.01
```

```
bc=-1.64;mags, from Table A5, Kenyon & Hartmann 1995
sbc=0.0;unknown!
vk=4.11;mags, also from Kenyon & Hartmann 1995
svk=0.03;Allen's Aph p. 151
k=9.938;mags, from 2MASS, simbad
sk=0.018;mags, from simbad



;luminosities:
lum1=4.*!dpi*sb*(r1*rsun)^2*(t1)^4/lumsun
lum2=4.*!dpi*sb*(r2*rsun)^2*(t2)^4/lumsun

slum1=2*lum1*sqrt((sr1/r1)^2+4*(st1/t1)^2)
slum2=2*lum2*sqrt((sr2/r2)^2+4*(st2/t2)^2)

lumsyst=(1.+frac)*(lum1+lum2)
slumsyst=(1.+frac)*sqrt(slum1^2+slum2^2)

;absolute magnitudes
mabs=mbolsun-2.5*alog10(lumsyst)
smabs=sqrt(smbolsun^2+(2.5*slumsyst/lumsyst)^2)

;apparent magnitudes
mapp=bc+vk+k
smapp=sqrt(sbc^2+svk^2+sk^2)

;distance
av=0.5; from Par1802 nature paper
sav=0.2; from Par 1802 nature paper

d0=10^((mapp-mabs+5.)/5.);in pc
sd0=alog(10)/5.*d0*sqrt(sav^2+smabs^2+smapp^2)

d=10^((mapp-mabs+5.+av)/5.);in pc
sd=alog(10)/5.*d*sqrt(sav^2+smabs^2+smapp^2)

;in pc, a_v = 0.32: is the extinction calculated for v1174 ori
d2=10^((mapp-mabs+5.+0.32)/5.)

;bw = wien's displacement constant of proportionality
bw = 2.89777e3 ; in microns * Kelvin
```

```
print,' '
print,'Distance to ONC: 436 +/- 20 pc (O'Dell and Henney 2008)'
print,' '
print,'T_1 = ',t1,'        T_2 = ',t2
print,'l_max,1 = ',bw/t1,'     l_max,2 = ',bw/t2
print,''
print,'L_3/L_tot = ', frac/(1+frac)
print,' '
print,'Av = 0, Distance:',d0,'   +/-',sd0
print,'Av = 0.32, Distance:',d2,'   +/-',sd
print,'Av = 0.5, Distance:',d,'   +/-',sd
```

APPENDIX G

2M0535−05: ABRIDGED JHK_S LIGHT CURVES

The tables presented in this Appendix are published in its entirety in a machine-readable form in the online version of the paper by Gómez Maqueo Chew et al. (2009). A portion of each table is shown here for guidance regarding their form and content.

Table 16: Differential J band Light Curve of 2M0535−05

HJD[a]	Δm[b]
2453311.723468	-0.02137
2453321.645380	0.00305
2453327.667177	0.09047
2453327.736855	0.25355
2453337.627205	0.44196
2453337.712161	0.30654
2453340.661636	0.02005
2453291.837179	0.06698
2453301.833196	0.13945
2453280.731279	-0.01333
2453280.795035	0.01343
2453280.850294	-0.02312
2453281.725007	0.00358
2453281.790626	0.01219
2453281.842875	0.00321

[a] Heliocentric Julian Date

[b] Differential J magnitude

Table 17: Differential H band Light Curve of 2M0535−05

HJD[a]	Δm[b]
2453426.520578	0.03610
2453445.485528	0.01546
2453428.650735	-0.00740
2453415.616726	0.00619
2453415.677288	0.06725
2453425.564072	0.37523
2453425.630860	0.53849
2453425.662732	0.47590
2453406.539051	0.01280
2453409.535701	-0.01483
2453409.619548	0.00244
2453435.510760	0.27719
2453435.569216	0.11036
2453435.621445	0.02131
2453436.510477	0.00301

[a] Heliocentric Julian Date

[b] Differential H magnitude

Table 18: Differential K_S band Light Curve of 2M0535−05

HJD[a]	Δm[b]
2453336.725515	-0.07627
2453336.758641	-0.04853
2453428.666590	-0.04077
2453415.586925	-0.03317
2453415.632014	-0.07676
2453415.692587	-0.00632
2453425.579580	0.42007
2453425.646588	0.49068
2453425.678437	0.44216
2453409.550989	0.01162
2453409.634848	0.00240
2453435.526476	0.21726
2453435.584515	0.11184
2453435.637277	0.00116
2453438.537777	0.08671

[a] Heliocentric Julian Date

[b] Differential K_S magnitude

BIBLIOGRAPHY

Baraffe, I., G. Chabrier, F. Allard, and P. H. Hauschildt (1998, September). Evolutionary models for solar metallicity low-mass stars: mass-magnitude relationships and color-magnitude diagrams. A&A *337*, 403–412.

Barden, S. C. and T. Armandroff (1995, June). Performance of the WIYN fiber-fed MOS system: Hydra. In S. C. Barden (Ed.), *Society of Photo-Optical Instrumentation Engineers (SPIE) Conference Series*, Volume 2476 of *Society of Photo-Optical Instrumentation Engineers (SPIE) Conference Series*, pp. 56–67.

Bate, M. R., I. A. Bonnell, and V. Bromm (2002, November). The formation of close binary systems by dynamical interactions and orbital decay. MNRAS *336*, 705–713.

Boden, A. F., A. I. Sargent, R. L. Akeson, J. M. Carpenter, G. Torres, D. W. Latham, D. R. Soderblom, E. Nelan, O. G. Franz, and L. H. Wasserman (2005, December). Dynamical Masses for Low-Mass Pre-Main-Sequence Stars: A Preliminary Physical Orbit for HD 98800 B. ApJ *635*, 442–451.

Bonnell, I. A., R. B. Larson, and H. Zinnecker (2007). The Origin of the Initial Mass Function. *Protostars and Planets V*, 149–164.

Bouvier, J., S. Cabrit, M. Fernandez, E. L. Martin, and J. M. Matthews (1993, May). Coyotes-I - the Photometric Variability and Rotational Evolution of T-Tauri Stars. A&A *272*, 176–+.

Burgasser, A. J., J. D. Kirkpatrick, M. W. McElwain, R. M. Cutri, A. J. Burgasser, and M. F. Skrutskie (2003, February). The 2Mass Wide-Field T Dwarf Search. I. Discovery of a Bright T Dwarf within 10 Parsecs of the Sun. AJ *125*, 850–857.

Cargile, P. (2010, May). Testing the Chronometric Accuracy of Stellar Evolution Models Using Young Stars in Open Clusters.

Cargile, P. A., K. G. Stassun, and R. D. Mathieu (2008, February). Discovery of Par 1802 as a Low-Mass, Pre-Main-Sequence Eclipsing Binary in the Orion Star-Forming Region. ApJ *674*, 329–335. (CSM07)

Carpenter, J. M., L. A. Hillenbrand, and M. F. Skrutskie (2001, June). Near-Infrared Photometric Variability of Stars toward the Orion A Molecular Cloud. AJ *121*, 3160–3190.

Chabrier, G. and I. Baraffe (2000). Theory of Low-Mass Stars and Substellar Objects. ARA&A *38*, 337–377.

Chabrier, G., J. Gallardo, and I. Baraffe (2007, September). Evolution of low-mass star and brown dwarf eclipsing binaries. A&A *472*, L17–L20.

Claret, A. (2000, November). A new non-linear limb-darkening law for LTE stellar atmosphere models. Calculations for -5.0 <= log[M/H] <= +1, 2000 K <= T_{eff} <= 50000 K at several surface gravities. A&A *363*, 1081–1190.

Close, L. M., N. Siegler, M. Freed, and B. Biller (2003, April). Detection of Nine M8.0-L0.5 Binaries: The Very Low Mass Binary Population and Its Implications for Brown Dwarf and Very Low Mass Star Formation. ApJ *587*, 407–422.

Covino, E., S. Catalano, A. Frasca, E. Marilli, M. Fernández, J. M. Alcalá, C. Melo, R. Paladino, M. F. Sterzik, and B. Stelzer (2000, September). RXJ 0529.4+0041: a low-mass pre-main sequence eclipsing-spectroscopic binary. A&A *361*, L49–L52.

Covino, E., A. Frasca, J. M. Alcalá, R. Paladino, and M. F. Sterzik (2004, November). Improved fundamental parameters for the low-mass pre-main sequence eclipsing system RX J0529.4+0041. A&A *427*, 637–649.

Cox, A. N. (2000). *Allen's astrophysical quantities*.

Cutri, R. M., M. F. Skrutskie, S. van Dyk, C. A. Beichman, J. M. Carpenter, T. Chester, L. Cambresy, T. Evans, J. Fowler, J. Gizis, E. Howard, J. Huchra, T. Jarrett, E. L. Kopan, J. D. Kirkpatrick, R. M. Light, K. A. Marsh, H. McCallon, S. Schneider, R. Stiening, M. Sykes, M. Weinberg, W. A. Wheaton, S. Wheelock, and N. Zacarias (2003, June). *2MASS All Sky Catalog of point sources.*

D'Antona, F. and I. Mazzitelli (1997). Evolution of low mass stars. *Memorie della Societa Astronomica Italiana 68*, 807–+.

DePoy, D. L., B. Atwood, S. R. Belville, D. F. Brewer, P. L. Byard, A. Gould, J. A. Mason, T. P. O'Brien, D. P. Pappalardo, R. W. Pogge, D. P. Steinbrecher, and E. J. Teiga (2003, March). A Novel Double Imaging Camera (ANDICAM). In M. Iye & A. F. M. Moorwood (Ed.), *Society of Photo-Optical Instrumentation Engineers (SPIE) Conference Series*, Volume 4841 of *Society of Photo-Optical Instrumentation Engineers (SPIE) Conference Series*, pp. 827–838.

Duquennoy, A. and M. Mayor (1991, August). Multiplicity among solar-type stars in the solar neighbourhood. II - Distribution of the orbital elements in an unbiased sample. A&A *248*, 485–524.

Famaey, B., A. Jorissen, X. Luri, M. Mayor, S. Udry, H. Dejonghe, and C. Turon (2005, January). Local kinematics of K and M giants from CORAVEL/Hipparcos/Tycho-2 data. Revisiting the concept of superclusters. A&A *430*, 165–186.

Fűrész, G., L. W. Hartmann, S. T. Megeath, A. H. Szentgyorgyi, and E. T. Hamden (2008, April). Kinematic Structure of the Orion Nebula Cluster and its Surroundings. ApJ *676*, 1109–1122.

Fischer, D. A. and G. W. Marcy (1992, September). Multiplicity among M dwarfs. ApJ *396*, 178–194.

Frasca, A., E. Covino, L. Spezzi, J. M. Alcalá, E. Marilli, G. Fżrész, and D. Gandolfi (2009, December). REM near-IR and optical photometric monitoring of pre-main sequence stars in Orion. Rotation periods and starspot parameters. A&A *508*, 1313–1330.

Glass, I. S. (1999, August). *Handbook of Infrared Astronomy*.

Gómez Maqueo Chew, Y., K. G. Stassun, A. Prša, L. Hebb, and R. D. Mathieu (2010). Uncovering Parenago 1802: the Pre-Main Sequence, Dissimilar Eclipsing Twins and their Third Companion. ApJ. To be submitted.

Gómez Maqueo Chew, Y., K. G. Stassun, A. Prša, and R. D. Mathieu (2009, July). Near-infrared Light Curves of the Brown Dwarf Eclipsing Binary 2MASS J05352184-0546085: Can Spots Explain the Temperature Reversal? ApJ *699*, 1196–1208.

Hauschildt, P. H., F. Allard, and E. Baron (1999, February). The NextGen Model Atmosphere Grid for 3000 <=T_{eff}<=10,000 K. ApJ *512*, 377–385.

Hillenbrand, L. A. (1997, May). On the Stellar Population and Star-Forming History of the Orion Nebula Cluster. AJ *113*, 1733–1768.

Hillenbrand, L. A., S. E. Strom, N. Calvet, K. M. Merrill, I. Gatley, R. B. Makidon, M. R. Meyer, and M. F. Skrutskie (1998, October). Circumstellar Disks in the Orion Nebula Cluster. AJ *116*, 1816–1841.

Honeycutt, R. K. (1992, June). CCD ensemble photometry on an inhomogeneous set of exposures. PASP *104*, 435–440.

Horne, J. H. and S. L. Baliunas (1986, March). A prescription for period analysis of unevenly sampled time series. ApJ *302*, 757–763.

Hut, P. (1981, June). Tidal evolution in close binary systems. A&A *99*, 126–140.

Irwin, J., S. Aigrain, S. Hodgkin, K. G. Stassun, L. Hebb, M. Irwin, E. Moraux, J. Bouvier, A. Alapini, R. Alexander, D. M. Bramich, J. Holtzman, E. L. Martín, M. J. McCaughrean, F. Pont, P. E. Verrier, and M. R. Zapatero Osorio (2007, September). The Monitor project: JW 380 - a 0.26-, 0.15-M_{solar}, pre-main-sequence eclipsing binary in the Orion nebula cluster. MNRAS *380*, 541–550.

Johnson, H. L. (1964, June). The colors, Bolometric corrections and effective temperatures of the bright stars. *Boletin de los Observatorios Tonantzintla y Tacubaya 3*, 305–324.

Kallrath, J. and E. F. Milone (2009). *Eclipsing Binary Stars: Modeling and Analysis*.

Kenyon, S. J. and L. Hartmann (1995, November). Pre-Main-Sequence Evolution in the Taurus-Auriga Molecular Cloud. ApJS *101*, 117–+.

Kirkpatrick, J. D., T. J. Henry, and D. W. McCarthy, Jr. (1991, November). A standard stellar spectral sequence in the red/near-infrared - Classes K5 to M9. ApJS *77*, 417–440.

Köhler, R., M. G. Petr-Gotzens, M. J. McCaughrean, J. Bouvier, G. Duchêne, A. Quirrenbach, and H. Zinnecker (2006, November). Binary stars in the Orion Nebula Cluster. A&A *458*, 461–476.

Kraus, A. L. and L. A. Hillenbrand (2009, October). The Coevality of Young Binary Systems. ApJ *704*, 531–547.

Kroupa, P. (1998, July). On the binary properties and the spatial and kinematical distribution of young stars. MNRAS *298*, 231–242.

Kurucz, R. L. (1996). Model Stellar Atmospheres and Real Stellar Atmospheres. In S. J. Adelman, F. Kupka, & W. W. Weiss (Ed.), *M.A.S.S., Model Atmospheres and Spectrum Synthesis*, Volume 108 of *Astronomical Society of the Pacific Conference Series*, pp. 2–+.

Lafrenière, D., R. Jayawardhana, A. Brandeker, M. Ahmic, and M. H. van Kerkwijk (2008, August). A Multiplicity Census of Young Stars in Chamaeleon I. ApJ *683*, 844–861.

Larson, R. B. (2003, October). The physics of star formation. *Reports on Progress in Physics 66*, 1651–1697.

Linnell, A. P. (1991, December). A test of the starspot hypothesis for W-type W Ursae Majoris light curves. ApJ *383*, 330–335.

Luhman, K. L. (1999, November). Young Low-Mass Stars and Brown Dwarfs in IC 348. ApJ *525*, 466–481.

MacDonald, J. and D. J. Mullan (2009, July). Structural Effects of Magnetic Fields in Brown Dwarfs. ApJ *700*, 387–394.

Maiti, M. (2007, April). Observational Evidence of Optical Variability in L Dwarfs. AJ *133*, 1633–1644.

Mason, B. D., D. R. Gies, W. I. Hartkopf, W. G. Bagnuolo, Jr., T. ten Brummelaar, and H. A. McAlister (1998, February). ICCD speckle observations of binary stars. XIX - an astrometric/spectroscopic survey of O stars. AJ *115*, 821–+.

Mathieu, R. D., I. Baraffe, M. Simon, K. G. Stassun, and R. White (2007). Dynamical Mass Measurements of Pre-Main-Sequence Stars: Fundamental Tests of the Physics of Young Stars. *Protostars and Planets V*, 411–425.

Mazeh, T. (2008). Observational Evidence for Tidal Interaction in Close Binary Systems. In M.-J. Goupil & J.-P. Zahn (Ed.), *EAS Publications Series*, Volume 29 of *EAS Publications Series*, pp. 1–65.

Melo, C. H. F., E. Covino, J. M. Alcalá, and G. Torres (2001, November). On the pre-main sequence circularization period. A&A *378*, 898–906.

Milone, E. F., R. E. Wilson, and B. J. Hrivnak (1987, August). RW Comae Berenices. III - Light curve solution and absolute parameters. ApJ *319*, 325–333.

Mohanty, S., K. G. Stassun, and R. D. Mathieu (2009, May). Circumstellar Environment and Effective Temperature of the Young Substellar Eclipsing Binary 2MASS J05352184-0546085. ApJ *697*, 713–720.

Morales, J. C., J. Gallardo, I. Ribas, C. Jordi, I. Baraffe, and G. Chabrier (2010, July). The Effect of Magnetic Activity on Low-Mass Stars in Eclipsing Binaries. ApJ *718*, 502–512.

O'Dell, C. R. and W. J. Henney (2008, October). High Spatial Velocity Features in the Orion Nebula,. AJ *136*, 1566–1586.

Palla, F. and I. Baraffe (2005, March). Pulsating young brown dwarfs. A&A *432*, L57–L60.

Prato, L., M. Simon, T. Mazeh, S. Zucker, and I. S. McLean (2002, November). Component Masses of the Young Spectroscopic Binary UZ Tau E. ApJ *579*, L99–L102.

Press, W. H., S. A. Teukolsky, W. T. Vetterling, and B. P. Flannery (2007). *Numerical recipes. The art of scientific computing*.

Prša, A. (2006, January). *PHOEBE Scientific Reference*.

Prša, A. and T. Zwitter (2005, July). A Computational Guide to Physics of Eclipsing Binaries. I. Demonstrations and Perspectives. ApJ *628*, 426–438.

Reiners, A., A. Seifahrt, K. G. Stassun, C. Melo, and R. D. Mathieu (2007, December). Detection of Strong Activity in the Eclipsing Binary Brown Dwarf 2MASS J05352184-0546085: A Possible Explanation for the Temperature Reversal. ApJ *671*, L149–L152.

Rhode, K. L., W. Herbst, and R. D. Mathieu (2001, December). Rotational Velocities and Radii of Pre-Main-Sequence Stars in the Orion Nebula Cluster. AJ *122*, 3258–3279.

Rucinski, S. (1999). Determination of Broadening Functions Using the Singular-Value Decomposition (SVD) Technique. In J. B. Hearnshaw and C. D. Scarfe (Eds.), *IAU Colloq. 170: Precise Stellar Radial Velocities*, Volume 185 of *Astronomical Society of the Pacific Conference Series*, pp. 82–+.

Scargle, J. D. (1982, December). Studies in astronomical time series analysis. II - Statistical aspects of spectral analysis of unevenly spaced data. ApJ *263*, 835–853.

Schwarzenberg-Czerny, A. (1991, November). Accuracy of period determination. MNRAS *253*, 198–206.

Setiawan, J., L. Pasquini, L. da Silva, O. von der Lühe, and A. Hatzes (2003, January). Precise radial velocity measurements of G and K giants. First results. A&A *397*, 1151–1159.

Simon, M. and R. C. Obbie (2009, February). Twins Among the Low-Mass Spectroscopic Binaries. AJ *137*, 3442–3448.

Skrutskie, M. F., R. M. Cutri, R. Stiening, M. D. Weinberg, S. Schneider, J. M. Carpenter, C. Beichman, R. Capps, T. Chester, J. Elias, J. Huchra, J. Liebert, C. Lonsdale, D. G. Monet, S. Price, P. Seitzer, T. Jarrett, J. D. Kirkpatrick, J. E. Gizis, E. Howard, T. Evans, J. Fowler, L. Fullmer, R. Hurt, R. Light, E. L. Kopan, K. A. Marsh, H. L. McCallon, R. Tam, S. Van Dyk, and S. Wheelock (2006, February). The Two Micron All Sky Survey (2MASS). AJ *131*, 1163–1183.

Stassun, K. G., R. D. Mathieu, P. A. Cargile, A. N. Aarnio, E. Stempels, and A. Geller (2008, June). Surprising dissimilarities in a newly formed pair of 'identical twin' stars. Nature *453*, 1079–1082. (SMC08)

Stassun, K. G., R. D. Mathieu, T. Mazeh, and F. J. Vrba (1999, June). The Rotation Period Distribution of Pre-Main-Sequence Stars in and around the Orion Nebula. AJ *117*, 2941–2979.

Stassun, K. G., R. D. Mathieu, and J. A. Valenti (2006, March). Discovery of two young brown dwarfs in an eclipsing binary system. Nature *440*, 311–314. (SMV06)

Stassun, K. G., R. D. Mathieu, and J. A. Valenti (2007, August). A Surprising Reversal of Temperatures in the Brown Dwarf Eclipsing Binary 2MASS J05352184-0546085. ApJ *664*, 1154–1166. (SMV07)

Stassun, K. G., R. D. Mathieu, L. P. R. Vaz, N. Stroud, and F. J. Vrba (2004, April). Dynamical Mass Constraints on Low-Mass Pre-Main-Sequence Stellar Evolutionary Tracks: An Eclipsing Binary in Orion with a 1.0 M_{solar} Primary and a 0.7 M_{solar} Secondary. ApJS *151*, 357–385.

Stellingwerf, R. F. (1978, September). Period determination using phase dispersion minimization. ApJ *224*, 953–960.

Stempels, H. C., L. Hebb, K. G. Stassun, J. Holtzman, N. Dunstone, L. Glowienka, and S. Frandsen (2008, April). The pre-main-sequence eclipsing binary ASAS J052821+0338.5. A&A *481*, 747–755.

Stempels, H. C. and N. Piskunov (2003, September). The photosphere and veiling spectrum of T Tauri stars. A&A *408*, 693–706.

Tonry, J. and M. Davis (1979, October). A survey of galaxy redshifts. I - Data reduction techniques. AJ *84*, 1511–1525.

Torres, G., J. Andersen, and A. Giménez (2010, February). Accurate masses and radii of normal stars: modern results and applications. A&A Rev. *18*, 67–126.

Tull, R. G. (1998, July). High-resolution fiber-coupled spectrograph of the Hobby-Eberly Telescope. In S. D'Odorico (Ed.), *Society of Photo-Optical Instrumentation Engineers (SPIE) Conference Series*, Volume 3355 of *Society of Photo-Optical Instrumentation Engineers (SPIE) Conference Series*, pp. 387–398.

van Hamme, W. (1993, November). New limb-darkening coefficients for modeling binary star light curves. AJ *106*, 2096–2117.

Van Hamme, W. and R. E. Wilson (2007, June). Third-Body Parameters from Whole Light and Velocity Curves. ApJ *661*, 1129–1151.

Vogt, S. S., S. L. Allen, B. C. Bigelow, L. Bresee, B. Brown, T. Cantrall, A. Conrad, M. Couture, C. Delaney, H. W. Epps, D. Hilyard, D. F. Hilyard, E. Horn, N. Jern, D. Kanto, M. J. Keane, R. I. Kibrick, J. W. Lewis, J. Osborne, G. H. Pardeilhan, T. Pfister, T. Ricketts, L. B. Robinson, R. J. Stover, D. Tucker, J. Ward, and M. Z. Wei (1994, June). HIRES: the high-resolution echelle spectrometer on the Keck 10-m Telescope. In D. L. Crawford & E. R. Craine (Ed.), *Society of Photo-Optical Instrumentation Engineers (SPIE) Conference Series*, Volume 2198 of *Society of Photo-Optical Instrumentation Engineers (SPIE) Conference Series*, pp. 362–+.

von Zeipel, H. (1924, June). The radiative equilibrium of a rotating system of gaseous masses. MNRAS *84*, 665–683.

Wainscoat, R. J. and L. L. Cowie (1992, January). A filter for deep near-infrared imaging. AJ *103*, 332–337.

Wall, J. V. and C. R. Jenkins (2003, November). *Practical Statistics for Astronomers*. Princeton Series in Astrophysics.

Whitney, B. A., K. Wood, J. E. Bjorkman, and M. Cohen (2003, December). Two-dimensional Radiative Transfer in Protostellar Envelopes. II. An Evolutionary Sequence. ApJ *598*, 1079–1099.

Wilson, R. E. (1979, December). Eccentric orbit generalization and simultaneous solution of binary star light and velocity curves. ApJ *234*, 1054–1066.

Wilson, R. E. (1990, June). Accuracy and efficiency in the binary star reflection effect. ApJ *356*, 613–622.

Wilson, R. E. (2008, January). Eclipsing Binary Solutions in Physical Units and Direct Distance Estimation. ApJ *672*, 575–589.

Wilson, R. E. and P. Biermann (1976, May). TX CANCRI - Which component is hotter. A&A *48*, 349–357.

Wilson, R. E. and E. J. Devinney (1971, June). Realization of Accurate Close-Binary Light Curves: Application to MR Cygni. ApJ *166*, 605–+.

Zahn, J. (1977, May). Tidal friction in close binary stars. A&A *57*, 383–394.

Zapatero Osorio, M. R., J. A. Caballero, and V. J. S. Béjar (2005, March). Optical Linear Polarization of Late M and L Type Dwarfs. ApJ *621*, 445–460.

Zucker, S. and T. Mazeh (1994, January). Study of spectroscopic binaries with TODCOR. 1: A new two-dimensional correlation algorithm to derive the radial velocities of the two components. ApJ *420*, 806–810.